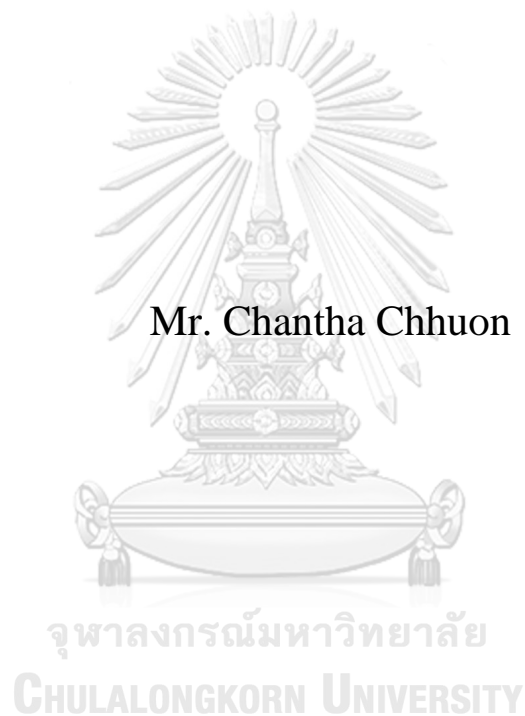


**SBFE ANALYSIS OF LAYERED ELASTIC MEDIA WITH
CONSIDERATION OF SURFACE ENERGY EFFECT**



A Thesis Submitted in Partial Fulfillment of the Requirements
for the Degree of Master of Engineering in Civil Engineering
Department of Civil Engineering
Faculty of Engineering
Chulalongkorn University
Academic Year 2018
Copyright of Chulalongkorn University

การวิเคราะห์ตัวกลางชั้นยึดหยุ่น โดยพิจารณาผลของพลังงานที่ผิวด้วยระเบียบวิธีสเกลบาวดารีไฟ
ไนท์เอลิเมนต์



วิทยานิพนธ์นี้เป็นส่วนหนึ่งของการศึกษาตามหลักสูตรปริญญาวิศวกรรมศาสตรมหาบัณฑิต
สาขาวิชาวิศวกรรมโยธา ภาควิชาวิศวกรรมโยธา
คณะวิศวกรรมศาสตร์ จุฬาลงกรณ์มหาวิทยาลัย
ปีการศึกษา 2561
ลิขสิทธิ์ของจุฬาลงกรณ์มหาวิทยาลัย

Thesis Title	SBFE ANALYSIS OF LAYERED ELASTIC MEDIA WITH CONSIDERATION OF SURFACE ENERGY EFFECT
By	Mr. Chantha Chhuon
Field of Study	Civil Engineering
Thesis Advisor	Associate Professor Jaron Rungamornrat, Ph.D.
Thesis Co Advisor	Assistant Professor Sawekchai Tangaramvong, Ph.D.

Accepted by the Faculty of Engineering, Chulalongkorn University in Partial Fulfillment of the Requirement for the Master of Engineering

----- Dean of the Faculty of Engineering
(Professor SUPOT TEACHAVORASINSKUN, D.Eng.)

THESIS COMMITTEE

----- Chairman
(Professor Teerapong Senjuntichai, Ph.D.)

----- Thesis Advisor
(Associate Professor Jaron Rungamornrat, Ph.D.)

----- Thesis Co-Advisor
(Assistant Professor Sawekchai Tangaramvong, Ph.D.)

----- Examiner
(Assistant Professor WATANACHAI SMITTAKORN, Ph.D.)

----- External Examiner
(Assistant Professor Yasothorn Sapsathiarn, Ph.D.)



จุฬาลงกรณ์มหาวิทยาลัย
CHULALONGKORN UNIVERSITY

จันทา ชวน : การวิเคราะห์ตัวกลางชั้นยึดหยุ่นโดยพิจารณาผลของพลังงานที่ผิวด้วยระเบียบวิธีเสกัลบาวารีไฟไนต์เอลิเมนต์. (SBFE ANALYSIS OF LAYERED ELASTIC MEDIA WITH CONSIDERATION OF SURFACE ENERGY EFFECT) อ.ที่ปรึกษาหลัก : รศ. ดร.จรูญ รุ่งอมรรัตน์, อ.ที่ปรึกษาร่วม : ผศ. ดร.เสกษชัย ตั้งอร่ามวงศ์

วิทยานิพนธ์นี้นำเสนอระเบียบวิธีเชิงตัวเลขที่ถูกต้องและมีประสิทธิภาพสำหรับหาผลตอบสนองเชิงกลของตัวกลางชั้นยึดหยุ่นไร้ขอบเขตสองมิติภายใต้แรงกระทำใดๆที่ผิวและอิทธิพลของหน่วยแรงที่ผิว สมการกำกับของชั้นบัลล์ทั่วไปสร้างจากทฤษฎียึดหยุ่นเชิงเส้นดั้งเดิมโดยใช้ระเบียบวิธีเสกัลบาวารีไฟไนต์เอลิเมนต์ ส่วนสมการกำกับของวัสดุผิวสร้างจากทฤษฎียึดหยุ่นรูปแบบเต็มของเกอดิน-เมอร์คอค สมการกำกับถูกพัฒนาขึ้นในกรอบทั่วไปทำให้สามารถพิจารณาวัสดุบัลล์ทั้งกรณีที่มีคุณสมบัติคงที่และไม่คงที่ในแนวตั้งในแต่ละชั้นของตัวกลางได้ ระบบสมการอนุพันธ์เชิงเส้นแบบไม่เอกพันธ์ซึ่งกำกับฟังก์ชันปมของตัวกลางชั้นสร้างโดยอาศัยความต่อเนื่องบริเวณรอยต่อระหว่างผิววัสดุและบัลล์ ผลเฉลยทั่วไปของระบบสมการอนุพันธ์ดังกล่าวหาได้โดยใช้ระเบียบวิธีมาตรฐานและผลเฉลยที่ได้ถูกนำไปใช้สร้างระบบสมการพีชคณิตเชิงเส้นซึ่งกำกับข้อมูลของตัวกลางชั้น ระเบียบวิธีเสกัลบาวารีไฟไนต์เอลิเมนต์แบบโดเมนย่อยได้ถูกนำมาใช้เพื่อให้สามารถสร้างระบบสมการกำกับสุดท้ายสำหรับตัวกลางชั้นรวมได้ง่ายในกรณีที่แรงกระทำบนพื้นที่จำกัด มีการรายงานและอภิปรายผลเฉลยเชิงตัวเลขสำหรับกรณีตัวอย่างต่างๆ เพื่อตรวจสอบความถูกต้อง พหุคูณการลู่เข้า และความสามารถของระเบียบวิธีที่นำเสนอด้วย



สาขาวิชา วิศวกรรมโยธา
ปีการศึกษา 2561

ลายมือชื่อนิสิต
ลายมือชื่อ อ.ที่ปรึกษาหลัก
ลายมือชื่อ อ.ที่ปรึกษาร่วม

6070166721 : MAJOR CIVIL ENGINEERING

KEYWORD: FG materials, Gurtin-Murdoch model, Layered media, Scaled boundary finite element method, Surface stresses

Chantha Chhuon : SBFEM ANALYSIS OF LAYERED ELASTIC MEDIA WITH CONSIDERATION OF SURFACE ENERGY EFFECT. Advisor: Assoc. Prof. Jaron Rungamornrat, Ph.D. Co-advisor: Asst. Prof. Sawekchai Tangaramvong, Ph.D.

This thesis presents an efficient and accurate numerical technique for determining mechanical response of a two-dimensional, infinite, elastic, layered medium under arbitrary surface loading and surface stress effects. Governing equations of a generic bulk layer are formulated from the classical linear elasticity theory via a SBFEM technique whereas those of the generic material surface are obtained from a full version of Gurtin-Murdoch surface elasticity theory. The formulation is established sufficiently general allowing both homogenous and functionally graded bulk materials to be treated for each layer. By enforcing the continuity at the interface of the material surface and the bulk, it leads to a system of non-homogenous, linear, ordinary differential equations governing the nodal functions of the layered medium. A general solution of the resulting system of ODEs is then constructed via standard procedures and then used to form a system of linear algebraic equations governing nodal boundary data. To facilitate the treatment of surface loading over a finite region, a SBFEM subdomain technique is applied to establish a final system of governing equations for the whole layered medium. To fully investigate the accuracy, convergence, and capability of the proposed method, selected scenarios are solved and obtained numerical results are reported and discussed.



Field of Study: Civil Engineering
Academic Year: 2018

Student's Signature
Advisor's Signature
Co-advisor's Signature

ACKNOWLEDGEMENTS

Firstly, I would like to express my sincere gratitude to my thesis advisor, Associate Professor Dr. Jaroon Rungamornrat, for his continuous support of master's degree studies and the entire research. Thousand thanks to his motivation and patience to me from the start until now. Whenever I ran into trouble with both studying and living condition, his office's door was always opened for me. His guidance helped me in all kind of situations and I could not have imagined finishing this research without him.

I would also like to thank Assistant Professor Dr. Sawekchai Tangaramvong for his support related to the employed technique in the research. His guidance, as well as recommendation, provide me a better understanding of SBFEM. With his support, I can efficiently work faster with a better result.

Next, I would like to thank all thesis committees: Professor Dr. Teerapong Senjuntichai, Assistant professor Dr. Watanachai Smittakorn, and Assistant Professor Dr. Yasothorn Sapsathiarn for the useful suggestions, guidance, and feedbacks. This research is remarkably improved due to their insightful comments and encouragement.

Deeply thanks to Collaborative Research Program (CR) under ASEAN University Network Southeast Asia Engineering Education Development Network Program (AUN/SEED-Net) of Japan International Cooperation Agency (JICA) JFY 2017-2018 for financial support. To me, this support is invaluable and without it, I cannot be here and this will never be done by me.

Also, thanks to all lectures as well as the academic staffs in Structural Division of Civil Engineering Department for their guidance, helps and supports related to my studies.

Lastly, I would like to express my sincere gratitude to my family, relatives, and friends who usually give me support, encouragement not only during the period of conducting this research but also so far. All of them are usually with me, help me, and listen to me most of the time I need help from them. Their presence means a lot to me.

Chantha Chhuon

TABLE OF CONTENTS

	Page
ABSTRACT (THAI)	iii
ABSTRACT (ENGLISH).....	iv
ACKNOWLEDGEMENTS	v
TABLE OF CONTENTS.....	vi
LIST OF TABLES	viii
LIST OF FIGURES	ix
LIST OF ABBREVIATION.....	xiii
CHAPTER 1 INTRODUCTION	1
1.1. Motivation and Significance.....	1
1.2. Literature Review	3
1.2.1. Surface elasticity theory	4
1.2.2. Layered media under surface loading.....	5
1.2.3. Contact on layered media.....	7
1.2.4. Scaled Boundary Finite Element Method	9
1.3. Objective.....	11
1.4. Scope of Work.....	11
1.5. Methodology	11
1.6. Outcome and Contribution	13
CHAPTER 2 FORMULATION	14
2.1. Problem Description	14
2.2. Governing Equations for Generic Layer.....	15
2.2.1. Governing Equation for Bulk Layer.....	16
2.2.1.1. Scaled Boundary Finite Element Approximation.....	18
2.2.1.2. Scaled Boundary Finite Element Equations	19
2.2.2. Governing Equation for Material Surface/Interface.....	21

2.3. Governing Equation for Layered Medium.....	22
CHAPTER 3 SOLUTION METHODOLOGY	26
3.1. Homogeneous Solution.....	26
3.2. Particular Solution	29
3.3. General Solution	30
3.4. Solution of entire layered medium	31
3.5. Error	33
3.6. Rate of convergence.....	33
CHAPTER 4 NUMERICAL RESULTS	34
4.1. Surface-loaded Half-plane	34
4.2. Homogeneous half-plane without surface stresses	35
4.2.1. Functionally graded half-plane.....	42
4.3. Single layer medium	45
4.3.1. Uniformly distributed normal traction	45
4.3.2. Uniformly distributed shear traction	62
4.4. Surface loaded multilayer media	78
CHAPTER 5 CONCLUSIONS	90
REFERENCES	92
VITA.....	98

LIST OF TABLES

	Page
Table 1: Relative percent error and rate of convergence of numerical solutions with linear elements (solution generated by a uniform mesh containing 128 quadratic elements is taken as the exact solution)	59
Table 2: Relative percent error and rate of convergence of numerical solutions with quadratic elements (solution generated by a uniform mesh containing 128 quadratic elements is taken as the exact solution)	59
Table 3: Relative percent error and rate of convergence of numerical solutions with linear elements (solution generated by a uniform mesh containing 128 quadratic elements is taken as the exact solution)	76
Table 4: Relative percent error and rate of convergence of numerical solutions with quadratic elements (solution generated by a uniform mesh containing 128 quadratic elements is taken as the exact solution)	76
Table 5: Material properties of Al [111] and Si [100]	79
Table 6: Relative percent error and rate of convergence of numerical solutions generated by linear elements without surface stresses (solution generated by a uniform mesh containing 128 quadratic elements is taken as the converged solution).....	79
Table 7: Relative percent error and rate of convergence of numerical solutions generated by linear elements with surface stresses (solution generated by a uniform mesh containing 128 quadratic elements is taken as the converged solution).....	79

LIST OF FIGURES

	Page
Figure 1: Schematic of a two-dimensional, multi-layer body subjected to the arbitrary loading at the top surface	14
Figure 2: Schematic of the k^{th} surface and the k^{th} bulk layer.....	15
Figure 3: Elastic half-plane loaded by constant pressure p over length $2a$	34
Figure 4: Normalized vertical stress along the line of symmetry obtained from uniform meshes containing linear elements.....	37
Figure 5: Normalized vertical stress along the line of symmetry obtained from uniform meshes containing quadratic elements	37
Figure 6: Normalized vertical stress along the line of symmetry obtained from non-uniform meshes containing linear elements.....	38
Figure 7: Normalized vertical stress along the line of symmetry obtained from non-uniform meshes containing quadratic elements	38
Figure 8: Normalized surface displacement of a homogeneous half-plane without influence of surface stresses.....	39
Figure 9: Normalized horizontal and vertical stress components of a homogeneous half-plane without influence of surface stresses. Results are reported along $x_1 = 0$	39
Figure 10: Normalized horizontal stress component of a homogeneous half-plane without influence of surface stresses. Results are reported at different depths.	40
Figure 11: Normalized vertical stress component of a homogeneous half-plane without influence of surface stresses. Results are reported at different depths.	40
Figure 12: Normalized shear stress component of a homogeneous half-plane without influence of surface stresses. Results are reported at different depths.	41
Figure 13: Normalized vertical stress generated from standard FEM, SBFEM and reference solution.....	41
Figure 14: Normalized surface horizontal displacement of FG half-plane under uniformly distributed normal traction.....	43
Figure 15: Normalized surface vertical displacement of FG half-plane under uniformly distributed normal traction.....	44

Figure 16: Normalized surface vertical stress of FG half-plane under uniformly distributed normal traction.....	44
Figure 17: Semi-infinite rigid-based elastic layer under surface loading: (a) uniformly distributed normal traction and (b) uniformly distributed shear traction.....	45
Figure 18: Normalized vertical displacement along the line of symmetry obtained from uniform meshes containing linear elements.....	47
Figure 19: Normalized vertical stress along the line of symmetry obtained from uniform meshes containing linear elements.....	47
Figure 20: Normalized vertical displacement along the line of symmetry obtained from uniform meshes containing quadratic elements.....	48
Figure 21: Normalized vertical stress along the line of symmetry obtained from uniform meshes containing quadratic elements.....	48
Figure 22: Normalized horizontal displacement along (a) x_1 -direction and (b) x_2 -direction generated by a uniform mesh containing 128 quadratic elements.....	49
Figure 23: Normalized vertical displacement along (a) x_1 -direction and (b) x_2 -direction generated by a uniform mesh containing 128 quadratic elements.....	50
Figure 24: Normalized horizontal stress along (a) x_1 -direction and (b) x_2 -direction generated by a uniform mesh containing 128 quadratic elements.....	51
Figure 25: Normalized vertical stress along (a) x_1 -direction and (b) x_2 -direction generated by a uniform mesh containing 128 quadratic elements.....	52
Figure 26: Normalized shear stress along (a) x_1 -direction and (b) x_2 -direction generated by a uniform mesh containing 128 quadratic elements.....	53
Figure 27: Contour plot of normalized horizontal displacement ($\mu u_1 / p$) of a rigid-based elastic layer under uniformly distributed normal traction: (a) without surface effect and (b) with surface effect.....	54
Figure 28: Contour plot of normalized vertical displacement ($\mu u_2 / p$) of a rigid-based elastic layer under uniformly distributed normal traction: (a) without surface effect and (b) with surface effect.....	55
Figure 29: Contour plot of normalized horizontal stress ($-\sigma_{11} / p$) of a rigid-based elastic layer under uniformly distributed normal traction: (a) without surface effect and (b) with surface effect.....	56

Figure 30: Contour plot of normalized vertical stress ($-\sigma_{22} / p$) of a rigid-based elastic layer under uniformly distributed normal traction: (a) without surface effect and (b) with surface effect	57
Figure 31: Contour plot of normalized shear stress ($-\sigma_{12} / p$) of a rigid-based elastic layer under uniformly distributed normal traction: (a) without surface effect and (b) with surface effect.....	58
Figure 32: Relative percent error of numerical solutions generated by uniform meshes of linear and quadratic elements (solution generated by a uniform mesh containing 128 quadratic elements is taken as the exact solution)	60
Figure 33: Convergence study of normalized vertical stress obtained from finite element method with meshes containing 8 nodes rectangular elements.....	61
Figure 34: Comparison of converged normalized vertical stress from SBFEM (16 quadratic elements) and FEM (10240 8-node rectangular elements).	61
Figure 35: Normalized horizontal displacement along the line of anti-symmetry obtained from uniform meshes of linear elements.....	64
Figure 36: Normalized shear stress along the line of anti-symmetry obtained from uniform meshes of linear elements	64
Figure 37: Normalized horizontal displacement along the line of anti-symmetry obtained from uniform meshes of quadratic elements	65
Figure 38: Normalized shear stress along the line of anti-symmetry obtained from uniform meshes of quadratic elements	65
Figure 39: Normalized horizontal displacement along (a) x_1 -direction and (b) x_2 -direction generated by a uniform mesh containing 128 quadratic elements.....	66
Figure 40: Normalized vertical displacement along (a) x_1 -direction and (b) x_2 -direction generated by a uniform mesh containing 128 quadratic elements.....	67
Figure 41: Normalized horizontal stress along (a) x_1 -direction and (b) x_2 -direction generated by a uniform mesh containing 128 quadratic elements.....	68
Figure 42: Normalized vertical stress along (a) x_1 -direction and (b) x_2 -direction generated by a uniform mesh containing 128 quadratic elements.....	69
Figure 43: Normalized shear stress along (a) x_1 -direction and (b) x_2 -direction generated by a uniform mesh containing 128 quadratic elements.....	70

Figure 44: Contour plot of normalized horizontal displacement ($\mu u_1 / q$) of a rigid-based elastic layer under uniformly distributed shear traction: (a) without surface effect and (b) with surface effect	71
Figure 45: Contour plot of normalized vertical displacement ($\mu u_2 / q$) of a rigid-based elastic layer under uniformly distributed shear traction: (a) without surface effect and (b) with surface effect	72
Figure 46: Contour plot of normalized horizontal stress ($-\sigma_{11} / q$) of a rigid-based elastic layer under uniformly distributed shear traction: (a) without surface effect and (b) with surface effect	73
Figure 47: Contour plot of normalized vertical stress ($-\sigma_{22} / q$) of a rigid-based elastic layer under uniformly distributed shear traction: (a) without surface effect and (b) with surface effect	74
Figure 48: Contour plot of normalized shear stress ($-\sigma_{12} / q$) of a rigid-based elastic layer under uniformly distributed shear traction: (a) without surface effect and (b) with surface effect.....	75
Figure 49: Relative percent error of numerical solutions generated by uniform meshes of linear and quadratic elements (solution generated by a uniform mesh containing 128 quadratic elements is taken as the exact solution)	76
Figure 50: Convergence study of normalized vertical stress obtained from finite element method with meshes containing 8 nodes rectangular elements.....	77
Figure 51: Comparison of converged normalized vertical stress from SBFEM (16 quadratic elements) and FEM (2560 8-node rectangular elements).	77
Figure 52: Schematic of a semi-infinite, rigid-based, Si/Al layered elastic medium subjected to uniformly distributed normal traction p over the normalized length $2\bar{a}$	78
Figure 53: Relative percent error of numerical solutions generated by uniform meshes of linear elements without surface stresses	80
Figure 54: Relative percent error of numerical solutions generated by uniform meshes of linear elements with surface stresses	80
Figure 55: Normalized vertical displacement of Si/Al layered medium along x_1 - direction generated by a uniform mesh containing 128 quadratic elements.....	82
Figure 56: Normalized vertical stress of Si/Al layered medium along x_1 -direction generated by a uniform mesh containing 128 quadratic elements.....	82

Figure 57: Normalized vertical displacement of Si/Al layered medium along x_2 -direction generated by a uniform mesh containing 128 quadratic elements.....	83
Figure 58: Normalized vertical stress of Si/Al layered medium along x_2 -direction generated by a uniform mesh containing 128 quadratic elements.....	83
Figure 59: Contour plot of normalized horizontal displacement ($\mu u_1 / q$) of Si/Al layered medium under uniformly distributed normal traction: (a) without surface effect and (b) with surface effect	84
Figure 60: Contour plot of normalized horizontal displacement ($\mu u_2 / q$) of Si/Al layered medium under uniformly distributed normal traction: (a) without surface effect and (b) with surface effect	85
Figure 61: Contour plot of normalized horizontal stress ($-\sigma_{11} / p$) of Si/Al layered medium under uniformly distributed normal traction: (a) without surface effect and (b) with surface effect	86
Figure 62: Contour plot of normalized vertical stress ($-\sigma_{22} / p$) of Si/Al layered medium under uniformly distributed normal traction: (a) without surface effect and (b) with surface effect	87
Figure 63: Contour plot of normalized shear stress ($-\sigma_{12} / p$) of Si/Al layered medium under uniformly distributed normal traction: (a) without surface effect and (b) with surface effect	88
Figure 64: Convergence of normalized vertical stress generated from 8 nodes rectangular element of ANSYS	89
Figure 65: Comparison of normalized vertical stress generated from 16 quadratic element of SBFEM and 10240 element of ANSYS.....	89

LIST OF ABBREVIATION

a	Length of applied load
\mathbf{a}_k	Constant vector of applied traction vector
A	Unknown constant vector of particular solution of the unknown displacement
b	Superscript designated the quantities of the bulk
$\mathbf{b}_1, \mathbf{b}_2$	Constants matrices of L operator
B	Vector of derivation of Nodal basic function N
c	Arbitrary constant
C^+, C^o, C^-	Arbitrary constant vectors associated with R^+, R^o, R^-
D	Material matrix containing material constant
E	Material constant matrix
E_0^b, E_1^b, E_2^b	Coefficient matrices of the bulk material
f	Superscript designated unknown quantities
h_i	Element size
h	Thickness of layered media
K	Coefficient matrix
L	Two-dimensional linear differential operator
n	Number of nodes for the enter media
\mathbf{n}	Unit normal vector
N	Number of layers
N	Vector containing nodal basic functions
O	Origin of Cartesian coordinate

p	Number of node per bulk
p	Uniformly distributed normal traction
$\mathbf{P}^l, \mathbf{P}^r$	Vector containing nodal traction on $\partial\Omega^l$ and $\partial\Omega^r$
q	Uniformly distributed tangential traction
q_i	i^{th} modal internal flux
Q	Internal flux
r	Superscript designated the prescribed quantities
r_i	i^{th} modal scaling factor
$\mathbf{R}^+, \mathbf{R}^o, \mathbf{R}^-$	Diagonal matrices containing eigenvalue involving the positive, zero, and negative real part
s	Superscript designate the surface quantities
t_1^o	Arbitrary distributed normal surface traction
t_2^o	Arbitrary distributed tangential surface traction
\mathbf{t}	Vector containing nodal traction
\mathbf{t}^o	Vector containing applied traction at the top surface t_1^o and t_2^o
T	Superscript designated the transpose operator
$\mathbf{T}^u, \mathbf{T}^b$	Vector containing nodal traction on $\partial\Omega^l$ and $\partial\Omega^b$
\mathbf{u}	Vector containing in-plane displacement components
\mathbf{U}	Vector containing nodal displacements
\mathbf{V}	Vector containing mode shape vector and modal internal flux
w	Arbitrary weight residual function
\mathbf{W}	Vector containing nodal weight function
x_1	Horizontal axis of Cartesian coordinate

x_2	Vertical axis of Cartesian coordinate
$\phi^{(i)}$	Nodal basic function at i^{th} node
η_i	i^{th} mode shape vector
Ω	Rectangular region representing the bulk material
$\partial\Omega^l$	Left boundary of rectangular region Ω
$\partial\Omega^r$	Right boundary of rectangular region Ω
$\partial\Omega^t$	Top boundary of rectangular region Ω
$\partial\Omega^b$	Bottom boundary of rectangular region Ω
$\Gamma^+, \Gamma^o, \Gamma^-$	Matrices containing all vectors of r_i and η_i generated from the eigenvalue associated with the positive real part R^+ , the zero part R^o , and the negative real part R^-
Π^+, Π^o, Π^-	Diagonal matrices obtained by substituting the diagonal entries r_i of the matrices R^+, R^o and R^- respectively into the function $e^{r_i x_1}$
σ	Vector containing in-plane stress components
ε	Vector containing in-plane strain components
λ	Bulk's Lamé constant
λ^s	Surface's Lamé constant
μ	Bulk shear modulus
μ^s	Surface's shear modulus
τ^s	Surface's residual tension
ν	Bulk's Poisson ratio
A	Material intrinsic length scale

CHAPTER 1

INTRODUCTION

This chapter begins with the summary of fundamental aspects of the proposed research including the research significance, research interest, relevant previous studies and also the research objective. After the research problem is clearly stated, the scope of work and the methodology are addressed. Finally, expected outcomes and contributions are briefly presented in the last part of the chapter.

1.1. Motivation and Significance

Since the discovery of a new class of materials in the late 80's, commonly known and named as nano-materials, researches in nanotechnology have become popular, continuously grown and extensively attracted investigators in various fields of sciences and engineering. Due to unique properties of nano-scale/nano-structured materials and current advances in the nanotechnology, various means have been introduced to develop/design/fabricate smaller, stronger, more affordable, and even more environmentally friendly devices and objects to serve many purposes with better benefits to human daily life. At the same time, significant effort must be invested in parallel to not only gain an adequate insight of underlying knowledge in the area but also be capable of transferring such fundamental knowledge to support practical uses.

Nano-scale materials and technology have also been well recognized in surface coating applications. Both single-layer and multi-layer surface coatings by nano-scale materials have been commonly utilized to modify/enhance the surface properties and overall performance of components. For instance, a reflective color filter device made from photonic nano-structure can be used to replace the conventional color filter on the LCD screen in order to harvest the wasted energy of the absorbed light into electricity (Park et al., 2011). Likewise, a compact of multilayer film structures can be applied to solar-thermal harvesting, thermoelectric detection and imaging due to its possibility in ultra-broadband and perfect omnidirectional absorption (Yang et al., 2016). The surface coating is also required for quantum dots (QDs) in order to improve or strengthen their performance regarding

the fluorescence property and long-term stability. Other types of surface coatings for abrasive resistance were extensively reviewed in the work of [Wu et al. \(2014\)](#). Due to the vast applications of nano-scale surface coating, the fundamental understanding and the capability to assess/predict the performance of the surface after coating is essential and provide the basic information in the design procedure.

To investigate key responses and performance of nano-scale coated surfaces, two fundamental approaches including experimental studies and mathematical modeling can be applied. The former approach has been recognized to generally offer a better set of results representing/describing the real response of interest ([Wong et al., 1997](#)) ; however, the method itself may not be necessary a good candidate for all researchers due to various factors such as high-precision measurement and testing devices required, sophisticated testing environments and procedures, preparation of specimens and test setups, and, more importantly, the prohibitive cost consumed. Theoretical simulations based upon discrete mathematical models, such as atomistic and molecular dynamics simulations, have also been found an alternative promising tool to gain profound understanding of physical responses of nano-scale problems ([Shenoy, 2002](#)). Besides the high accuracy gained, the technique requires extremely large computational resources regarding the treatment of discrete feature of matter in a small scale and the complexity of the governing physics and this, as a result, renders its limited use.

In the past several decades, attempts have been made to propose alternative continuum-based models, in which the object is still treated as a continuum, to alleviate the requirement of existing discrete-based approaches but still providing sufficiently accurate results. Unlike problems in a macro-scale, various effects have been observed and found significant in small-scale problems such as the surface free energy and the nonlocality induced by the long-range interatomic attraction. It has been well recognized that classical size-independent theories in continuum mechanics adopted specifically for simulating mechanical response of macro-scale problems have failed to simulate those situations. As a result, such existing continuum-based mathematical models must be properly modified or enhanced by integrating the influences observed in a small-scale before used in the simulations to sufficiently

capture the inherent small-scale characteristics. A surface elasticity theory proposed by [Gurtin and Murdoch \(1975\)](#) and [Gurtin and Murdoch \(1978\)](#) has become one of the most popular models utilized successfully by researchers to integrate the effect of surface free energy in the prediction of mechanical response for various nano-scale problems ([He et al., 2004](#), [Huang, 2008](#), [Ansari and Norouzzadeh, 2016](#), [Norouzzadeh and Ansari, 2018](#)). The key motivation of integrating the influence of surface stresses in the mathematical model relies upon the fact that materials at a nano-scale exhibit very high surface to volume ratio resulting in excess surface free energy caused by the exclusive surface's atom arrangement and, as a direct consequence, rendering their response strongly size-dependent especially when the internal length scale of materials and the external characteristic length of the problems are comparable ([Dingreville et al., 2005](#)). Within the context of surface and contact mechanics, recent applications of G-M surface elasticity has also been recognized ([Rungamornrat et al., 2016](#), [Tartira, 2018](#), [Pinyochotiwong et al., 2013](#), [Intarit et al., 2018](#)). Nevertheless, most of existing studies found in the literature are quite limited in two folds, one associated with boundary value problems formulated in rather simple settings and the other corresponding to the solution techniques employed. The former raises the important issue on their direct application to simulate practical problems which are relatively complex in nature (e.g., multi-layer and functionally-graded-layer surface coatings) whereas the latter leads to the issue on the computational performance when the complex and large-scale problems are involved. The proposed study aims mainly to offer certain significant enhancement to narrow down such existing gap of knowledge.

1.2. Literature Review

To provide adequate historical background and emphasize the novel aspect of the proposed study, a set of relevant studies resulting from an extensive literature survey is presented in this section. Results from the review are separated into three parts including those related to the surface elasticity theory, the layered media under surface loadings, and contacts on layered media.

1.2.1. Surface elasticity theory

The concept of surface effects was originally introduced by [Gibbs \(1906\)](#); in his work, the surface free energy and the surface stresses were defined and derived from the well-known laws of thermodynamics. The distinction and the relationship between the surface free energy and the surface stresses were later elaborated by [Shuttleworth \(1950\)](#) and [Cammarata \(1994\)](#). Motivated by the original work of Gibbs, Gurtin and Murdoch ([1975, 1978](#)) has successfully established the mathematical framework, known as a surface elasticity theory, which supplies a set of equations sufficient for describing the mechanical response of both material surfaces and interfaces. Unlike the body treatment in a classical sense, the body, here, can be separated into the surface and the bulk in which the former is mathematically treated as the zero-thickness material layer perfectly adhered to the bulk with its behavior governed by constitutive laws exhibiting different properties from the bulk. With the integration of the surface effect through such the material layer, an intrinsic length scale of materials is automatically introduced, and the resulting mathematical model can now capture the size-dependent behavior ([Pinyochotiwong et al., 2013](#), [Intarit et al., 2018](#), [Tirapat and Senjuntichai, 2018](#), [Rungamornrat et al., 2016](#), [Tirapat et al., 2017](#), [Tarntira, 2018](#)).

Gurtin-Murdoch surface elasticity theory has gained significant attention and been extensively employed by various investigators, for the past three decades, in the simulations of nano-scale problems such as ultra-thin elastic films ([He et al., 2004](#), [Huang, 2008](#)), soft elastic nano-materials ([He and Lim, 2006](#)), nano-scale elastic layers ([Rungamornrat et al., 2016](#), [Intarit et al., 2018](#)), functionally graded nano-plates ([Ansari and Norouzzadeh, 2016](#), [Norouzzadeh and Ansari, 2018](#)), and nano-sized cracks ([Nguyen et al., 2015](#), [Nguyen et al., 2016](#), [Intarit et al., 2017](#)). Its popularity stems not only from its capability to capture the size dependency resulting from the presence of the surface energy but also its relatively simple mathematical foundation based upon the continuum assumption of matter. In addition, past evidence has clearly indicated that continuum-based models enhanced by incorporating G-M surface elasticity can yield results in good agreement with that obtained directly from

atomistic (Miller and Shenoy, 2000, Shenoy, 2005, Shenoy, 2002) or molecular dynamics simulations (Zhou and Huang, 2004).

1.2.2. Layered media under surface loading

Problems concerning a layered medium under surface loading are considered fundamental in solid mechanics. In addition to providing a profound understanding of mechanical behavior and a useful means to assess certain properties of the medium, results obtained from such problems can be further used as essential basis for solving contact problems. Within the context of nano-scale modeling, investigations of the surface loading on layered media by taking into account the surface energy via Gurtin-Murdoch model have been increasingly found for the past two decades. For instance, Wang and Feng (2007) examined the effect of surface stresses on an elastic half-plane subjected to either a uniformly distributed surface pressure or a concentrated surface force by adopting the Fourier integral transforms method to derive the general solution. This study resulted in some interesting characteristics mechanical behavior in comparison with those in classical theory; however, only the residual surface tension was considered in the simulation while the surface elastic constants were ignored which leads to an extended study conducted by Huang and Yu (2007). By taking into account the surface effect with both residual and elastic surface constants, the displacement Green's function of an elastic half-plane subjected to a concentrated surface force in either normal or tangential direction was obtained by using the Fourier integral transforms. Zhao and Rajapakse (2009) and Zhao and Rajapakse (2013) investigated a problem of an infinite elastic layer bonded to the rigid base and subjected to distributed surface load by considering the surface energy effect but ignoring the out-of-plane contribution of the residual surface tension. The method of integral transforms was employed together with Love's representation in the solution procedure. The out-of-plane contribution of the residual surface tension in Gurtin-Murdoch model was also neglected in the modeling of dislocations and internal loadings in an elastic half-plane by Intarit et al. (2010). Since the residual surface tension, especially the contribution in the out-of-plane direction, significantly influences the apparent stiffness of the medium, a similar study of the buried load in

an infinite elastic layer was later conducted by [Intarit et al. \(2011\)](#) with the use of a complete version of Gurtin-Murdoch model.

Recently, the modeling of layered media under surface loadings and accounting for the complete Gurtin-Murdoch elasticity theory was extensively conducted for various scenarios such as an infinite rigid-based elastic layer subjected to axisymmetric surface loads ([Rungamornrat et al., 2016](#)), a layered elastic half-space under axisymmetric surface loads ([Tirapat et al., 2017](#)), and an elastic half-plane subjected to a circular shear traction on the surface ([Mi, 2017](#)). Solution procedures implemented for all those problems were based solely on analytical and quasi-analytical techniques; in particular, analytical expressions for an elastic field induced within the medium were derived based on Hankel integral transform together with Love's representation ([Rungamornrat et al., 2016](#), [Tirapat et al., 2017](#)) and Boussinesq potential ([Mi, 2017](#)) and the evaluation of those expressions was carried out via selected numerical quadratures. Note in addition that results from an extensive parametric study indicate the important role of the residual surface tension in enhancing material stiffness relative to the classical case and the case where the out-of-plane contribution of the residual surface tension was fully ignored. This leads to the conclusion that the complete version of Gurtin-Murdoch constitutive law should be employed to simulate the surface effect of nano-scale problems. Also, it has been observed that the predicted response of materials is strongly size-dependent when the size of a loading region is comparable to the intrinsic length scale of the material.

The most recent research on the investigation of mechanical responses of three-dimensional elastic layered media under axisymmetric surface loading with the consideration of surface energy effects was conducted by [Tarnkira \(2018\)](#). In this work, the medium was modeled as multiple homogeneous layers of constant thickness perfectly bonded at the interface. The material surface and interfaces were treated by a complete Gurtin-Murdoch surface elasticity theory. An analytical technique based upon Love's strain potential and Hankel integral transform was employed to derive the general solution and the exact stiffness for each generic layer in the transform space, and a standard assembly procedure was then adopted together with the interface equations to obtain the system of equations governing the whole medium.

While the work of [Tarntira \(2018\)](#) has the capability to treat a layered medium consisting of arbitrary number of layers, the solution procedure employed raises certain important issues related to the computational efficiency when dealing with large scale problems and the practical application to treat functionally graded material layers. More powerful solution techniques are still required to further upgrade the modeling capability of simulating multi-layered media with a set of general data.

1.2.3. Contact on layered media

Surface indentation has become a well-known technique commonly utilized to investigate the mechanical behavior and to measure certain properties of nano-scale materials and structures. Attempt has been significantly invested, in the past decades, to develop physically sound mathematical models together with the solution methodology to be capable of simulating such physical phenomena up to the level of complexity involved. According to the past studies, several researchers were interested in measuring the elastic properties of the film-on-substrate subjected to various axisymmetric indenters by using various existing techniques including Hankel integral transform ([Yu et al., 1990](#), [Yang, 1998](#)) and the surface displacement Green's function ([Gao et al., 2008](#)). These studies provide uniquely useful guideline in the evaluation of elastic properties from the appropriate film thickness and substrate selection ([Yu et al., 1990](#)), from applied load and penetration depth relationship, and from the surface traction and surface displacement relationship ([Gao et al., 2008](#)). However, results obtained from those studies can be incomparable to actual response since the surface effects are fully ignored in the modeling.

The incorporation of Gurtin-Murdoch surface elasticity theory to further enhance the existing classical continuum-based model for the investigation of an elastic half-space indented by axisymmetric, rigid, frictionless, nano-size punches was first established by [Zhao \(2009\)](#). In this work, a solution technique based on Love's strain potential, Hankel integral transform and Fredholm integral equation is adopted to derive elastic field within the half-space. Although the influence of the surface stresses on the material response and the size-dependent behavior of predicted solutions were clearly observed, the out of plane contribution of the residual surface tension in Gurtin-Murdoch model was still ignored. Later, [Pinyochotiwong et al.](#)

(2013) investigated the same problem as Zhao (2009) but employed the complete version of Gurtin-Murdoch surface elasticity theory in their formulation. In the analysis, a solution technique similar to that employed by Zhao (2009) was adopted. It was demonstrated that the influence of the residual surface tension on the predicted response is more pronounced when its out-of-plane contribution is included. Intarit et al. (2018) studied the influence of the surface energy effect on the mechanical response of an infinite elastic layer rested on a rigid foundation and compressed by axisymmetric, rigid, frictionless, nano-size indentors. Fundamental results established by Rungamornrat et al. (2016) was employed as the basis in the formulation of the governing integral equation and a collocation technique equipped with an efficient numerical quadrature was adopted in the solution procedure. Most recently, Tirapat and Senjuntichai (2018) formulated the problem of axisymmetric frictionless rigid indenter on a layered medium as a mixed boundary value problem of which the displacement under the punch is imposed whereas the contact pressure is determined from discretization with the use of displacement Green's function and Hankel integral transform. Results from the past studies confirmed that the medium becomes stiffer when the surface stresses are taken into account and, moreover, the surface effect is more significant when the internal length scale of the material is comparable to the external length scale of the problem. It is worth noting that solution techniques employed in all studies mentioned above are quite limited in nature and their capability and computational efficiency, when applied to treat more general problems such as indentations on multi-layer or functionally graded layer media, is still questionable. To overcome such concern, Attia and Mahmoud (2015) adopted the finite element method to solve a functionally graded film layer rested on an elastic layer subjected to either a rigid or deformable indenter with arbitrary profiles. The influence of surface stresses was treated by the complete Gurtin-Murdoch surface elasticity model. In addition to the significance of the surface contribution and the size dependency observed, such study also revealed the essential influence of a film's gradation parameter on the response of the contact problem. While the numerical technique proposed by Attia and Mahmoud (2015) allows a set of more general data to be easily treated in comparison with those employed by Zhao (2009), Pinyochotiwong et al. (2013), Intarit et al. (2018), and Tirapat and Senjuntichai

(2018) an issue of the computational efficiency also arises when an infinite, multi-layer medium is of interest. This clearly leaves a plenty of room for the enhancement of the solution procedure to further boost the modeling capability of the nano-scale layered media.

1.2.4. Scaled Boundary Finite Element Method

The scaled boundary finite element method (SBFEM) was firstly introduced in 1990s by wolf and Song (Wolf and Song, 1995a, Wolf and Song, 1995b, Wolf and Song, 1996). The original purpose of SBFEM development is to analyze the dynamic semi-infinite medium-structure interaction based on mechanically based derivation. The feature of SBFEM is that the boundary in the circumferential direction is discretized into a number of certain elements, leading to governing linear ordinary differential equation in radial direction whose constant coefficients is defined by finite element approximation in circumferential direction. However, the mathematical formulation of the original work is still complicated.

To overcome such drawback and to prove that the so-called SBFEM is computationally efficient, the original SBFEM formulation was rederived by employing the weighted residual technique (Song and Wolf, 1997, Wolf and Song, 2000, Wolf and Song, 2001) and virtual work principle (Deeks and Wolf, 2002b). In return, the SBFEM become more computationally efficient and even more general than FEM for unbounded domain problems involving stress singularity (Deeks and Wolf, 2002a). The efficiency and accuracy of the so-called SBFEM has been found in several engineering problems including crack problems (Ooi et al., 2012, Ooi et al., 2013, Chowdhury et al., 2014, Dai et al., 2015), wave propagation (Li et al., 2013b, Li et al., 2013c, Meng and Zou, 2013, Gravenkamp et al., 2014). Although the efficiency of SBFEM is better than another existing method for certain problems, the SBFEM still cost some computational expense for problems involving a large number of degrees of freedom.

To streamline the accuracy and efficiency of SBFEM as well as to broaden its application, several techniques have been integrated into standard SBFEM. With the incorporation of h -hierarchical adaptive procedure, the computational time was considerably reduced in comparison with finite element method (Deeks and Wolf,

2002a). Deeks and Augarde (2005) developed a meshless local Petrov-Galerkin scale boundary method (MLPG-SBM) to implement the solution convergence. As a result, the MLPG-SBM converge faster than the conventional SBFEM due to the increase of smoothness and continuity of shape function. Higher-order shape functions, generated from two different techniques, the spectral element and hierarchical approach, was considered in SBFEM (Vu and Deeks, 2006). According to this study, the higher-order elements generated from spectral element approach is more efficient than that generated from the hierarchical approach. Vu and Deeks (2008) integrated a p -adaptive mesh optimization into SBFEM in order to maximize the solution accuracy and to minimize the computational cost and also demonstrated that the convergence of the p -adaptive SBFEM increased faster than the h -adaptive SBFEM. The SBFEM accuracy also improves when element-free Galerkin approach is used in the circumferential direction (He et al., 2013a). Beside using polynomial shape function, He et al. (2014) introduced Fourier shape function into SBFEM and investigate its performance. The accuracy and convergence of the method were evaluated by numerical studies of elasto-static and heat transferred problems and was shown to be more efficient in comparison with polynomial shape function or element-free Galerkin method.

The potential of SBFEM in solving complicated engineering problems, unbounded domains, variation of material properties and loading, was remarkably recognized and considerably raise the application. Recently, several engineering problems have been efficiently solved and accurately investigated by employing the SBFEM including electrostatic problem (Liu and Lin, 2012), piezoelectric materials (Li et al., 2013a, Li et al., 2014), cyclically symmetric problem (He et al., 2013b), concentrated load on elastic medium (Vu and Deeks, 2014), two-dimensional linear multi-field media (Nguyen Van et al., 2017), etc. Based on such versatility, accuracy, and efficiency, the scaled boundary finite element method would be very suitable and become a better computationally efficient technique in investigating the mechanical behavior of infinite layered elastic medium in comparison with analytical technique (Rungamornrat et al., 2016, Tirapat et al., 2017, Tarntira, 2018) and the standard finite element method (Attia and Mahmoud, 2015).

1.3. Objective

The objective of the present study is to implement a numerical technique based on the scaled boundary finite element method for determining mechanical response of a nano-scale layered medium under prescribed surface loading.

1.4. Scope of Work

The present work is to be carried out within the following scope:

- (i) a medium is assumed two-dimensional, subjected to plane-strain condition, free of body force, and consists of multiple infinite layers of uniform thickness adhered perfectly at interfaces;
- (ii) a bulk material of each layer is isotropic, linearly elastic and can be either homogeneous or functionally graded in the direction perpendicular to the layer;
- (iii) material surface and interfaces are governed by Gurtin-Murdoch model with constant surface parameters; and
- (iv) a medium is excited only by a surface loading expressible as a linear combination of polynomial functions.

1.5. Methodology

The primary concern of this research is the implementation of a numerical procedure based on the scaled boundary finite element method and its application to investigate the mechanical response of a nano-scale layered medium under the action of surface loading. To achieve such tasks, the following key methodology and research procedure are proposed as follows.

- (i) A classical theory of linear elasticity ([Timoshenko and Goodier, 1970](#), [Gurtin, 1973](#), [Karasudhi, 2012](#)) is adopted to form basic field equations for the bulk material of each layer whereas Gurtin-Murdoch surface elasticity theory ([Gurtin and Murdoch, 1975](#), [Gurtin and Murdoch, 1978](#)) is employed to model the material surface and interfaces between bulk layers.
- (ii) For the bulk material of each layer, a standard weighted residual technique together with the integration-by-parts procedure is adopted to derive the governing weak-form statement. The scaling coordinate (along the infinite direction of the layer) and the boundary coordinate (along the direction

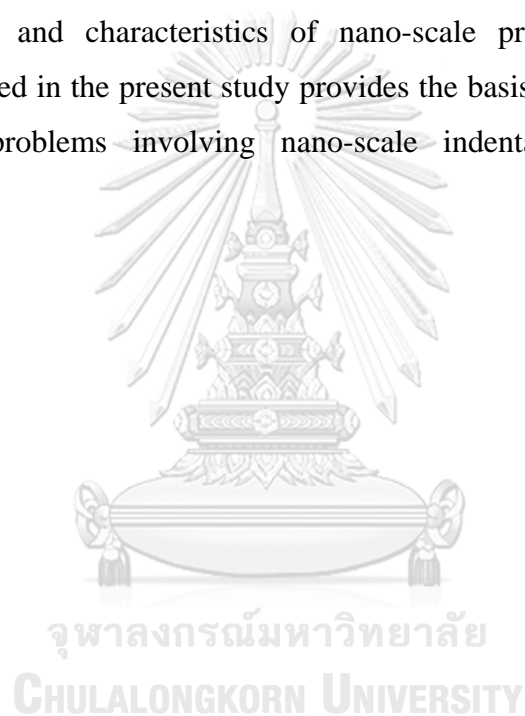
perpendicular to the layer) are first introduced and the finite element approximation of the displacement field is applied along the boundary coordinate direction. A set of linear, second-order, ordinary differential equations governing the nodal functions along the scaling coordinate together with the boundary conditions can then be obtained from the weak-form statement via the introduction of the scaled boundary finite element approximation and the integration-by-parts procedure.

- (iii) For the material surface and interfaces, a set of linear, second-order, ordinary differential equations in terms of the surface/interface displacements and the corresponding boundary conditions are established based on Gurtin-Murdoch model.
- (iv) A system of linear, second-order, non-homogeneous, ordinary differential equations and the corresponding boundary conditions for the whole layered medium can be obtained by combining governing equations for each bulk layer established in (ii), governing equations of material surface and interfaces from (iii), the boundary conditions corresponding to the prescribed surface loading, and the continuity of the displacement and traction at the material interfaces.
- (v) A homogeneous solution of the system of differential equations obtained in (iv) is obtained by a standard technique in the theory of differential equations and such a procedure leads to solving an equivalent linear eigenvalue problem. An efficient numerical algorithm based on the polynomial root-finder is adopted to obtain all eigenvalues and eigenvectors.
- (vi) A particular solution of the system of differential equations obtained in (iv) is obtained by adopting the method of undetermined coefficients.
- (vii) A set of boundary conditions is then employed together with the obtained general solution to obtain a system of linear algebraic equations governing the nodal degrees of freedom along the boundary coordinate direction.
- (viii) Once the nodal degrees of freedom are solved, the displacements and stresses within the layered medium are post-processed via the direct substitution.
- (ix) A numerical procedure is implemented by using MATLAB

- (x) The accuracy, efficiency and capability of the implemented numerical procedure is then tested by benchmarking obtained results with reliable reference solutions available in the literature.

1.6. Outcome and Contribution

The proposed study offers a computationally efficient and robust numerical technique for simulating a nano-scale layered medium subjected to a set of general data and fully equipped with Gurtin-Murdoch surface elasticity model. A fully tested, in-house computer code of such high capability should assist ones to further explore the essential features and characteristics of nano-scale problems. In addition, the technique developed in the present study provides the basis for the extension to solve more complex problems involving nano-scale indentation of layered media.



CHAPTER 2

FORMULATION

This chapter provides a clear description of the research problem, a set of two-dimensional basic governing equations for the bulk and material surface, and the formulation of key governing equations for the whole layered medium based on the concept of scaled boundary finite element approximation.

2.1. Problem Description

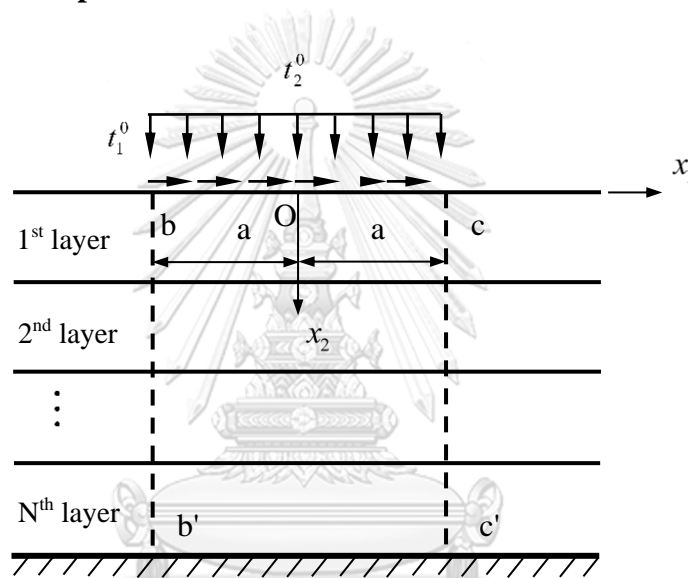


Figure 1: Schematic of a two-dimensional, multi-layer body subjected to the arbitrary loading at the top surface

Consider a two-dimensional, infinite, layered medium rested on a rigid foundation as shown schematically in Figure 1. The medium consists of N layers of uniform thickness and all layers are bonded rigidly at the material interfaces. The bulk of each layer is made of an isotropic, linearly elastic material whose properties can either be homogeneous or vary across the thickness. The latter allows the treatment of a functionally graded layer. The material surface of the top layer and the material interfaces between any two consecutive layers possess their own properties different from those of the bulk; in particular, both the residual surface tension and the surface elastic constants are fully prescribed and assumed homogenous. The layered medium

is free of the body force and subjected only to arbitrarily distributed traction on the surface of the top layer over the length $2a$. The infinite layered media can be divided into three sub-domains along the lines bb' and cc' and they are referred to the left part, the center part, and the right part. Then, in the formulation, the representative layered medium with a similar shape as that of the center part is considered. Once the formulation is achieved on representative domain, it can be readily applied to all subdomains of left, center, and right parts. For instance, formulation of the left part is obtained from representative domain by taking the left boundary of the representative domain to infinity and removing all loading on the boundary of the top surface.

The statement of the research problem is to develop an efficient solution procedure for determining an elastic field within the layered medium under applied surface loading and the influence of surface stresses on the material surface/interfaces. For convenience in further development, a two-dimensional, Cartesian coordinate system $\{0, x_1, x_2\}$ is introduced as shown in Figure 1.

2.2. Governing Equations for Generic Layer

To formulate a set of governing equations for the representative layered medium, it suffices to establish the governing equations for a generic bulk layer of finite thickness and finite length, called the k^{th} bulk layer and denoted by a rectangular region Ω , and a generic material surface/interface, called the k^{th} surface and denoted by a straight line s , as shown in Figure 2.

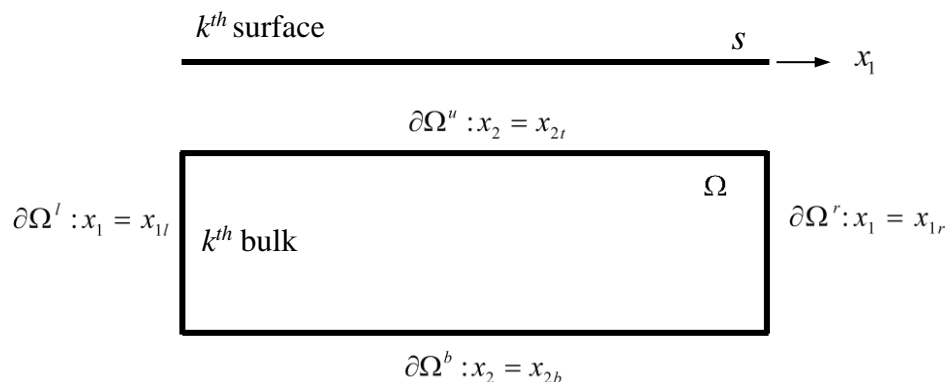


Figure 2: Schematic of the k^{th} surface and the k^{th} bulk layer

The boundary of the k^{th} bulk layer is denoted by $\partial\Omega$ and it can be decomposed into $\partial\Omega = \partial\Omega^l \cup \partial\Omega^r \cup \partial\Omega^b \cup \partial\Omega^u$ where $\partial\Omega^l$, $\partial\Omega^r$, $\partial\Omega^b$ and $\partial\Omega^u$ denote the left, right, bottom and top boundaries, respectively. The k^{th} surface is treated as a zero-thickness, material line whose properties are different from those of the bulk. For $k=1$, it represents the material surface on the top of the top layer whereas for $k=2,3,\dots,N$, it represents the material interface between the $(k-1)^{th}$ bulk layer and k^{th} bulk layer.

2.2.1. Governing Equation for Bulk Layer

From the classical theory of linear elasticity, equilibrium equations, stress-strain relationship, and strain-displacement relationship can be expressed in a concise form, for a two-dimensional body subjected to the plane-strain condition and zero body force, as

$$\mathbf{L}^T \boldsymbol{\sigma}^b = 0 \quad (2.1)$$

$$\boldsymbol{\sigma}^b = \mathbf{D} \boldsymbol{\varepsilon}^b \quad (2.2)$$

$$\boldsymbol{\varepsilon}^b = \mathbf{L} \mathbf{u}^b \quad (2.3)$$

where $\boldsymbol{\sigma}^b$, $\boldsymbol{\varepsilon}^b$, \mathbf{u}^b , \mathbf{D} and \mathbf{L} denoting, respectively, a vector containing in-plane stress components, a vector containing in-plane strain components, a vector containing in-plane displacement components, a modulus matrix involving material constants, and a two-dimensional, linear differential operator are defined explicitly by

$$\boldsymbol{\sigma}^b = \begin{Bmatrix} \sigma_{11}^b \\ \sigma_{22}^b \\ \sigma_{12}^b \end{Bmatrix}, \boldsymbol{\varepsilon}^b = \begin{Bmatrix} \varepsilon_{11}^b \\ \varepsilon_{22}^b \\ \varepsilon_{12}^b \end{Bmatrix}, \mathbf{u}^b = \begin{Bmatrix} u_1^b \\ u_2^b \end{Bmatrix}, \mathbf{D} = \frac{\mu}{\kappa-1} \begin{bmatrix} \kappa+1 & 3-\kappa & 0 \\ 3-\kappa & \kappa+1 & 0 \\ 0 & 0 & \kappa-1 \end{bmatrix} \quad (2.4)$$

$$\mathbf{L} = \begin{bmatrix} \partial/\partial x_1 & 0 \\ 0 & \partial/\partial x_2 \\ \partial/\partial x_2 & \partial/\partial x_1 \end{bmatrix} \quad (2.5)$$

where μ is the elastic shear modulus of the bulk layer and $\kappa = 3 - 4\nu$ with ν denoting Poisson's ratio. It is important to remark here that the superscript “ T ” appearing in (2.1) denotes the matrix transpose operator and the superscript “ b ” is used to designate quantities associated with the bulk. Note also that in-plane components of the displacement, stress and strain follow standard notation and the reference coordinate system shown in Figure 1. The linear differential operator \mathbf{L} can be further decomposed into

$$\mathbf{L} = \mathbf{b}_1 \frac{\partial}{\partial x_1} + \mathbf{b}_2 \frac{\partial}{\partial x_2} \quad (2.6)$$

where \mathbf{b}_1 and \mathbf{b}_2 are constant matrices defined explicitly by

$$\mathbf{b}_1 = \begin{bmatrix} 1 & 0 \\ 0 & 0 \\ 0 & 1 \end{bmatrix}, \quad \mathbf{b}_2 = \begin{bmatrix} 0 & 0 \\ 0 & 1 \\ 1 & 0 \end{bmatrix} \quad (2.7)$$

The traction $\mathbf{t}^{b(\partial\Omega)}$ acting to the boundary $\partial\Omega$ can be expressed in terms of the stress field of the bulk layer at its boundary $\boldsymbol{\sigma}^{b(\partial\Omega)}$ and the corresponding unit normal vector \mathbf{n} such that

$$\mathbf{t}^{b(\partial\Omega)} = \boldsymbol{\sigma}^{b(\partial\Omega)} \mathbf{n} \quad (2.8)$$

The equilibrium equation (2.1), the constitutive law (2.2), and the strain-displacement relation (2.3) can be combined to obtain

$$\mathbf{L}^T \mathbf{D} \mathbf{L} \mathbf{u}^b = 0 \quad (2.9)$$

By applying the standard weighted residual technique together with the integration by parts and the corresponding traction boundary condition, the alternative weak statement of equation (2.9) is given by

$$\int_{\Omega} (\mathbf{L} \mathbf{w})^T \mathbf{D} (\mathbf{L} \mathbf{u}^b) dA = \int_{\partial\Omega} \mathbf{w}^T \mathbf{t}^{b(\partial\Omega)} ds \quad (2.10)$$

where \mathbf{w} is any weight function satisfying the following integrability condition

$$\int_{\Omega} (\mathbf{L}\mathbf{w})^T (\mathbf{L}\mathbf{w}) dA < \infty \quad (2.11)$$

2.2.1.1. Scaled Boundary Finite Element Approximation

Let one introduce the scaled boundary finite element approximation of the displacement field \mathbf{u}^b and the weight function \mathbf{w} such that

$$\mathbf{u}^h = \mathbf{u}^h(x_1, x_2) = \sum_{i=1}^p \phi^{(i)}(x_2) \mathbf{u}^{(i)}(x_1) = \mathbf{N}\mathbf{U}^h \quad (2.12)$$

$$\mathbf{w}^h = \mathbf{w}^h(x_1, x_2) = \sum_{i=1}^p \phi^{(i)}(x_2) \mathbf{w}^{(i)}(x_1) = \mathbf{N}\mathbf{W}^h \quad (2.13)$$

where p denotes the number of nodal points along the approximate direction; $\phi^{(i)}$ indicates the i^{th} nodal basis function defined along the x_2 -direction; $\mathbf{u}^{(i)} = \{u_1^i \ u_2^i\}^T$ and $\mathbf{w}^{(i)} = \{w_1^i \ w_2^i\}^T$ represent the i^{th} nodal displacement vector and i^{th} arbitrary nodal weight function defined in terms of x_1 , respectively; and the matrix \mathbf{N} and the two vectors \mathbf{U}^h and \mathbf{W}^h are defined by

$$\mathbf{N} = \mathbf{N}(x_2) = \begin{bmatrix} \phi^{(1)} & 0 & \phi^{(2)} & 0 & \dots & \phi^{(p)} & 0 \\ 0 & \phi^{(1)} & 0 & \phi^{(2)} & \dots & 0 & \phi^{(p)} \end{bmatrix} \quad (2.14)$$

$$\mathbf{U}^h = \mathbf{U}^h(x_1) = \{u_1^{(1)} \ u_2^{(1)} \ u_1^{(2)} \ u_2^{(2)} \ \dots \ u_1^{(p)} \ u_2^{(p)}\}^T \quad (2.15)$$

$$\mathbf{W}^h = \mathbf{W}^h(x_1) = \{w_1^{(1)} \ w_2^{(1)} \ w_1^{(2)} \ w_2^{(2)} \ \dots \ w_1^{(p)} \ w_2^{(p)}\}^T \quad (2.16)$$

By employing the approximations (2.14)-(2.16) together with the operator (2.6), the terms $\mathbf{L}\mathbf{w}$ and $\mathbf{L}\mathbf{u}^b$ can be approximated by

$$\mathbf{L}\mathbf{w}^h = \left(\mathbf{b}_1 \frac{\partial}{\partial x_1} + \mathbf{b}_2 \frac{\partial}{\partial x_2} \right) \mathbf{N}\mathbf{W}^h = \mathbf{b}_1 \mathbf{N}' (\mathbf{W}^h)' + \mathbf{b}_2 \mathbf{B}\mathbf{W}^h \quad (2.17)$$

$$\mathbf{L}u^h = \left(\mathbf{b}_1 \frac{\partial}{\partial x_1} + \mathbf{b}_2 \frac{\partial}{\partial x_2} \right) \mathbf{N}U^h = \mathbf{b}_1 \mathbf{N}'(U^h)' + \mathbf{b}_2 \mathbf{B}U^h \quad (2.18)$$

where $(\cdot)'$ denotes the ordinary derivative with respect to the coordinate x_1 and the matrix \mathbf{B} is defined by

$$\mathbf{B} = \frac{d\mathbf{N}}{dx_2} \quad (2.19)$$

2.2.1.2. Scaled Boundary Finite Element Equations

By introducing the approximations (2.17) and (2.18) into the weak-form statement (2.10), it gives rise to

$$\begin{aligned} & \int_{\Omega} (\mathbf{W}^h)'^T (\mathbf{N}^T \mathbf{b}_1^T \mathbf{D} \mathbf{b}_1 \mathbf{N}) U^h' dA + \int_{\Omega} (\mathbf{W}^h)'^T (\mathbf{N}^T \mathbf{b}_1^T \mathbf{D} \mathbf{b}_2 \mathbf{B}) U^h dA + \\ & \int_{\Omega} (\mathbf{W}^h)^T (\mathbf{B}^T \mathbf{b}_2^T \mathbf{D} \mathbf{b}_1 \mathbf{N}) U^h' dA + \int_{\Omega} (\mathbf{W}^h)^T (\mathbf{B}^T \mathbf{b}_2^T \mathbf{D} \mathbf{b}_2 \mathbf{B}) U^h dA = \\ & \int_{\partial\Omega} (\mathbf{W}^h)^T \mathbf{N}^T \mathbf{t}^{b(\partial\Omega)} ds \end{aligned} \quad (2.20)$$

Upon using the fact that the terms in the second parentheses appearing in (2.20) are only functions of the coordinate x_2 together with the partition of the boundary $\partial\Omega = \partial\Omega^l \cup \partial\Omega^r \cup \partial\Omega^b \cup \partial\Omega^u$, the relation (2.20) now becomes

$$\begin{aligned} & \int_{x_{1l}}^{x_{1r}} (\mathbf{W}^h)'^T \mathbf{E}_2^b U^h' dx_1 + \int_{x_{1l}}^{x_{1r}} (\mathbf{W}^h)'^T \mathbf{E}_1^b U^h dx_1 + \int_{x_{1l}}^{x_{1r}} (\mathbf{W}^h)^T (\mathbf{E}_1^b)^T U^h' dx_1 \\ & + \int_{x_{1l}}^{x_{1r}} (\mathbf{W}^h)^T \mathbf{E}_0^b U^h dx_1 = \int_{x_{1l}}^{x_{1r}} (\mathbf{W}^h)^T (\mathbf{T}^u + \mathbf{T}^b) dx_1 + (\mathbf{W}^{hr})^T \mathbf{P}^r + (\mathbf{W}^{hl})^T \mathbf{P}^l \end{aligned} \quad (2.21)$$

where

$$\mathbf{E}_0^b = \int_{x_{2b}}^{x_{2u}} \mathbf{B}^T \mathbf{b}_2^T \mathbf{D} \mathbf{b}_2 \mathbf{B} dx_2 \quad (2.22)$$

$$\mathbf{E}_1^b = \int_{x_{2b}}^{x_{2u}} \mathbf{N}^T \mathbf{b}_1^T \mathbf{D} \mathbf{b}_2 \mathbf{B} dx_2 \quad (2.23)$$

$$\mathbf{E}_2^b = \int_{x_{2b}}^{x_{2u}} \mathbf{N}^T \mathbf{b}_1^T \mathbf{D} \mathbf{b}_1 \mathbf{N} dx_2 \quad (2.24)$$

$$\mathbf{T}^u = \mathbf{T}^u(x_1) = \mathbf{N}^T(x_{2u}) \mathbf{t}^u(x_1), \mathbf{T}^b = \mathbf{T}^b(x_1) = \mathbf{N}^T(x_{2b}) \mathbf{t}^b(x_1) \quad (2.25)$$

$$\mathbf{P}^r = \int_{x_{2b}}^{x_{2u}} \mathbf{N}^T(x_2) \mathbf{t}^r(x_2) dx_2, \mathbf{P}^l = \int_{x_{2b}}^{x_{2u}} \mathbf{N}^T(x_2) \mathbf{t}^l(x_2) dx_2 \quad (2.26)$$

$$\mathbf{W}^{hr} = \mathbf{W}^h(x_{1r}), \mathbf{W}^{hl} = \mathbf{W}^h(x_{1l}) \quad (2.27)$$

Since the integrands of integrals in (2.22)-(2.24) are only functions of the coordinate x_2 , the matrices \mathbf{E}_0^b , \mathbf{E}_1^b and \mathbf{E}_2^b are constant and their dimensions depend primarily on the number of nodal points along the approximate direction. Next, by integrating the first and second integrals on the left-hand side of (2.21) by parts, it leads to

$$\begin{aligned} \int_{x_{1l}}^{x_{1r}} (\mathbf{W}^h)^T \mathbf{E}_2^b \mathbf{U}^h{}' dx_1 &= \int_{x_{1l}}^{x_{1r}} [((\mathbf{W}^h)^T \mathbf{E}_2^b \mathbf{U}^h)' - (\mathbf{W}^h)^T \mathbf{E}_2^b \mathbf{U}^h{}''] dx_1 \\ &= (\mathbf{W}^{hr})^T \mathbf{E}_2^b \mathbf{U}^h{}'(x_{1r}) - (\mathbf{W}^{hl})^T \mathbf{E}_2^b \mathbf{U}^h{}'(x_{1l}) - \int_{x_{1l}}^{x_{1r}} (\mathbf{W}^h)^T \mathbf{E}_2^b \mathbf{U}^h{}'' dx_1 \end{aligned} \quad (2.28)$$

$$\begin{aligned} \int_{x_{1l}}^{x_{1r}} (\mathbf{W}^h)^T \mathbf{E}_1^b \mathbf{U}^h dx_1 &= \int_{x_{1l}}^{x_{1r}} [((\mathbf{W}^h)^T \mathbf{E}_1^b \mathbf{U}^h)' - (\mathbf{W}^h)^T \mathbf{E}_1^b \mathbf{U}^h{}'] dx_1 \\ &= (\mathbf{W}^{hr})^T \mathbf{E}_1^b \mathbf{U}^h(x_{1r}) - (\mathbf{W}^{hl})^T \mathbf{E}_1^b \mathbf{U}^h{}'(x_{1l}) - \int_{x_{1l}}^{x_{1r}} (\mathbf{W}^h)^T \mathbf{E}_1^b \mathbf{U}^h{}' dx_1 \end{aligned} \quad (2.29)$$

By substituting the results (2.28) and (2.29) into (2.21), it results in

$$\begin{aligned}
& \int_{x_{1l}}^{x_{1r}} (\mathbf{W}^h)^T \{ \mathbf{E}_2^b \mathbf{U}^{h''} + [\mathbf{E}_1^b - (\mathbf{E}_1^b)^T] \mathbf{U}^{h'} - \mathbf{E}_0^b \mathbf{U}^h + \mathbf{T}^u + \mathbf{T}^b \} dx_1 \\
& = (\mathbf{W}^{hr})^T [-\mathbf{P}^r + \mathbf{Q}^b(x_{1r})] + (\mathbf{W}^{hl})^T [-\mathbf{P}^l - \mathbf{Q}^b(x_{1l})]
\end{aligned} \tag{2.30}$$

where the matrix \mathbf{Q}^b denotes the nodal internal flux defined by

$$\mathbf{Q}^b = \mathbf{Q}^b(x_1) = \mathbf{E}_1^b \mathbf{U}^h(x_1) + \mathbf{E}_2^b \mathbf{U}^{h'}(x_1) \tag{2.31}$$

Finally, by invoking the arbitrariness of the vector \mathbf{W} in (2.28), it leads to

$$\mathbf{E}_2^b \mathbf{U}^{h''} + [\mathbf{E}_1^b - (\mathbf{E}_1^b)^T] \mathbf{U}^{h'} - \mathbf{E}_0^b \mathbf{U}^h + \mathbf{T}^u + \mathbf{T}^b = 0 \tag{2.32}$$

$$\mathbf{Q}^b(x_{1l}) = -\mathbf{P}^l \tag{2.33}$$

$$\mathbf{Q}^b(x_{1r}) = \mathbf{P}^r \tag{2.34}$$

Note that equation (2.32) is a system of fully coupled, linear, second-order ordinary differential equations governing the unknown nodal functions \mathbf{U}^h whereas (2.33) and (2.34) represent the boundary conditions on left and right boundaries of the bulk layer.

2.2.2. Governing Equation for Material Surface/Interface

The behavior of the material surface/interface is treated differently from the bulk according to the complete version of the surface elasticity theory introduced by (1975, Gurtin and Murdoch, 1978). In particular, the governing equations such as the surface equilibrium in terms of the generalized Young-Laplace equation (Povstenko, 1993), surface constitutive law, and surface kinematics are expressed, for the one-dimensional case, as follows

$$\frac{\partial \sigma_{11}^s}{\partial x_1} + t_1^{su} + t_1^{sb} = 0, \quad \frac{\partial \sigma_{21}^s}{\partial x_1} + t_2^{su} + t_2^{sb} = 0 \tag{2.35}$$

$$\sigma_{11}^s = \tau^s + (2\mu^s + \lambda^s) \varepsilon_{11}^s, \quad \sigma_{21}^s = \tau^s \varepsilon_{21}^s \tag{2.36}$$

$$\varepsilon_{11}^s = \frac{\partial u_1^s}{\partial x_1}, \quad \varepsilon_{21}^s = \frac{\partial u_2^s}{\partial x_1} \quad (2.37)$$

where the superscript “s” is employed to emphasize the surface quantities; the material constants λ^s, μ^s and τ^s represent the surface Lamé constants and the residual surface tension, respectively; and t^{su} and t^{sb} denote the tractions acting to the top and bottom of the surface, respectively. By substituting the equation (2.36) and (2.37) into equation (2.35), the in-plane and out-of-plane equilibrium equations of the surface can be expressed, in terms of the surface displacement, as

$$\mathbf{E}^s (\mathbf{U}^s)' + t^{su} + t^{sb} = \mathbf{0} \quad (2.38)$$

where

$$\mathbf{E}^s = \begin{bmatrix} (2\mu^s + \lambda^s) & 0 \\ 0 & \tau^s \end{bmatrix}, \quad t^{su} = \begin{Bmatrix} t_1^{su} \\ t_2^{su} \end{Bmatrix}, \quad t^{sb} = \begin{Bmatrix} t_1^{sb} \\ t_2^{sb} \end{Bmatrix}, \quad \mathbf{U}^s = \begin{Bmatrix} u_1^s \\ u_2^s \end{Bmatrix} \quad (2.39)$$

The internal flux within the material surface/interface, denoted by \mathbf{Q}^s , is defined by

$$\mathbf{Q}^s = \mathbf{Q}^s(x_1) = \mathbf{E}^s \mathbf{U}^s'(x_1) \quad (2.40)$$

2.3. Governing Equation for Layered Medium

Since the $(k-1)^{th}$ bulk layer, the k^{th} material interface and the k^{th} bulk layer (for $k=2,3,\dots,N$) are perfectly bonded without slipping, the displacement and traction along the interface of the surface must satisfy the following conditions

$$\begin{aligned} u_1^{b(k-1)}(x_2 = z_k) &= u_1^{s(k)}(x_2 = z_k) = u_1^{b(k)}(x_2 = z_k) \\ u_2^{b(k-1)}(x_2 = z_k) &= u_2^{s(k)}(x_2 = z_k) = u_2^{b(k)}(x_2 = z_k) \end{aligned} \quad (2.41)$$

$$t_1^{b(k-1)} + t_1^{s(k)} = 0; \quad t_2^{b(k-1)} + t_2^{s(k)} = 0 \quad (2.42)$$

$$t_1^{s(k)} + t_1^{b(k)} = 0; \quad t_2^{s(k)} + t_2^{b(k)} = 0 \quad (2.43)$$

Also, the boundary conditions at the top surface of the 1st layer and the bottom surface of the last layer are given by

$$t_1^0 + t_1^{s(1)} = 0, \quad t_2^0 + t_2^{s(1)} = 0 \quad (2.44)$$

$$u_1^{b(N)} = u_2^{b(N)} = 0 \quad (2.45)$$

with the use of conditions (2.41)-(2.45), equations (2.32) and (2.39) can be combined and the resulting system of equations is given by

$$\mathbf{E}_2^{bs} \mathbf{U}'' + [\mathbf{E}_1^{bb} - (\mathbf{E}_1^{bb})^T] \mathbf{U}' - \mathbf{E}_0^{bb} \mathbf{U} = \mathbf{t} \quad (2.46)$$

The corresponding internal flux, for the layered medium, now takes the form

$$\mathbf{Q} = \mathbf{Q}(x_1) = \mathbf{E}_1^{bb} \mathbf{U}(x_1) + \mathbf{E}_2^{bs} \mathbf{U}'(x_1) \quad (2.47)$$

where \mathbf{E}_2^{bs} , \mathbf{E}_1^{bb} and \mathbf{E}_0^{bb} are matrices containing material parameters resulting from the assembly of material surface/interfaces and the bulk layers and \mathbf{U} and \mathbf{t} are the nodal displacement vector and the vector containing the side-face traction, respectively. The matrices \mathbf{E}_2^{bs} , \mathbf{E}_1^{bb} and \mathbf{E}_0^{bb} and the vectors \mathbf{U} and \mathbf{t} are given explicitly, by

$$\mathbf{E}_2^{bs} = \begin{bmatrix} E_{11}^{b21} + E_{11}^{s1} & \cdots & 0 & \cdots & 0 \\ \vdots & \vdots & \vdots & \vdots & \vdots \\ \cdots & E_{(2p-1)(2p-1)}^{b2k} + E_{11}^{sk} + E_{11}^{b2(k+1)} & \cdots & 0 \\ \vdots & \vdots & \vdots & \vdots & \vdots \\ 0 & \cdots & 0 & \cdots & E_{(2p)(2p)}^{b2N} \end{bmatrix} \quad (2.48)$$

$$\mathbf{E}_1^{bb} = \begin{bmatrix} E_{11}^{b11} & \cdots & 0 & \cdots & 0 \\ \vdots & \vdots & \vdots & \vdots & \vdots \\ 0 & \cdots & E_{(2p-1)(2p-1)}^{b1k} + E_{11}^{b1(k+1)} & \cdots & 0 \\ \vdots & \vdots & \vdots & \vdots & \vdots \\ 0 & \cdots & 0 & \cdots & E_{(2p)(2p)}^{b1N} \end{bmatrix} \quad (2.49)$$

$$\mathbf{E}_0^{bb} = \begin{bmatrix} E_{11}^{b01} & \cdots & 0 & \cdots & 0 \\ \vdots & \vdots & \vdots & \vdots & \vdots \\ 0 & \cdots & E_{(2p-1)(2p-1)}^{b0k} + E_{11}^{b0(k+1)} & \cdots & 0 \\ \vdots & \vdots & \vdots & \vdots & \vdots \\ 0 & \cdots & 0 & \cdots & E_{(2p)(2p)}^{b0N} \end{bmatrix} \quad (2.50)$$

$$\mathbf{U} = \{u_1 \quad u_2 \quad \cdots \quad u_{2k-1} \quad u_{2k} \quad \cdots \quad u_{2n-1} \quad u_{2n}\}^T \quad (2.51)$$

$$\mathbf{t} = \{t_1^0 \quad t_2^0 \quad \cdots \quad 0 \quad 0 \quad \cdots \quad R_1 \quad R_2\}^T \quad (2.52)$$

where N , p , n , R_1 and R_2 denote the number of layers, the number of nodes per bulk layer, the number of nodes for the entire body, the horizontal reaction, and the vertical reaction, respectively. It worth noting that the nodal displacement vector \mathbf{U} in (2.51) and the nodal traction vector \mathbf{t} in (2.52) can be partitioned into $\mathbf{U} = \{\mathbf{U}^f \quad \mathbf{U}^r\}^T$ and $\mathbf{t} = \{\mathbf{t}^f \quad \mathbf{t}^r\}^T$ where \mathbf{U}^f ; \mathbf{U}^r ; \mathbf{t}^f and \mathbf{t}^r are $2n-2$ components of the unknown nodal displacement vector, 2 components of prescribed nodal displacement vector, $2n-2$ components of applied nodal loading vector, and 2 components of unknown reaction vector, respectively. According to such partition, the system of equations (2.46) can be further separated into two sub-systems of equations such that

$$\mathbf{E}_2^{bsff} \mathbf{U}^{f''} + [\mathbf{E}_1^{bbff} - (\mathbf{E}_1^{bbff})^T] \mathbf{U}^{f'} - \mathbf{E}_0^{bbff} \mathbf{U}^f = \mathbf{t}^f \quad (2.53)$$

$$\mathbf{E}_2^{bsrf} \mathbf{U}^{f''} + [\mathbf{E}_1^{bbrf} - (\mathbf{E}_1^{bbrf})^T] \mathbf{U}^{f'} - \mathbf{E}_0^{bbrf} \mathbf{U}^f = \mathbf{t}^r \quad (2.54)$$

Similarly, the corresponding internal flux (2.47) gives rise to

$$\mathbf{Q}^f = \mathbf{Q}^f(x_1) = \mathbf{E}_1^{ff} \mathbf{U}^f(x_1) + \mathbf{E}_2^{bsff} \mathbf{U}^{f'}(x_1) \quad (2.55)$$

$$\mathbf{Q}^r = \mathbf{Q}^r(x_1) = \mathbf{E}_1^{bbrf} \mathbf{U}^f(x_1) + \mathbf{E}_2^{bsrf} \mathbf{U}^{f'}(x_1) \quad (2.56)$$

where \mathbf{E}_2^{bsff} , \mathbf{E}_2^{bsrf} , \mathbf{E}_1^{bbff} , \mathbf{E}_1^{bbrf} , \mathbf{E}_0^{bbff} , and \mathbf{E}_0^{bbrf} are sub-matrices resulting from the partition of the matrices \mathbf{E}_2^{bs} , \mathbf{E}_1^{bb} , and \mathbf{E}_0^{bb} consistent to the partition of the

displacement vector. The governing equation of (2.53) and its corresponding internal flux of equation (2.56) are sufficient to determine the unknown displacement vector \mathbf{U}^f . Once \mathbf{U}^f is solved, the reactions vector \mathbf{r}^r can be readily obtained via the direct substitution of \mathbf{U}^f into (2.54). Likewise, the solution of the nodal displacement \mathbf{U}^f can be further used to post-process for the stress field within representative layered medium via the relations (2.2) and (2.3).



CHAPTER 3

SOLUTION METHODOLOGY

This chapter presents a procedure used to construct the solution of a system of linear, nonhomogeneous, second-order ordinary differential equations supplied by a set of well-posed boundary conditions. The general solution can be separated into two parts, a homogenous solution and a particular solution. The homogeneous solution of a system of linear, second-order, differential equations is determined by solving the eigenvalue problem resulting from adopting the standard theory of differential equations with constant coefficients. In contrast, the particular solution is obtained by adopting the technique of undetermined coefficients which depends mainly on the form of applied traction on the free surface. Finally, by enforcing a set of boundary conditions, the stiffness equation governing the entire problem is derived.

3.1. Homogeneous Solution

Let U^{jh} be the homogeneous solution of the system of linear second order ordinary differential equation (2.53) which is determined by following the standard procedure in the theory of differential equation and takes the form

$$U^{jh}(x_1) = \sum_{i=1}^{4n-4} c_i e^{r_i x_1} \eta_i \quad (3.1)$$

where η_i and $c_i e^{r_i x_1}$ represent $2n-2$ components of the i^{th} mode shape vector and i^{th} modal coordinate respectively. In addition, c_i and r_i are the arbitrary constants corresponding the modal contribution of i^{th} mode and the i^{th} modal scaling factor respectively. By substituting equation (3.1), its first and second derivatives into the homogeneous equation of (2.53), it yields

$$\sum_{i=1}^{4n-4} c_i e^{r_i x_1} (r_i^2 \mathbf{E}_2^{bsff} + [\mathbf{E}_1^{bbff} - (\mathbf{E}_1^{bbff})^T] r_i - \mathbf{E}_0^{bbff}) \eta_i = 0 \quad (3.2)$$

Since $c_i e^{r_i x_1} \neq 0$, equation (3.2) can be reduced to

$$(r_i^2 \mathbf{E}_2^{bsff} + [\mathbf{E}_1^{bbff} - (\mathbf{E}_1^{bbff})^T] r_i - \mathbf{E}_0^{bbff}) \boldsymbol{\eta}_i = 0 \quad (3.3)$$

Equation (3.3) is the eigenvalue problem of which the eigenvector $\boldsymbol{\eta}_i$ can be determined from the corresponding eigenvalue r_i obtained from solving higher order of characteristic polynomial. To facilitate the computational effort, we again substitute equation (3.1) and its first derivative into the internal flux of equation (2.55). It then gives rise to

$$\mathbf{Q}^f(x_1) = \sum_{i=1}^{4n-4} c_i e^{r_i x_1} (r_i \mathbf{E}_2^{bsff} + \mathbf{E}_1^{bbff}) \boldsymbol{\eta}_i \quad (3.4)$$

By defining \mathbf{q}_i , the i^{th} modal internal flux, in terms of $\boldsymbol{\eta}_i$ as

$$\mathbf{q}_i = (r_i \mathbf{E}_2^{bsff} + \mathbf{E}_1^{bbff}) \boldsymbol{\eta}_i \quad (3.5)$$

it can be readily verified that

$$r_i \boldsymbol{\eta}_i = -(\mathbf{E}_2^{bsff})^{-1} \mathbf{E}_1^{bbff} \boldsymbol{\eta}_i + (\mathbf{E}_2^{bsff})^{-1} \mathbf{q}_i \quad (3.6)$$

where $(\mathbf{E}_2^{bsff})^{-1}$ denotes the inverse of \mathbf{E}_2^{bsff} . Similarly, by substituting equation (3.5) into equation (3.3), it then results in

$$r_i \mathbf{q}_i = [\mathbf{E}_0^{bbff} - (\mathbf{E}_2^{bsff})^{-1} \mathbf{E}_1^{bbff} (\mathbf{E}_1^{bbff})^T] \boldsymbol{\eta}_i + (\mathbf{E}_2^{bsff})^{-1} (\mathbf{E}_1^{bbff})^T \mathbf{q}_i \quad (3.7)$$

Now, by introducing a $4n-4$ vector \mathbf{V}_i and a constant matrix \mathbf{E} such that

$$\mathbf{V}_i = \{\boldsymbol{\eta}_i \quad \mathbf{q}_i\}^T \quad (3.8)$$

$$\mathbf{E} = \begin{bmatrix} -(\mathbf{E}_2^{bsff})^{-1} \mathbf{E}_1^{bbff} & (\mathbf{E}_2^{bsff})^{-1} \\ \mathbf{E}_0^{bbff} - (\mathbf{E}_1^{bbff})^T (\mathbf{E}_2^{bsff})^{-1} \mathbf{E}_1^{bbff} & (\mathbf{E}_1^{bbff})^T (\mathbf{E}_2^{bsff})^{-1} \end{bmatrix} \quad (3.9)$$

Equation (3.6) and (3.7) can be combined into a system of linear algebraic equations such that

$$r_i \mathbf{V}_i = \mathbf{E} \mathbf{V}_i \quad (3.10)$$

Now, eigenvalue r_i and eigenvector $\boldsymbol{\eta}_i$ can be obtained by solving a linear eigenvalue problem of equation (3.10) instead of solving the nonlinear equation (3.3). It should be noticed that the repeated indices in the equation (3.10) do not imply the summation over their range.

Nevertheless, the matrix \mathbf{E} is not symmetric; therefore, the obtained r_i and \mathbf{V}_i can be complex numbers. Commonly, the imaginary part of complex root is finite provided that the boundedness of the solution only depends on the real part of the eigenvalues. For more convenience in the construction of the homogeneous solution U^{fh} of equation (2.53), the real part of eigenvalues r_i are divided into three parts, a positive real part, a zero part, and a negative real part. Then, let \mathbf{R}^+ , \mathbf{R}^0 and \mathbf{R}^- be diagonal matrices containing the eigenvalue involving the positive real part, zero and negative real part respectively. Again, let three sets of Γ^{η^+} and Γ^{q^+} , Γ^{η^0} and Γ^{q^0} , Γ^{η^-} and Γ^{q^-} be matrices whose columns respectively contained all vectors of r_i and $\boldsymbol{\eta}_i$ generated from the eigenvalue associated with the positive real part \mathbf{R}^+ , the zero part \mathbf{R}^0 , and the negative real part \mathbf{R}^- respectively. Similarly, by introducing $\boldsymbol{\Pi}^+$, $\boldsymbol{\Pi}^0$ and $\boldsymbol{\Pi}^-$ as diagonal matrices obtained by substituting the diagonal entries r_i of the matrices \mathbf{R}^+ , \mathbf{R}^0 and \mathbf{R}^- respectively into the function $e^{r_i x_1}$, the corresponding homogeneous solution U^{fh} and the internal flux Q^{fh} can be express as

$$U^{fh}(x_1) = \Gamma^{\eta^+} \boldsymbol{\Pi}^+(x_1) \mathbf{C}^+ + \Gamma^{\eta^0} \boldsymbol{\Pi}^0(x_1) \mathbf{C}^0 + \Gamma^{\eta^-} \boldsymbol{\Pi}^-(x_1) \mathbf{C}^- \quad (3.11)$$

$$Q^{fh}(x_1) = \Gamma^{q^+} \boldsymbol{\Pi}^+(x_1) \mathbf{C}^+ + \Gamma^{q^0} \boldsymbol{\Pi}^0(x_1) \mathbf{C}^0 + \Gamma^{q^-} \boldsymbol{\Pi}^-(x_1) \mathbf{C}^- \quad (3.12)$$

where \mathbf{C}^+ , \mathbf{C}^0 and \mathbf{C}^- are the arbitrary constant vectors, which can be simply obtained by enforcing the boundary conditions.

3.2. Particular Solution

Let t^0 , the applied traction on the top surface, be a polynomial of degree m in terms of x_1 taking the form as

$$t^0 = \sum_{k=0}^m x_1^k a_k \quad (3.13)$$

where a_k denotes the given constant vector corresponding to the k^{th} degree of the polynomial. It should be noted that several functions including exponential, logarithm, trigonometric can be expressed in terms of a polynomial by adopting the Taylor series transform. Then, by employing the method of the undetermined coefficient, the particular solution of the system of equation (2.53), denoted by U^{fp} , can be expressed as

$$U^{fp} = \sum_{k=0}^m x_1^k A_k \quad (3.14)$$

The vector of unknown constants A_k has to be determined by taking the first, second derivation of U^{fp} and then directly substituting them into equation (2.53). Then, it gives rise to

$$(k+2)(k+1)E_2^{bsff} A_{k+2} + (k+1)[E_1^{bbff} - (E_1^{bbff})^T] A_{k+1} - E_0^{bbff} A_k = a_k \\ \forall k \in \{1, 2, \dots, m-2\} \quad (3.15)$$

$$\{m[E_1^{bbff} - (E_1^{bbff})^T] - E_0^{bbff}\} A_{m-1} = a_{m-1} \quad (3.16)$$

$$-E_0^{bbff} A_m = a_m \quad (3.17)$$

Now, by substituting U^{fp} into equation (2.55), the internal flux leads to

$$Q^{fp} = E_1^{bbff} U^{fp} + E_2^{bsff} U^{fp} \quad (3.18)$$

3.3. General Solution

The general solution of the displacement vector \mathbf{U}^f of the system of equations (2.53) and the corresponding nodal flux \mathbf{Q}^f can be obtained by directly combining the homogeneous and particular solutions and the final results are given by

$$\mathbf{U}^f = \mathbf{U}^{fh} + \mathbf{U}^{fp} = \Gamma^{\eta^+} \mathbf{\Pi}^+(x_1) \mathbf{C}^+ + \Gamma^{\eta^0} \mathbf{\Pi}^0(x_1) \mathbf{C}^0 + \Gamma^{\eta^-} \mathbf{\Pi}^-(x_1) \mathbf{C}^- + \mathbf{U}^{fp}(x_1) \quad (3.19)$$

$$\mathbf{Q}^f = \mathbf{Q}^{fh} + \mathbf{Q}^{fp} = \Gamma^{q^+} \mathbf{\Pi}^+(x_1) \mathbf{C}^+ + \Gamma^{q^0} \mathbf{\Pi}^0(x_1) \mathbf{C}^0 + \Gamma^{q^-} \mathbf{\Pi}^-(x_1) \mathbf{C}^- + \mathbf{Q}^{fp}(x_1) \quad (3.20)$$

In case that the left and the right boundaries are subjected to applied traction, the boundary fluxes are

$$\mathbf{Q}^f(x_{1l}) = -\mathbf{P}^{fl} \quad (3.21)$$

$$\mathbf{Q}^f(x_{1r}) = \mathbf{P}^{fr} \quad (3.22)$$

where \mathbf{P}^{fl} and \mathbf{P}^{fr} are $2n-2$ components nodal applied traction subset vectors of \mathbf{P}^l and \mathbf{P}^r . Due to the boundary conditions indicated in (3.21) and (3.22), equation (3.20) yields

$$\begin{Bmatrix} -\mathbf{P}^{fl} \\ \mathbf{P}^{fr} \end{Bmatrix} = \begin{bmatrix} \Gamma^{q^+} \mathbf{\Pi}^+(x_{1l}) & \Gamma^{q^0} \mathbf{\Pi}^0(x_{1l}) & \Gamma^{q^-} \mathbf{\Pi}^-(x_{1l}) \\ \Gamma^{q^+} \mathbf{\Pi}^+(x_{1r}) & \Gamma^{q^0} \mathbf{\Pi}^0(x_{1r}) & \Gamma^{q^-} \mathbf{\Pi}^-(x_{1r}) \end{bmatrix} \begin{Bmatrix} \mathbf{C}^+ \\ \mathbf{C}^0 \\ \mathbf{C}^- \end{Bmatrix} + \begin{Bmatrix} \mathbf{Q}^{fp}(x_{1l}) \\ \mathbf{Q}^{fp}(x_{1r}) \end{Bmatrix} \quad (3.23)$$

Equation (3.23) can be inverted to obtain

$$\begin{Bmatrix} \mathbf{C}^+ \\ \mathbf{C}^0 \\ \mathbf{C}^- \end{Bmatrix} = \begin{bmatrix} \Gamma^{q^+} \mathbf{\Pi}^+(x_{1l}) & \Gamma^{q^0} \mathbf{\Pi}^0(x_{1l}) & \Gamma^{q^-} \mathbf{\Pi}^-(x_{1l}) \\ \Gamma^{q^+} \mathbf{\Pi}^+(x_{1r}) & \Gamma^{q^0} \mathbf{\Pi}^0(x_{1r}) & \Gamma^{q^-} \mathbf{\Pi}^-(x_{1r}) \end{bmatrix}^{-1} \begin{bmatrix} -\mathbf{P}^{fl} \\ \mathbf{P}^{fr} \end{Bmatrix} - \begin{Bmatrix} \mathbf{Q}^{fp}(x_{1r}) \\ \mathbf{Q}^{fp}(x_{1l}) \end{Bmatrix} \quad (3.24)$$

If both the left and the right boundaries of the body are restrained against the movement such that the $2n-2$ components nodal displacements vectors $\mathbf{U}^{fl} = \mathbf{U}^f(x_{1l})$ and $\mathbf{U}^{fr} = \mathbf{U}^f(x_{1r})$ are known a priori, equation (3.19) becomes

$$\begin{Bmatrix} \mathbf{U}^{fl} \\ \mathbf{U}^{fr} \end{Bmatrix} = \begin{bmatrix} \Gamma^{\eta^+} \mathbf{\Pi}^+(x_{1l}) & \Gamma^{\eta^0} \mathbf{\Pi}^0(x_{1l}) & \Gamma^{\eta^-} \mathbf{\Pi}^-(x_{1l}) \\ \Gamma^{\eta^+} \mathbf{\Pi}^+(x_{1r}) & \Gamma^{\eta^0} \mathbf{\Pi}^0(x_{1l}) & \Gamma^{\eta^-} \mathbf{\Pi}^-(x_{1r}) \end{bmatrix} \begin{Bmatrix} \mathbf{C}^+ \\ \mathbf{C}^0 \\ \mathbf{C}^- \end{Bmatrix} + \begin{Bmatrix} \mathbf{U}^{fp}(x_{1l}) \\ \mathbf{U}^{fp}(x_{1r}) \end{Bmatrix} \quad (3.25)$$

For this particular case, equation (3.25) can be inverted to obtain

$$\begin{Bmatrix} \mathbf{C}^+ \\ \mathbf{C}^0 \\ \mathbf{C}^- \end{Bmatrix} = \begin{bmatrix} \Gamma^{\eta^+} \mathbf{\Pi}^+(x_{1l}) & \Gamma^{\eta^0} \mathbf{\Pi}^0(x_{1l}) & \Gamma^{\eta^-} \mathbf{\Pi}^-(x_{1l}) \\ \Gamma^{\eta^+} \mathbf{\Pi}^+(x_{1r}) & \Gamma^{\eta^0} \mathbf{\Pi}^0(x_{1l}) & \Gamma^{\eta^-} \mathbf{\Pi}^-(x_{1r}) \end{bmatrix}^{-1} \begin{bmatrix} \mathbf{U}^{fl} \\ \mathbf{U}^{fr} \end{Bmatrix} - \begin{Bmatrix} \mathbf{U}^{fp}(x_{1l}) \\ \mathbf{U}^{fp}(x_{1r}) \end{Bmatrix} \quad (3.26)$$

By using the result (3.24) or (3.26), it can be readily shown that

$$\begin{Bmatrix} -\mathbf{P}^{fl} \\ \mathbf{P}^{fr} \end{Bmatrix} - \begin{Bmatrix} \mathbf{Q}^{fp}(x_{1r}) \\ \mathbf{Q}^{fp}(x_{1l}) \end{Bmatrix} = \mathbf{K} \begin{bmatrix} \mathbf{U}^f(x_{1l}) \\ \mathbf{U}^f(x_{1r}) \end{bmatrix} - \begin{Bmatrix} \mathbf{U}^{fp}(x_{1l}) \\ \mathbf{U}^{fp}(x_{1r}) \end{Bmatrix} \quad (3.27)$$

where the coefficient matrix \mathbf{K} is defined by

$$\mathbf{K} = \begin{bmatrix} \Gamma^{\eta^+} \mathbf{\Pi}^+(x_{1l}) & \Gamma^{\eta^0} \mathbf{\Pi}^0(x_{1l}) & \Gamma^{\eta^-} \mathbf{\Pi}^-(x_{1l}) \\ \Gamma^{\eta^+} \mathbf{\Pi}^+(x_{1r}) & \Gamma^{\eta^0} \mathbf{\Pi}^0(x_{1l}) & \Gamma^{\eta^-} \mathbf{\Pi}^-(x_{1r}) \end{bmatrix} \begin{bmatrix} \Gamma^{\eta^+} \mathbf{\Pi}^+(x_{1l}) & \Gamma^{\eta^0} \mathbf{\Pi}^0(x_{1l}) & \Gamma^{\eta^-} \mathbf{\Pi}^-(x_{1l}) \\ \Gamma^{\eta^+} \mathbf{\Pi}^+(x_{1r}) & \Gamma^{\eta^0} \mathbf{\Pi}^0(x_{1l}) & \Gamma^{\eta^-} \mathbf{\Pi}^-(x_{1r}) \end{bmatrix}^{-1} \quad (3.28)$$

Equation (3.27) together with a set of prescribed boundary conditions provides a sufficient set of conditions to determine all unknown data on the boundaries of the representative layered medium. In particular, either the unknown nodal displacements or the unknown nodal tractions can be determined if either the nodal tractions or the nodal displacements are prescribed respectively.

3.4. Solution of entire layered medium

A system of linear equations governing the representative layered medium given by (3.27) is directly applied, here, to form the governing equation for the three sub-domains resulting from the cut of the whole layered medium along the lines bb' and cc' (i.e., the left part, the center part and the right part of the whole layered medium).

Since the center part has the same shape as the representative layered medium, the system of linear equations governing the unknown data on its boundary can be readily obtained in an identical form, i.e.,

$$\begin{Bmatrix} -\mathbf{P}_{II}^{fl} \\ \mathbf{P}_{II}^{fr} \end{Bmatrix} - \begin{Bmatrix} \mathbf{Q}_{II}^{fp}(x_{1r}) \\ \mathbf{Q}_{II}^{fp}(x_{1l}) \end{Bmatrix} = \mathbf{K}_{II} \begin{Bmatrix} \mathbf{U}_{II}^f(x_{1l}) \\ \mathbf{U}_{II}^f(x_{1r}) \end{Bmatrix} - \begin{Bmatrix} \mathbf{U}_{II}^{fp}(x_{1l}) \\ \mathbf{U}_{II}^{fp}(x_{1r}) \end{Bmatrix} \quad (3.29)$$

The system of linear equations governing the unknown data along the boundary of the left part and the right part of the whole layered medium can also be obtained from that of the representative layered medium by first setting applied loads at the top surface to zero and then taking limit of the left boundary or right boundary to infinity (i.e., $x_{1l} \rightarrow -\infty$ or $x_{1r} \rightarrow \infty$), respectively. The final systems of governing equations for the right and left parts are expressed explicitly as

$$\mathbf{K}_I \mathbf{U}_I^{fr} = \mathbf{P}_I^{fr} \quad (3.30)$$

$$\mathbf{K}_{III} \mathbf{U}_{III}^{fl} = -\mathbf{P}_{III}^{fl} \quad (3.31)$$

By enforcing the continuity of the displacement and the traction along the interface between the left part and the center part (i.e., along the line bb' indicated in Figure 1) and the interface between the right part and the center part (i.e., along the line cc' indicated in Figure 1) together with the standard assembly procedure of the three systems (3.29)-(3.31), it yields a final system of linear algebraic equations governing the nodal displacement data along the two interfaces bb' and cc' of the whole layered medium:

$$-\begin{Bmatrix} \mathbf{Q}_{II}^{fp}(x_{1r}) \\ \mathbf{Q}_{II}^{fp}(x_{1l}) \end{Bmatrix} = \mathbf{K} \begin{Bmatrix} \mathbf{U}^{fb} \\ \mathbf{U}^{fc} \end{Bmatrix} - \mathbf{K}_{II} \begin{Bmatrix} \mathbf{U}_{II}^{fp}(x_{1l}) \\ \mathbf{U}_{II}^{fp}(x_{1r}) \end{Bmatrix} \quad (3.32)$$

where \mathbf{K} denotes the material constant matrix resulted from the assembly of \mathbf{K}_I , \mathbf{K}_{II} , and \mathbf{K}_{III} associated with the right, center and left parts, respectively, and \mathbf{U}^{fb} and \mathbf{U}^{fc} are the unknown nodal displacements along the cuts bb' and cc' , respectively. Once the primary unknowns \mathbf{U}^{fb} and \mathbf{U}^{fc} are solved from (3.32), the elastic field including

the displacements and stresses within the whole layered medium can be readily post-processed with the use of basic field equations (2.1)-(2.3) together with the approximations (2.12).

3.5. Error

The error of the approximation using scaled boundary finite element method is measured by using the following formula:

$$error = \frac{\|\mathbf{e}\|_{L^2}}{\|\mathbf{u}^e\|_{L^2}} \times 100 \quad (3.32)$$

where $\|\mathbf{e}\|_{L^2}$ and $\|\mathbf{u}^e\|_{L^2}$ respectively denote the L^2 -norm of the error vector-value function and L^2 -norm of the exact value of the displacement and respectively defined by

$$\|\mathbf{e}\|_{L^2} = \sqrt{\int_{\Omega} \mathbf{e}^T(x) \mathbf{e}(x)} \quad (3.33)$$

$$\|\mathbf{u}^e\|_{L^2} = \sqrt{\int_{\Omega} (\mathbf{u}^e(x))^T \mathbf{u}^e(x)} \quad (3.34)$$

It is important to note that the error vector-value function $\mathbf{e} = \mathbf{e}(x)$ is determined by

$$\mathbf{e}(x) = \mathbf{u}^e(x) - \mathbf{u}^h(x) \quad (3.35)$$

where $\mathbf{u}^h(x)$ represent the approximated value of displacement determined by scale boundary finite element method.

3.6. Rate of convergence

In the approximation, the rate of convergence between two orders of a particular type of element is defined by

$$\frac{error_k}{error_{k+1}} = \left(\frac{h_k}{h_{k+1}} \right)^p \quad (3.36)$$

where $error_k$, h_k , and p respectively denoted relative percent error of k^{th} element, the element size of k^{th} element, and the rate of convergence between k^{th} and $(k+1)^{th}$ element.

CHAPTER 4

NUMERICAL RESULTS

In this chapter, the accuracy, convergence and capability of the proposed scaled boundary finite element method (SBFEM) in determining mechanical response of layered media under surface excitations are extensively discussed. The SBFEM has been successfully implemented within the MATLAB environment. In the solution discretization, both conventional linear and quadratic C^0 elements, similar to those employed in the finite element procedure for one-dimensional problems, are adopted. Several problems related to surface-loaded layer media including an elastic (functionally graded) half-plane, a single layer medium, and a multi-layer medium are considered in the numerical study. Results for certain cases (e.g., surface-loaded elastic layer and functionally graded half-plane with and without surface stresses) are compared with available benchmark solutions to confirm the correctness of both the formulation and numerical implementations. In addition, a series of meshes is adopted and used in the analysis to provide sufficient evidence to conclude the convergence behavior of numerical solutions.

4.1. Surface-loaded Half-plane

Consider an elastic half-plane loaded by a constant pressure p over the length $2a$ as shown schematically in Figure 3. This specific problem is chosen first in the numerical study since solutions for various cases including homogeneous and functionally graded half-planes were reported in the literature and can be used to verify the proposed technique.

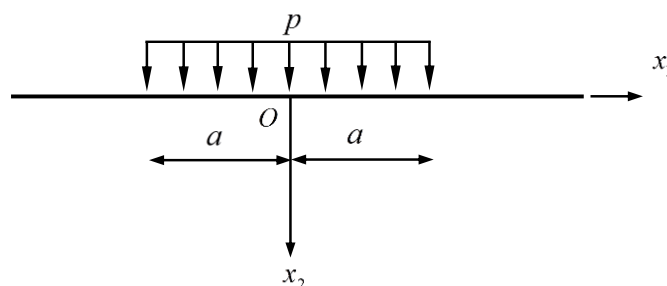


Figure 3: Elastic half-plane loaded by constant pressure p over length $2a$

Within the present formulation (where the layer possesses the finite thickness), a half-plane can be readily simulated by a single layer medium rested on a rigid foundation with its finite thickness h being chosen sufficiently large in comparison with the size of the loading region $2a$ (i.e., $h/a \gg 1$).

4.2. Homogeneous half-plane without surface stresses

Consider, now, a half-plane that is made of a homogeneous, isotropic, linearly elastic material and free of the influence of surface stresses (i.e., $\tau^s = \lambda^s = \mu^s = 0$). For this particular case, the exact solution for the elastic field within the medium can be found in standard textbooks for solid mechanics.

The convergence of numerical solutions obtained via the uniform discretization is investigated first. As clearly illustrated by Figure 4 and Figure 5, the normalized vertical stresses along the line of symmetry generated from meshes containing either linear or quadratic elements converge to the reference solution. Due to the higher order of basis functions, solutions generated by quadratic elements converge faster than those by linear elements. However, for both cases (linear and quadratic elements), the convergence of solutions in a region close to the top surface is quite slow in comparison with the remote region. Thus, to improve the convergence as well as to further reduce the computational effort and computational time while dealing with a very large thickness h , the non-uniform discretization along the approximation direction is employed in order to obtain a sufficiently fine mesh near the loading region where the mechanical response is anticipated to be quite complicated and coarser mesh at the region far away from the free surface. To achieve such non-uniform discretization, the ratio between sizes of two consecutive elements, denoted by α is chosen constant for this particular problem. The size of the i^{th} element, denoted by h_i , can be related to the thickness of the layer h and the number of elements n used in the discretization by

$$h_i = h_1 \alpha^{i-1}, \quad h_1 = h \left(\frac{\alpha - 1}{\alpha^n - 1} \right), \quad i = 1, 2, \dots, n \quad (4.1)$$

where the first and last elements, h_1 and h_n , are adjacent to the free surface and the rigid foundation, respectively.

The vertical stresses along the line of symmetry generated from a series of non-uniform meshes with $\alpha = 1.3$ are reported, again, in Figure 6 and Figure 7 for linear and quadratic elements, respectively. As anticipated, the normalized vertical stresses obtained from the non-uniform discretization of either linear or quadratic elements converge significantly faster than that of the uniform case. Interestingly, within a few number of elements, the solution generated from the proposed technique is indistinguishably comparable to the reference solution.

To alternatively confirm the correctness of the method, the displacement and stress on the free surface and within the half-plane obtained from the proposed technique are reported in Figures 8-12 together with the reference solutions. Due to the fast convergence resulting from the use of the non-uniform discretization, results reported in Figures 8-12 below are obtained from a mesh containing only 64 quadratic elements with $\alpha = 1.3$. It is seen that converged numerical solutions exhibit excellent agreement with the exact solution; in particular, plots of the two solutions are nearly identical for both the displacement and stress profiles.

To further emphasize the computational efficiency of the proposed technique, the problem of a homogenous half-plane subjected to a uniformly distributed normal surface traction is resolved again by using available standard finite element techniques (e.g., ANSYS) and the numbers of elements required in both techniques to obtain the converged solutions are compared. In the finite element analysis, the half-plane is truncated into a finite domain of dimensions $h/a=25$ and $L/a = 50$ and 8-node rectangular elements are employed in the discretization. The vertical stresses along the line of symmetry obtained from a series of finite element meshes are reported in Figure 13 together with the reference solution and the solution generated by the proposed SBFEM with a mesh containing 64 uniform quadratic elements. As observed from these results, to obtain solutions of the same quality, the standard finite element method requires a significantly larger number of degrees of freedom in the approximation.

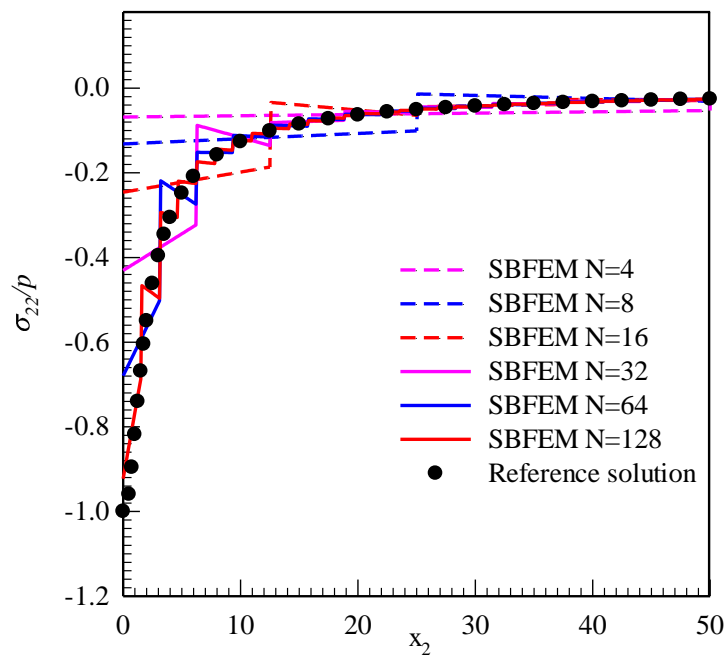


Figure 4: Normalized vertical stress along the line of symmetry obtained from uniform meshes containing linear elements

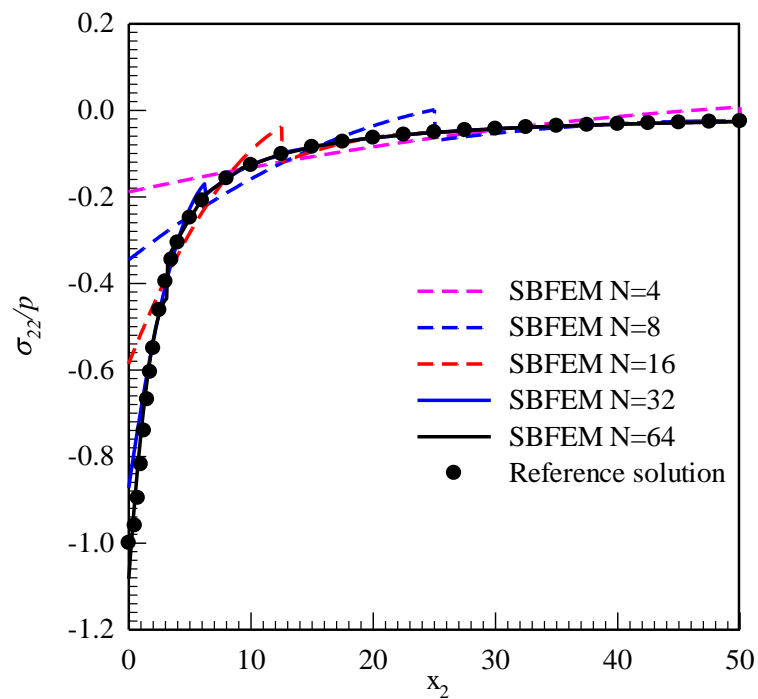


Figure 5: Normalized vertical stress along the line of symmetry obtained from uniform meshes containing quadratic elements

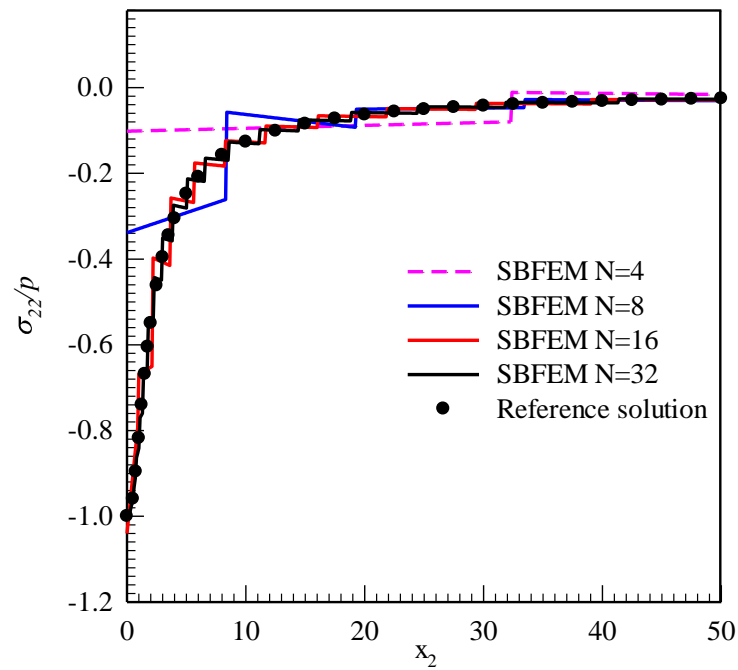


Figure 6: Normalized vertical stress along the line of symmetry obtained from non-uniform meshes containing linear elements

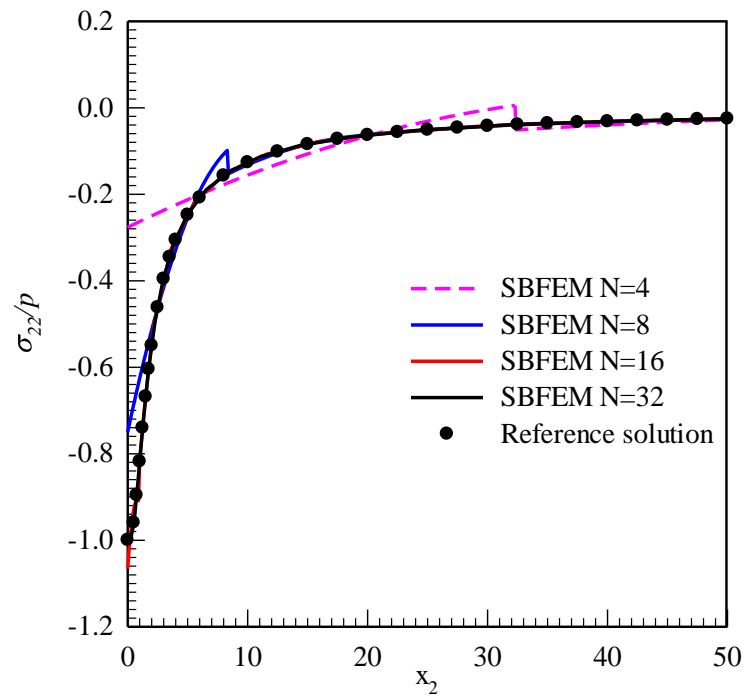


Figure 7: Normalized vertical stress along the line of symmetry obtained from non-uniform meshes containing quadratic elements

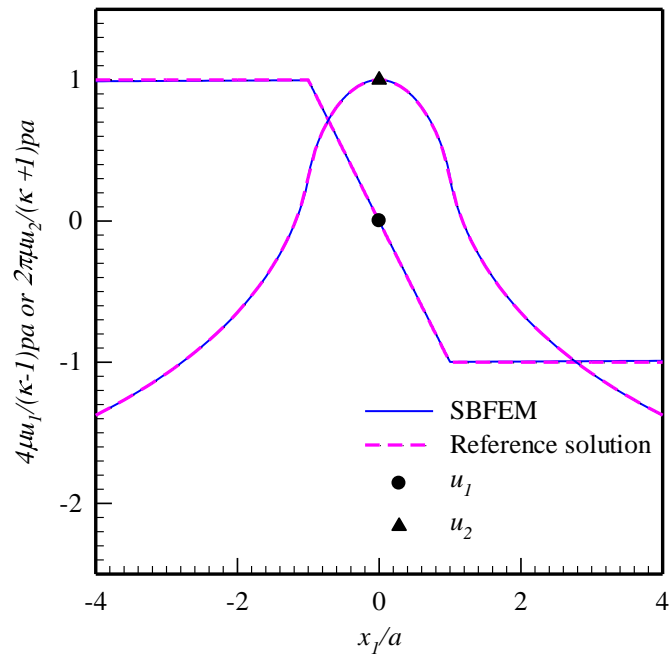


Figure 8: Normalized surface displacement of a homogeneous half-plane without influence of surface stresses.

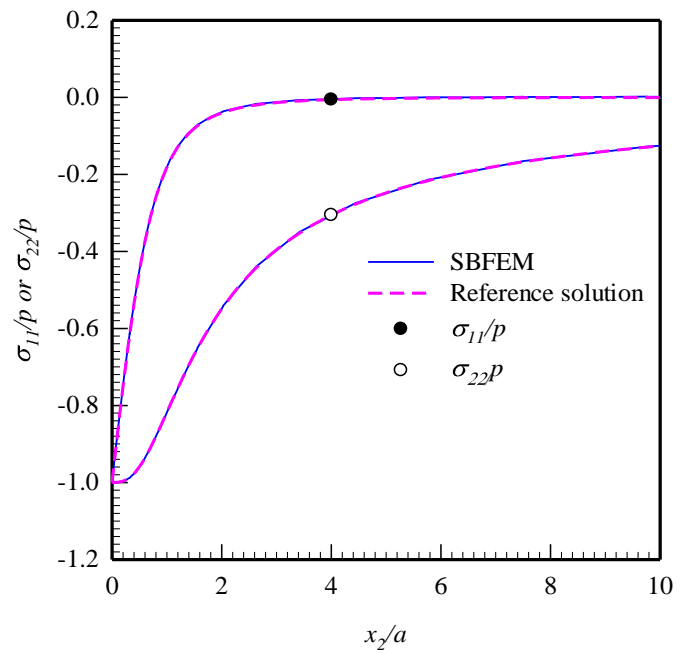


Figure 9: Normalized horizontal and vertical stress components of a homogeneous half-plane without influence of surface stresses. Results are reported along $x_1 = 0$.

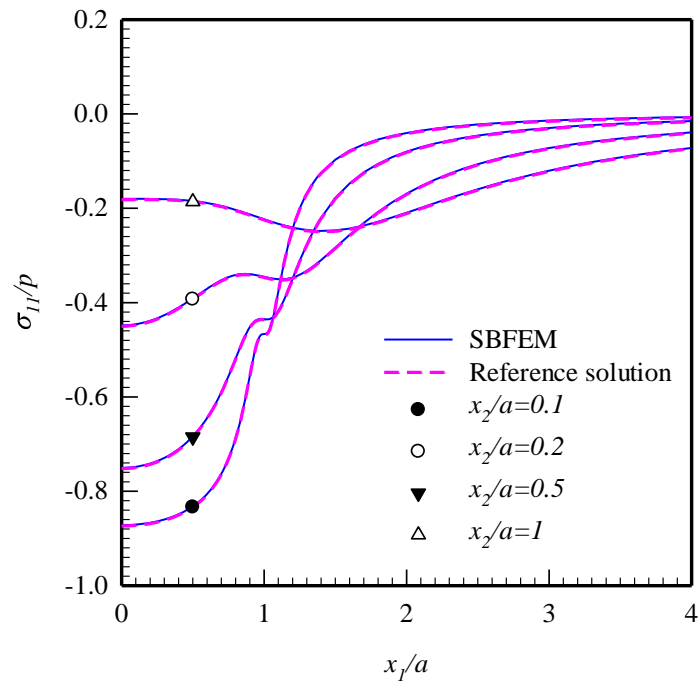


Figure 10: Normalized horizontal stress component of a homogeneous half-plane without influence of surface stresses. Results are reported at different depths.

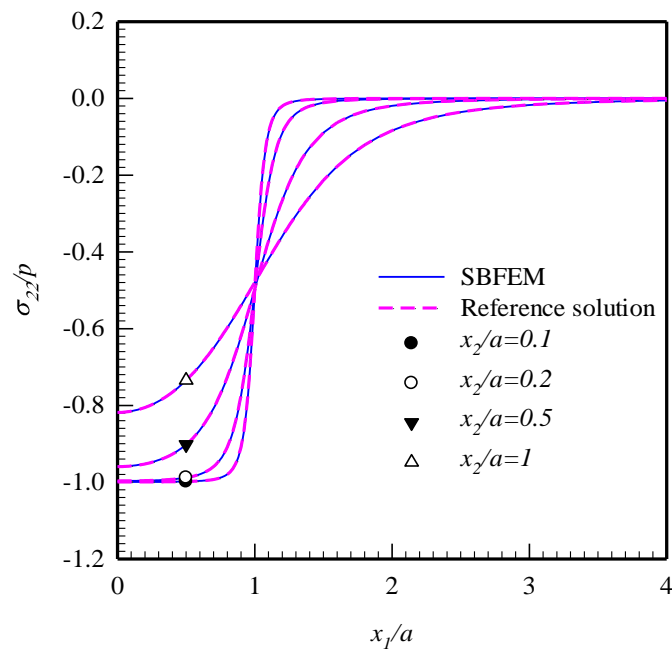


Figure 11: Normalized vertical stress component of a homogeneous half-plane without influence of surface stresses. Results are reported at different depths.

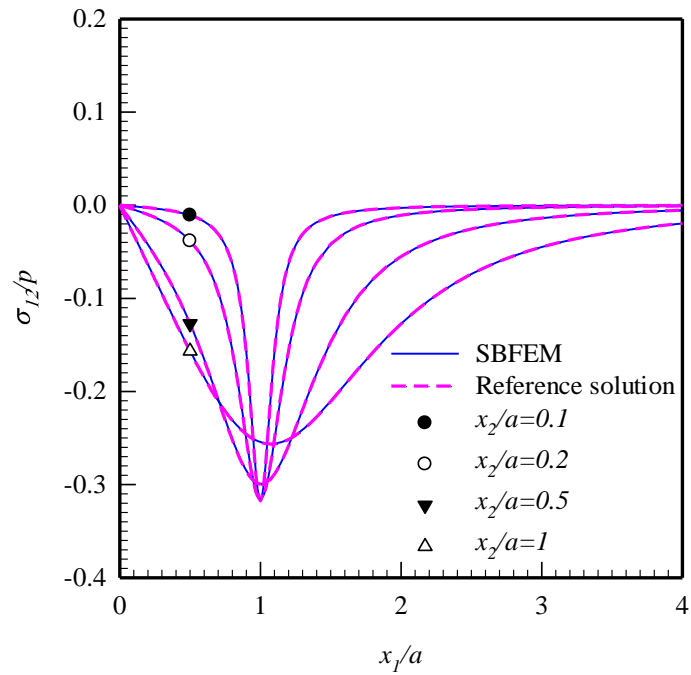


Figure 12: Normalized shear stress component of a homogeneous half-plane without influence of surface stresses. Results are reported at different depths.

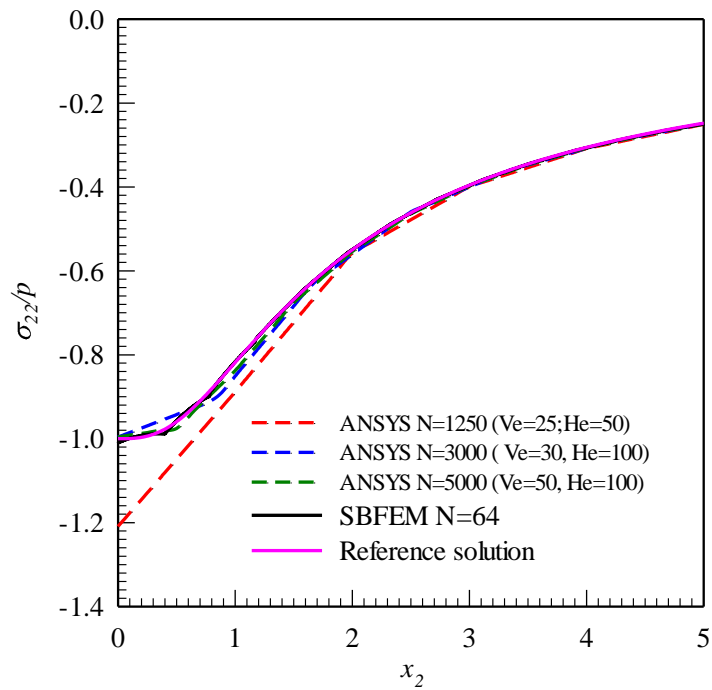


Figure 13: Normalized vertical stress generated from standard FEM, SBFEM and reference solution.

4.2.1. Functionally graded half-plane

Consider, next, an elastic half-plane that is made of an incompressible functionally graded (FG) and under the influence of surface stresses. To allow the comparison with reference solutions reported in the literature (Zhu et al. (2019)), only the residual surface tension τ^s is taken into account in Gurtin-Murdoch surface elasticity model whereas the surface Lamé constants are fully ignored. The material properties of the bulk FG material are taken from Gibson's solid (Gibson, 1967) where Poisson's ratio is taken as $\nu = 0.5$ (for an incompressible solid) and the elastic shear modulus $\mu = \mu(x_2)$ is taken as

$$\mu(x_2) = \mu_0 + mx_2 \quad (4.2)$$

where μ_0 and m denote the shear modulus at the top surface and the shear modulus gradient, respectively. Results of Zhu et al. (2019) were reported for different ratios s/β where $\beta = \mu_0/m$ denotes the ratio between the shear modulus of the top surface and the shear modulus gradient and $s = \tau^s/2\mu_0$ denotes the intrinsic length scale of the material surface. In addition, the ratio between the half length of the loading region a and the parameter β is fixed equal to 0.1 (i.e., $a/\beta = 0.1$). In the analysis, a non-uniform mesh containing the 64 quadratic elements with $\alpha = 1.3$ is employed to generate the converged numerical results.

To simulate the incompressibility of the bulk, the value of Poisson's ratio is taken very close to 0.5, i.e., $\nu = 0.4999$, and no numerical instability has been observed in the analysis. The normalized horizontal surface displacement, the normalized vertical surface displacement, and the surface vertical stress generated by the proposed technique are reported in Figures 14, 15, and 16, respectively, together with the benchmark solution from Zhu et al. (2019). Results are compared for classical case without the surface effect ($s/\beta = 0$), the case of inferior surface effect ($s/\beta = 0.02$), and the case of superior surface effect ($s/\beta = 0.1$). It is evident that the established results are in very good agreement with the reference solutions. Although the thickness of the layer used to simulate the half-plane is quite large, accurate results can be obtained with the use of few elements as long as the non-uniform mesh

is employed to obtain meshes with elements of sufficiently small size at the desired location.

For the classical case where the surface effect is fully neglected ($s/\beta = 0$), both the normalized horizontal and vertical surface displacement at the loading area of the half-plane is relatively higher than the other two cases ($s/\beta = 0.02$ and $s/\beta = 0.1$) as clearly illustrated in Figure 14 and Figure 15. This finding also confirms the conclusion of the various previous researches on that the presence of surface stresses or surface energy renders the material stiffer (Zhao and Rajapakse, 2009, Intarrit et al., 2010, Intarrit et al., 2011, Zhao and Rajapakse, 2013, Rungamornrat et al., 2016, Tirapat et al., 2017, Tarntira, 2018). Similarly, as the ratio s/β increases, the vertical stress at the free surface of the bulk reduces over the loading region and becomes larger outside of the loading region. In short, as supported by results shown in Figure 14 to Figure 16, the presence of the residual surface tension significantly alters both the distribution and value of the displacements and stresses at the top surface.

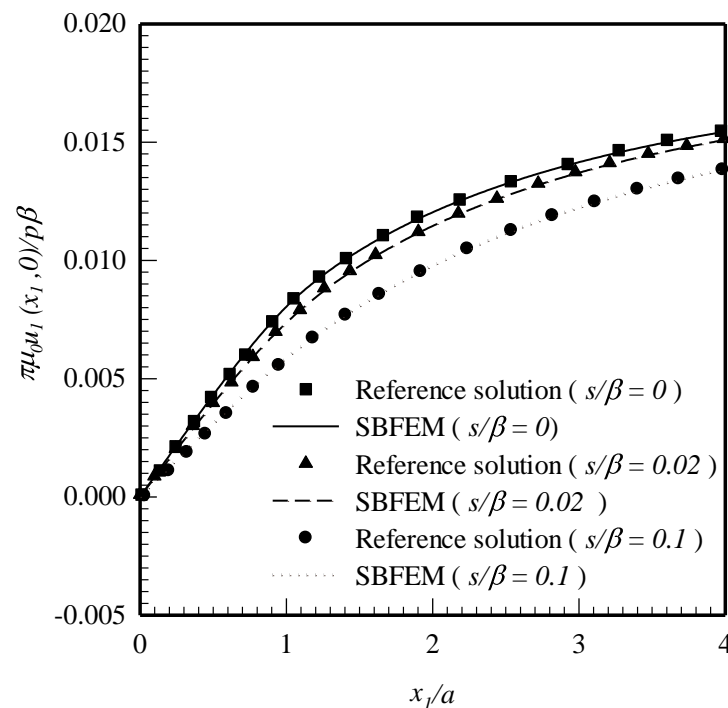


Figure 14: Normalized surface horizontal displacement of FG half-plane under uniformly distributed normal traction.

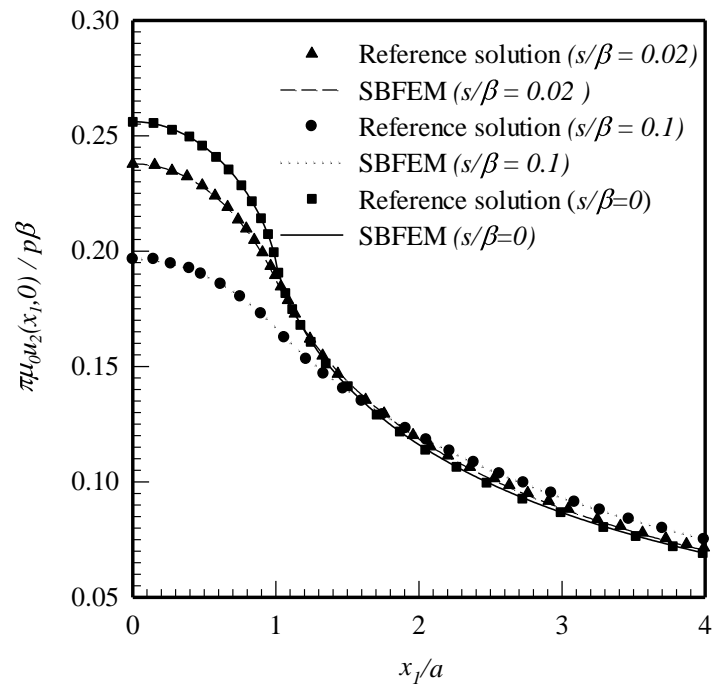


Figure 15: Normalized surface vertical displacement of FG half-plane under uniformly distributed normal traction.

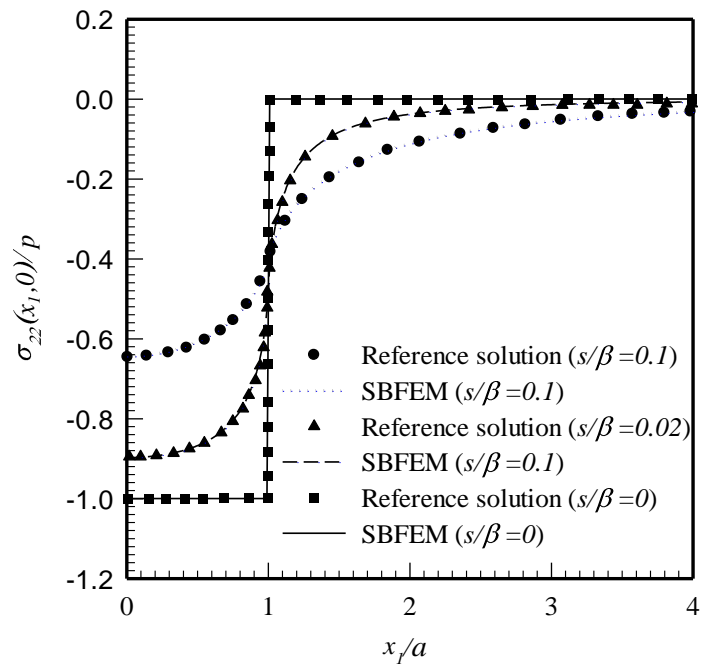


Figure 16: Normalized surface vertical stress of FG half-plane under uniformly distributed normal traction.

4.3. Single layer medium

Consider, next, a semi-infinite, rigid-based, elastic layer of the thickness $h = 2\Lambda$ subjected to two different types of surface loading over the length $2a$, Type-1 for uniformly distributed normal traction p and Type-2 for uniformly distributed shear traction q , as schematically shown in Figure 17. The intrinsic length scale of the surface material Λ is defined by

$$\Lambda = \frac{\kappa^s(2\mu + \lambda)}{2\mu(\mu + \lambda)} \quad (4.3)$$

where $\kappa^s = 2\mu^s + \lambda^s$. The layer, considered in the numerical study, is made of Al [111] whose material properties are shown in Table 5. In the analysis, uniform meshes containing either linear or quadratic elements are employed. The convergence of numerical solutions is investigated first and the converged solution is then compared with those obtained from a method of Fourier integral transform proposed by [Intarit et al. \(2011\)](#).

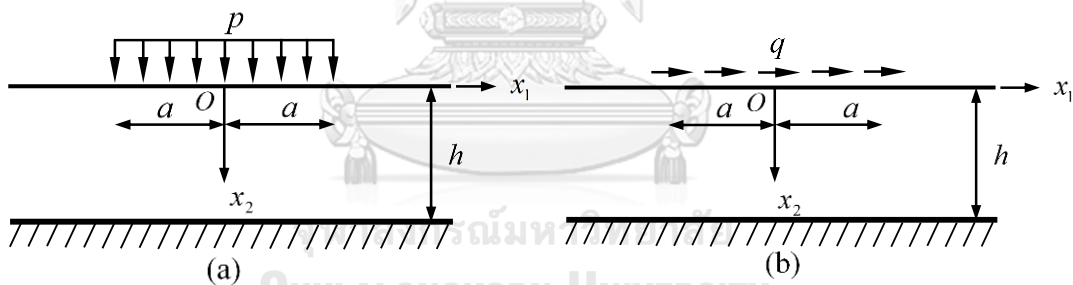


Figure 17: Semi-infinite rigid-based elastic layer under surface loading: (a) uniformly distributed normal traction and (b) uniformly distributed shear traction.

4.3.1. Uniformly distributed normal traction

The normalized vertical displacement and normalized vertical stress along the line of symmetry are reported in Figures 18-19 and Figures 20-21 for the uniform discretization with linear and quadratic elements, respectively. Results are compared with the analytical solutions reported by [Intarit et al. \(2011\)](#). It is seen that both the displacement and stress converge as the mesh is refined and the converged solutions are comparable to the reference solutions for all cases. As anticipated from the nature

of the approximation and requirement to evaluate derivatives when the stress is computed, the solution of the displacement converges much faster than that of the stress. In addition, the quality of the approximate solutions generated by quadratic elements is far superior to that from linear elements especially for the stress field. Only few elements can be used to obtain results comparable to the analytical solutions.

Extensive results of the displacement and stress at various locations within the medium, generated by a uniform mesh containing 128 quadratic elements, are also reported in Figures 22-26 and compared with analytical solutions from [Intarit et al. \(2011\)](#). It is evident from all plots that the two solutions are graphically identical and this excellent agreement additionally confirms the correctness of the proposed technique. Due to the high quality of this set of numerical results, they are taken as the converged solution and later used as the exact solution to evaluate the solution error. The contour plots of the normalized displacements and stresses are also reported in Figures 27-31 to clearly see the variation of the field quantities in regions surrounding the loading area with and without the influence of the surface stresses.

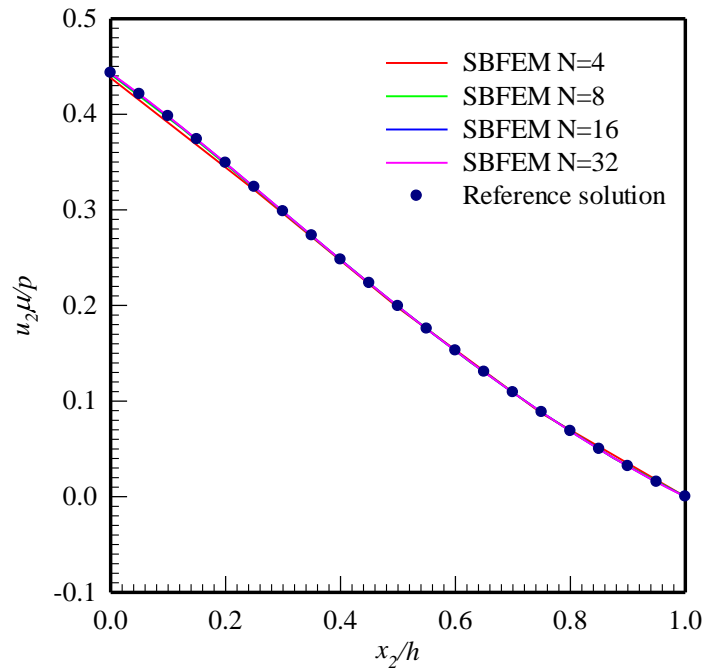


Figure 18: Normalized vertical displacement along the line of symmetry obtained from uniform meshes containing linear elements

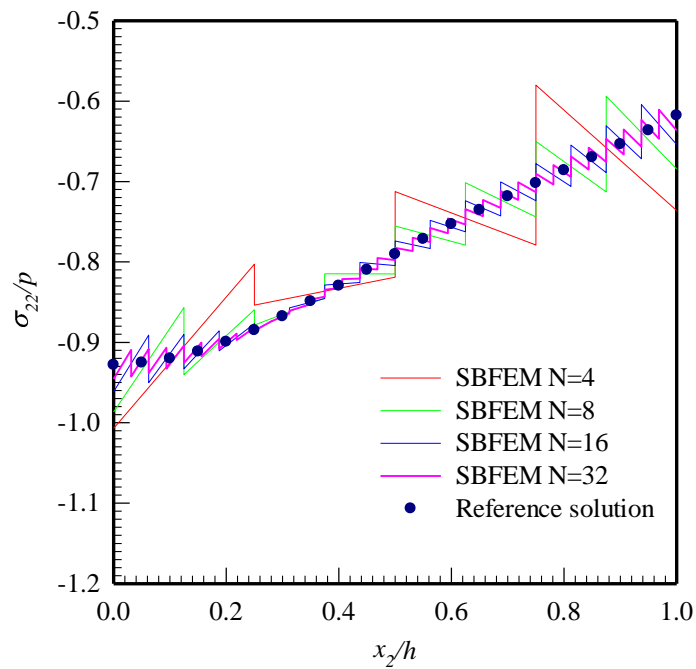


Figure 19: Normalized vertical stress along the line of symmetry obtained from uniform meshes containing linear elements

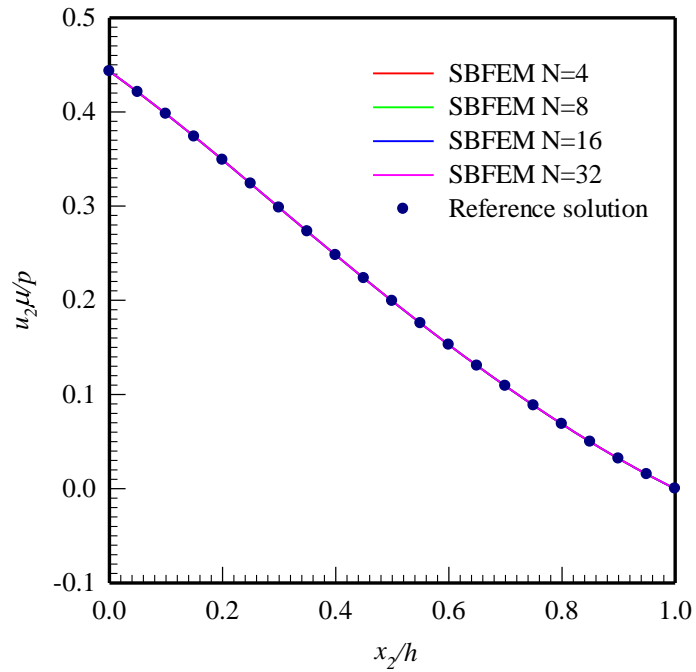


Figure 20: Normalized vertical displacement along the line of symmetry obtained from uniform meshes containing quadratic elements

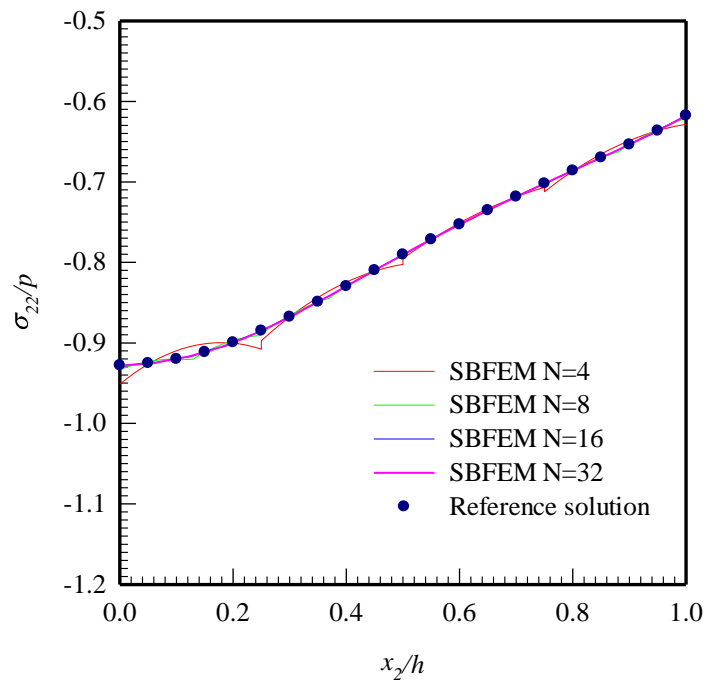


Figure 21: Normalized vertical stress along the line of symmetry obtained from uniform meshes containing quadratic elements

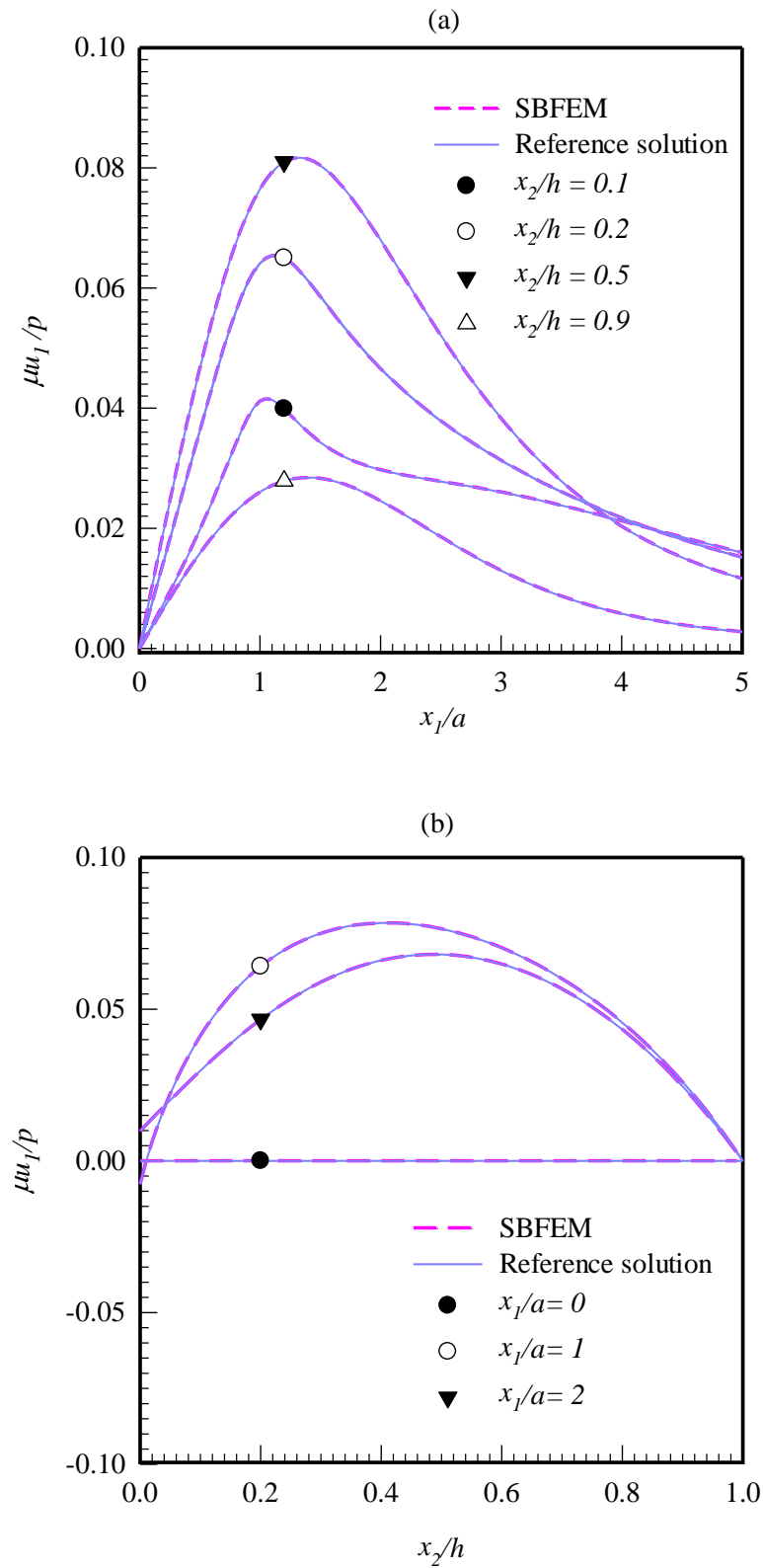


Figure 22: Normalized horizontal displacement along (a) x_1 -direction and (b) x_2 -direction generated by a uniform mesh containing 128 quadratic elements

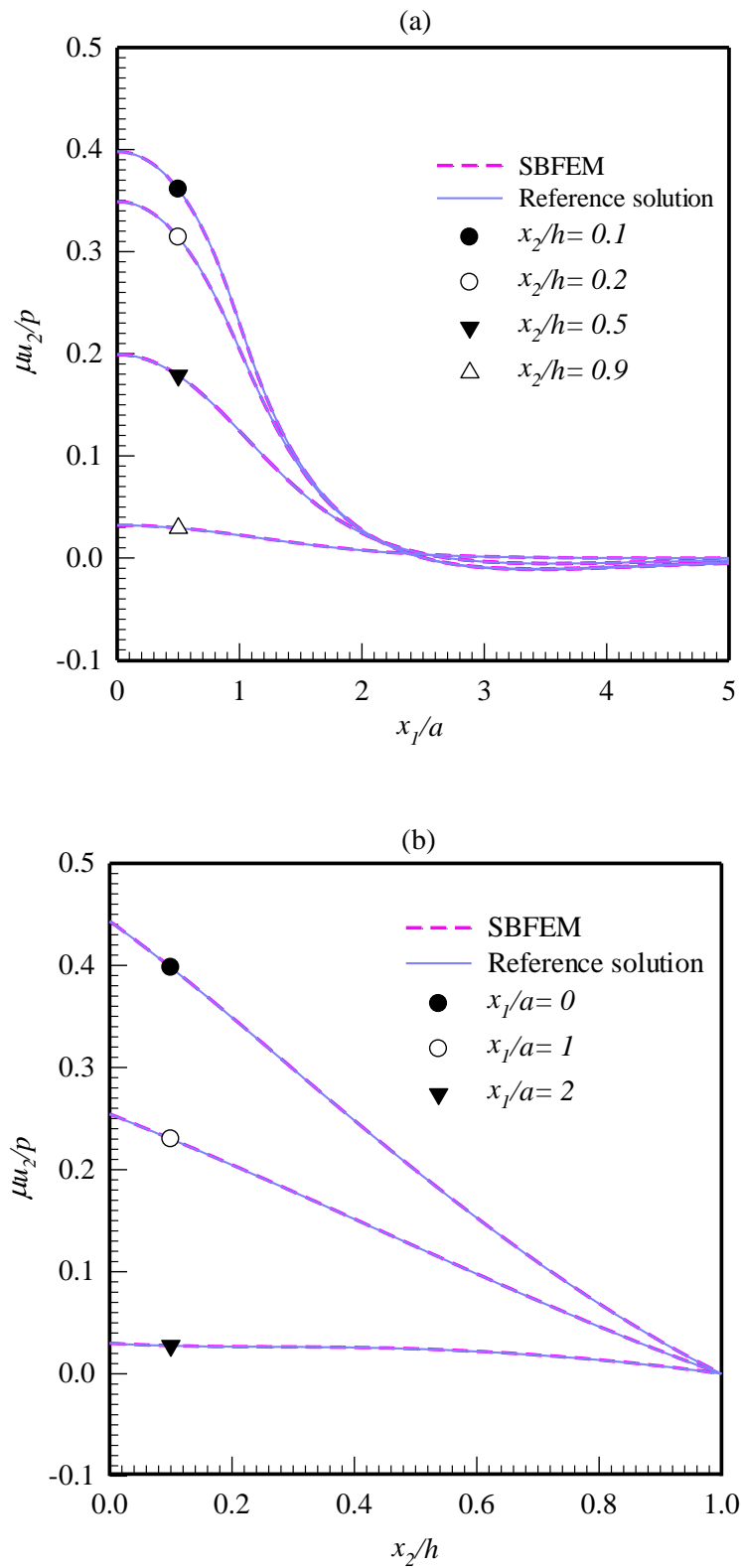


Figure 23: Normalized vertical displacement along (a) x_1 -direction and (b) x_2 -direction generated by a uniform mesh containing 128 quadratic elements

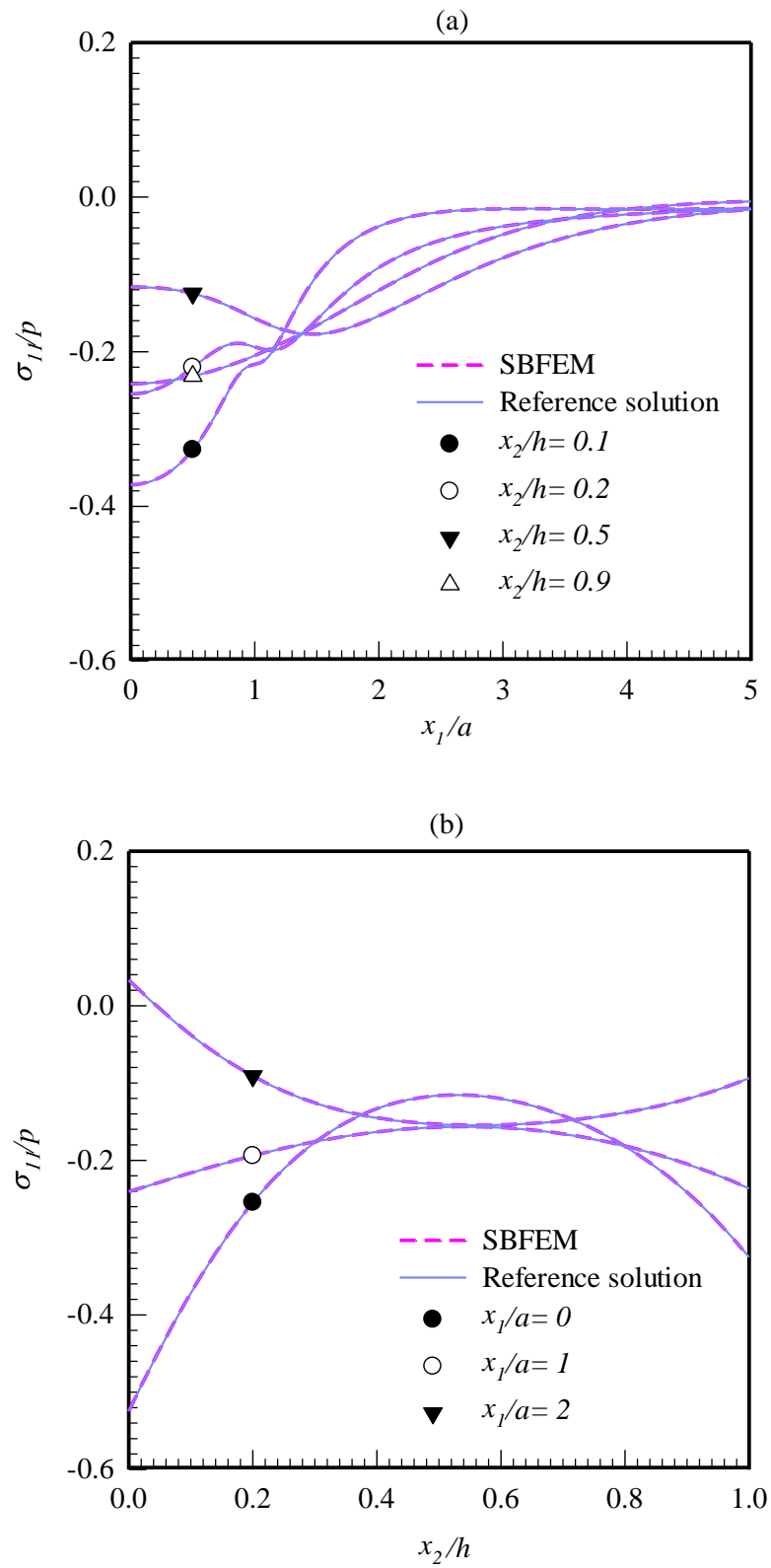


Figure 24: Normalized horizontal stress along (a) x_1 -direction and (b) x_2 -direction generated by a uniform mesh containing 128 quadratic elements

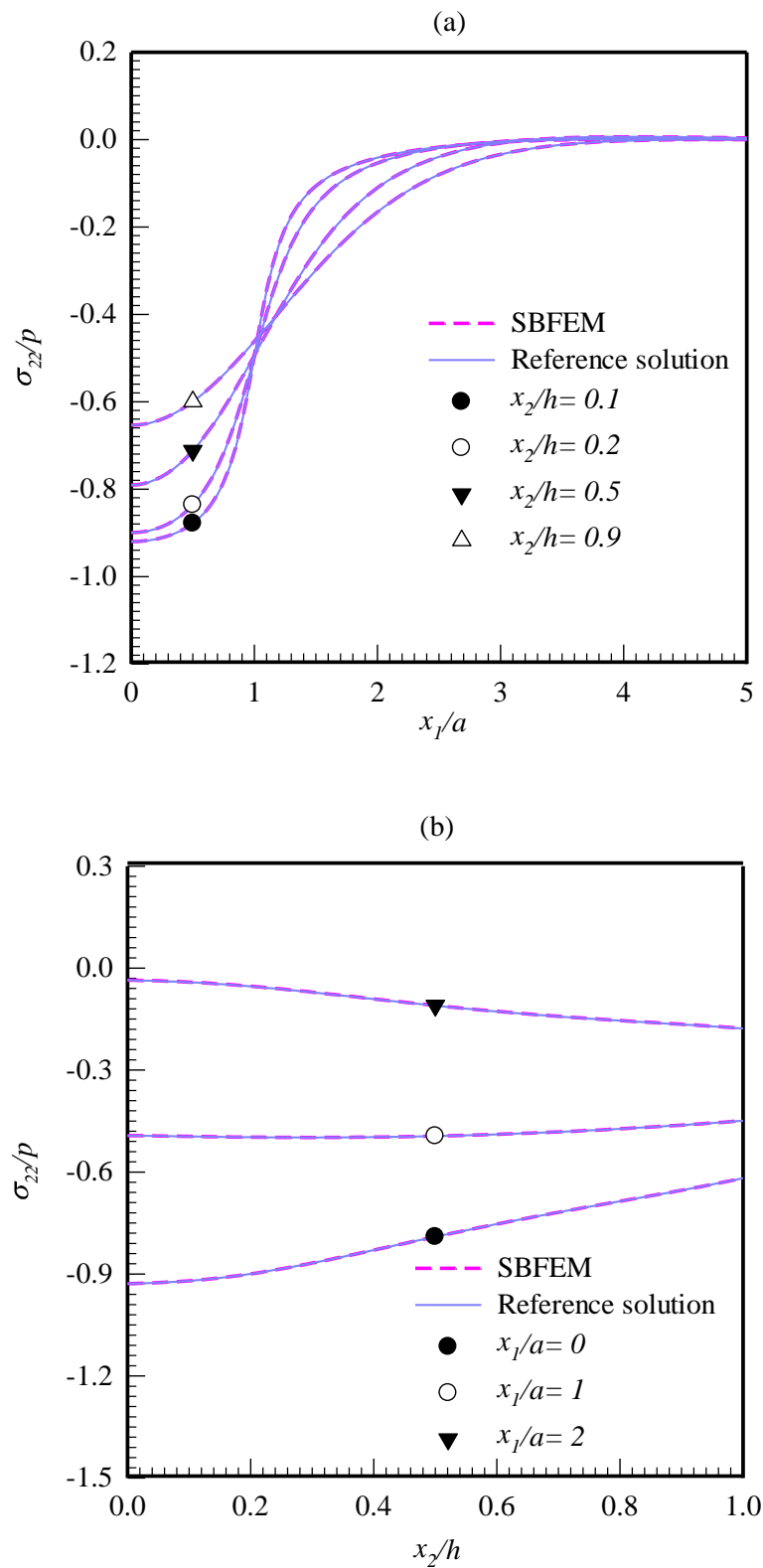


Figure 25: Normalized vertical stress along (a) x_1 -direction and (b) x_2 -direction generated by a uniform mesh containing 128 quadratic elements

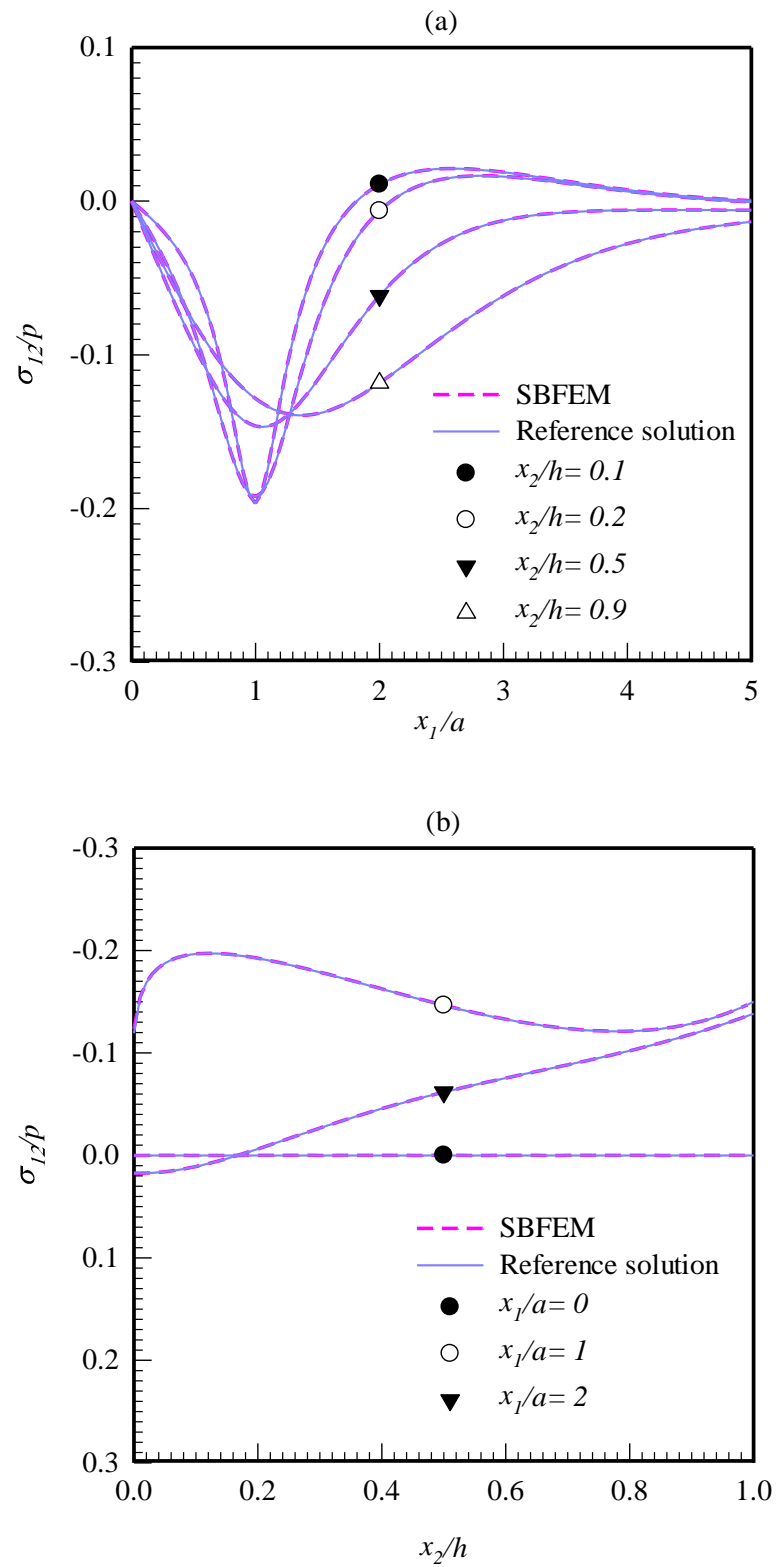


Figure 26: Normalized shear stress along (a) x_1 -direction and (b) x_2 -direction generated by a uniform mesh containing 128 quadratic elements

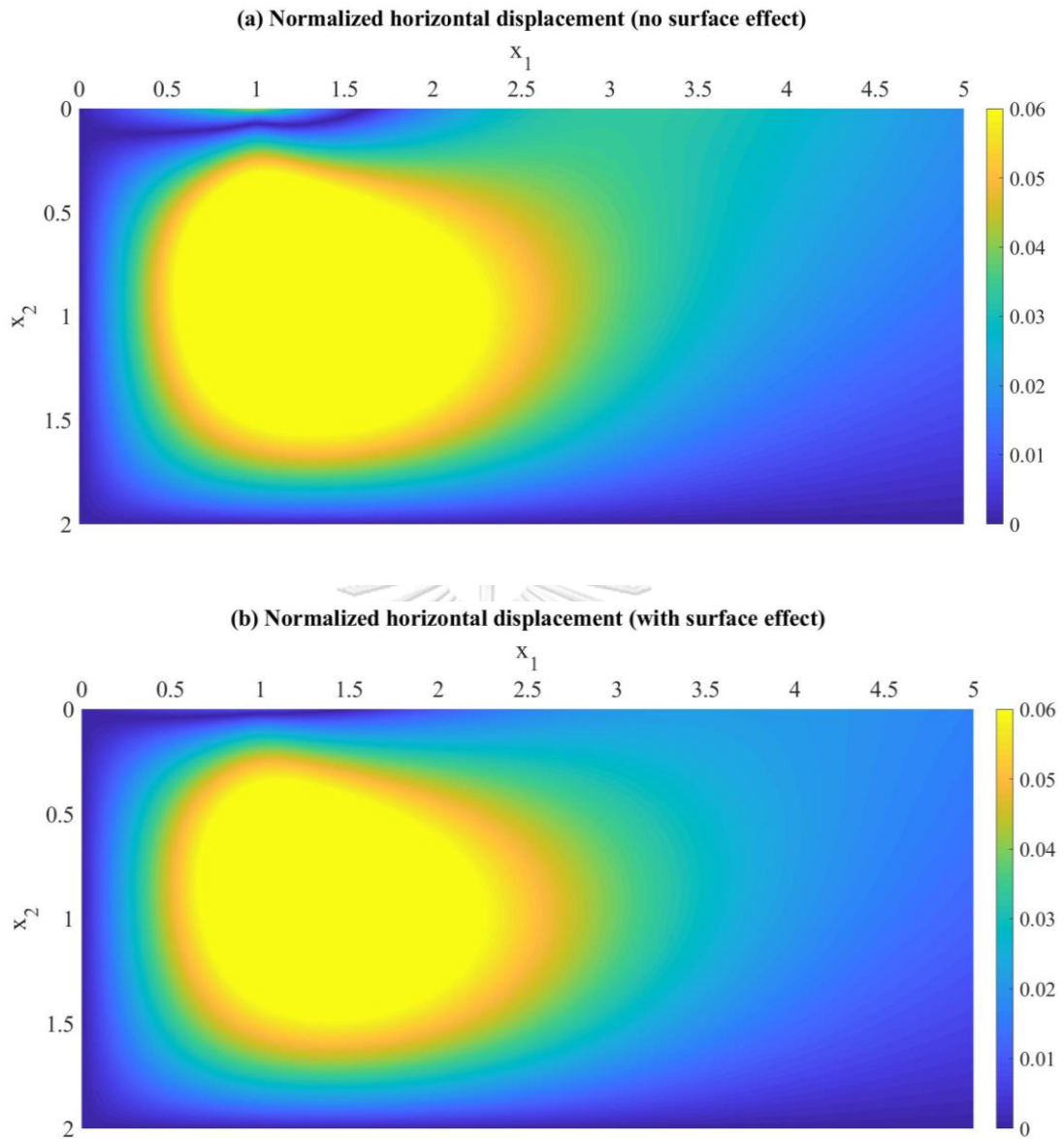


Figure 27: Contour plot of normalized horizontal displacement ($\mu u_1 / p$) of a rigid-based elastic layer under uniformly distributed normal traction: (a) without surface effect and (b) with surface effect

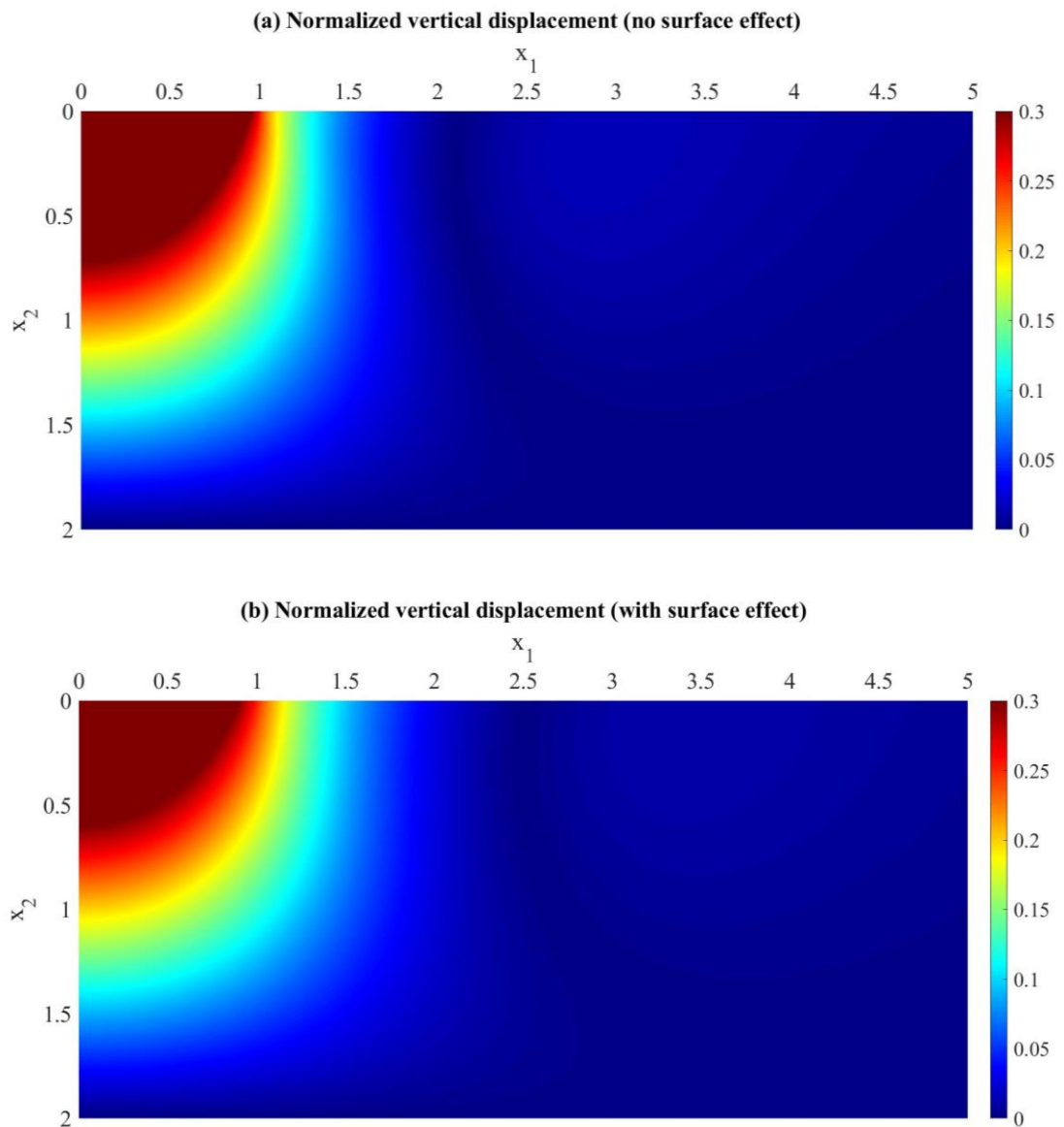


Figure 28: Contour plot of normalized vertical displacement ($\mu u_2 / p$) of a rigid-based elastic layer under uniformly distributed normal traction: (a) without surface effect and (b) with surface effect

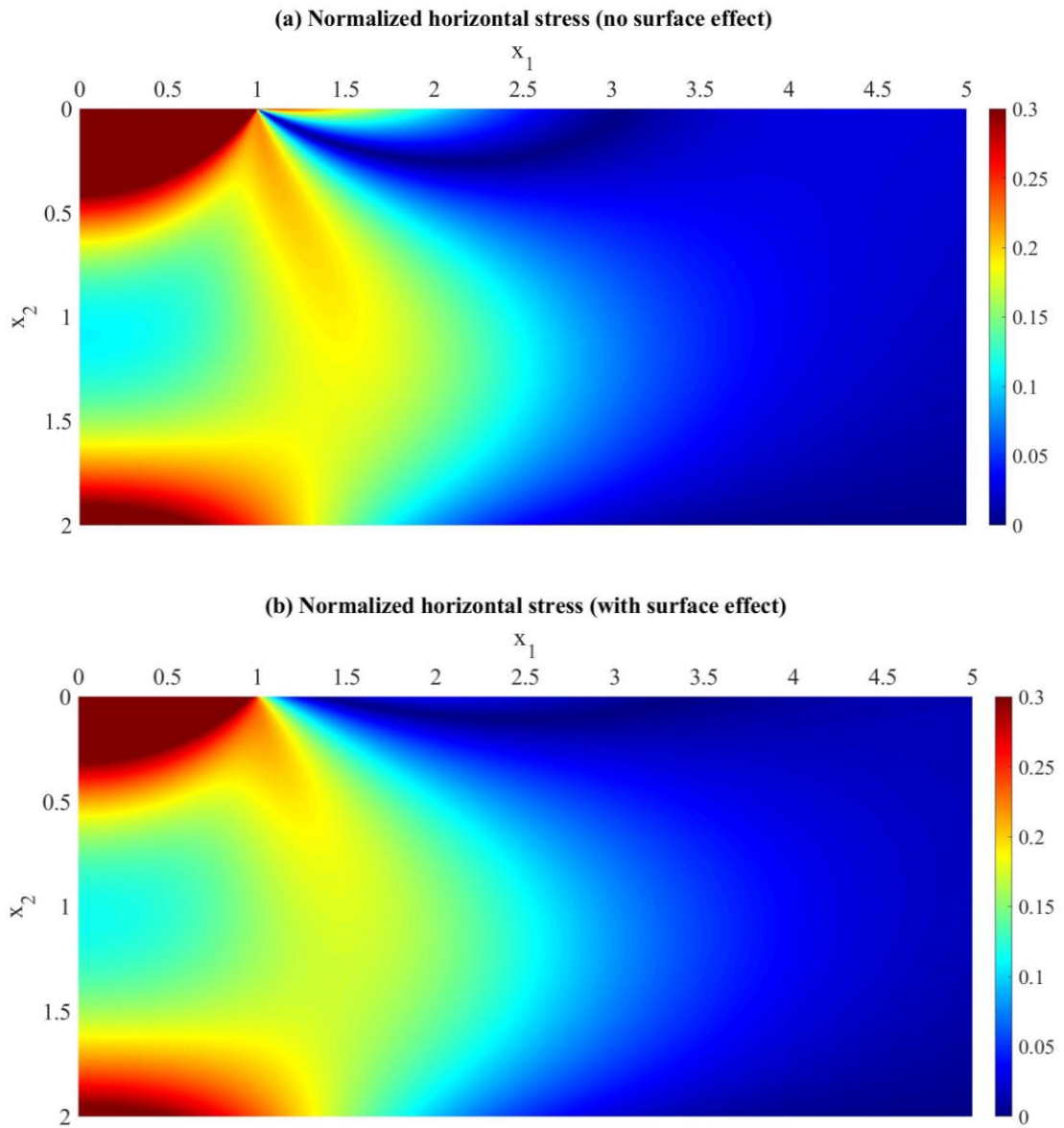


Figure 29: Contour plot of normalized horizontal stress ($-\sigma_{11} / p$) of a rigid-based elastic layer under uniformly distributed normal traction: (a) without surface effect and (b) with surface effect

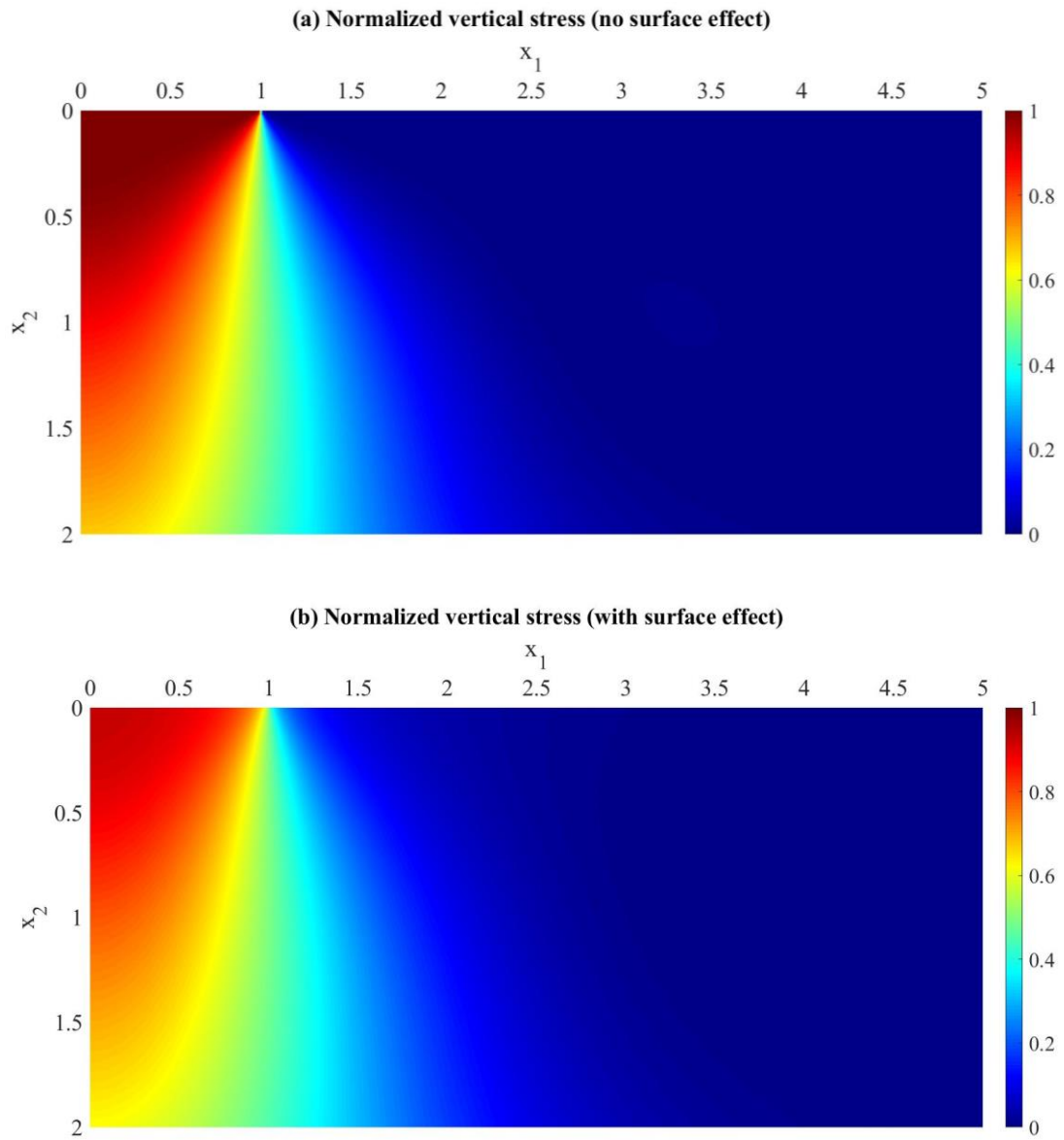


Figure 30: Contour plot of normalized vertical stress ($-\sigma_{22} / p$) of a rigid-based elastic layer under uniformly distributed normal traction: (a) without surface effect and (b) with surface effect

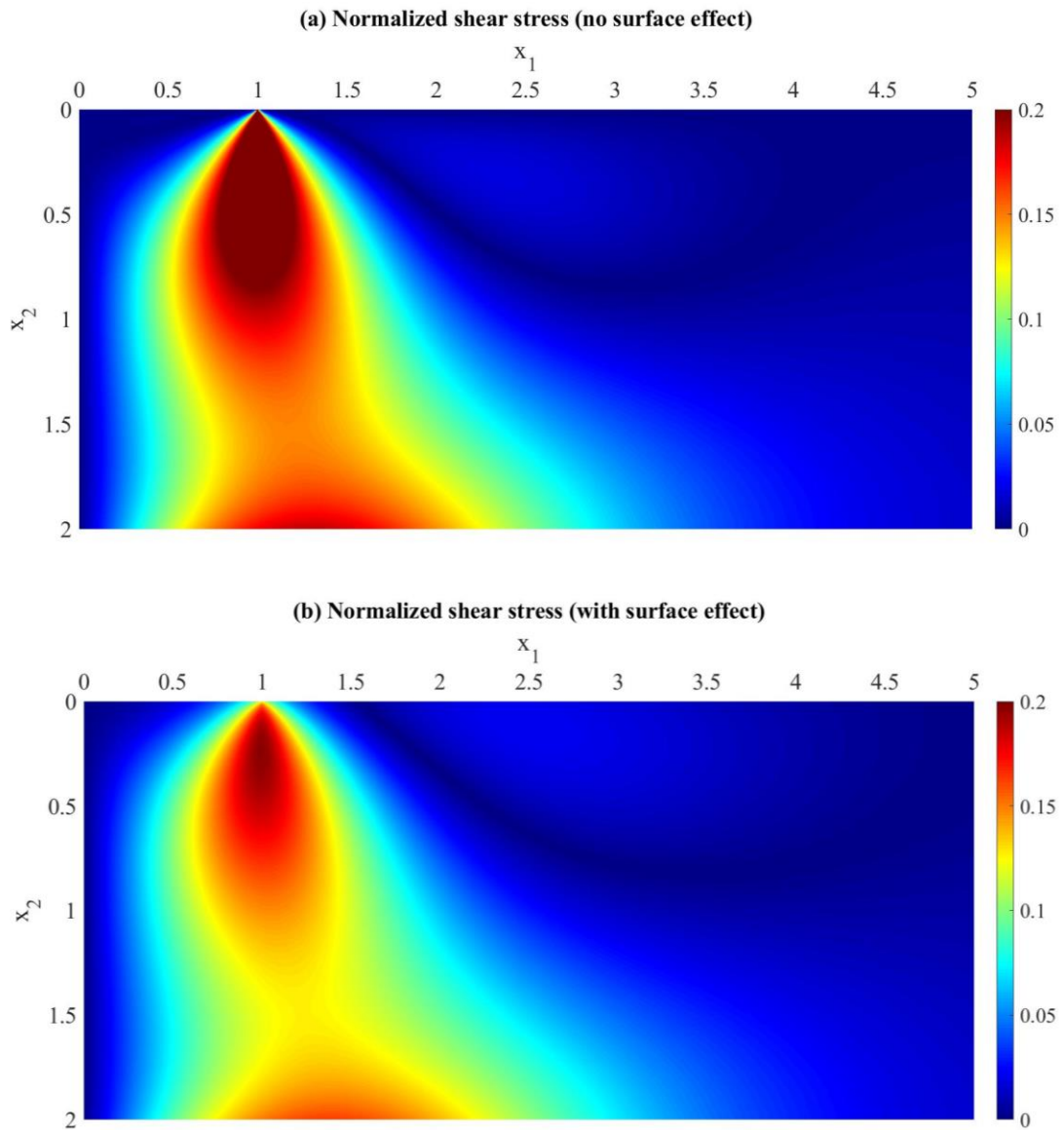


Figure 31: Contour plot of normalized shear stress ($-\sigma_{12} / p$) of a rigid-based elastic layer under uniformly distributed normal traction: (a) without surface effect and (b) with surface effect

To further explore the convergence behavior of SBFEM solutions, for this particular loading case, the relative errors and the rate of convergence are computed and reported in Table 1, Table 2, and Figure 32 for both linear and quadratic elements. Since the closed-form solution is not available in the literature, the solution generated by a sufficiently fine mesh containing 128 quadratic elements is utilized to serve as the exact solution in the calculation of relative errors. As clearly indicated by the obtained results, the relative percent errors significantly decrease as the number of elements increases whereas the rate of convergence approaches 2 for the linear case and is larger than 2.7 for the quadratic case as the meshes being refined. It should be remarked also that the rate of convergence for linear elements converges slower than that for quadratic elements.

Table 1: Relative percent error and rate of convergence of numerical solutions with linear elements (solution generated by a uniform mesh containing 128 quadratic elements is taken as the exact solution)

N	NDOFs	h/Λ	Error (%)	P
2	6	1	6.205856	-
4	10	0.5	1.817316	1.77
8	18	0.25	0.49006	1.89
16	34	0.125	0.12705	1.95
32	66	0.0625	0.033369	1.93
64	130	0.03125	0.008397	1.99

Table 2: Relative percent error and rate of convergence of numerical solutions with quadratic elements (solution generated by a uniform mesh containing 128 quadratic elements is taken as the exact solution)

N	NDOFs	h/Λ	Error (%)	P
2	10	1	0.8256033	-
4	18	0.5	0.1618244	2.35
8	34	0.25	0.0301914	2.42
16	66	0.125	0.0052689	2.52
32	130	0.0625	0.0008588	2.62
64	258	0.03125	0.0001292	2.73

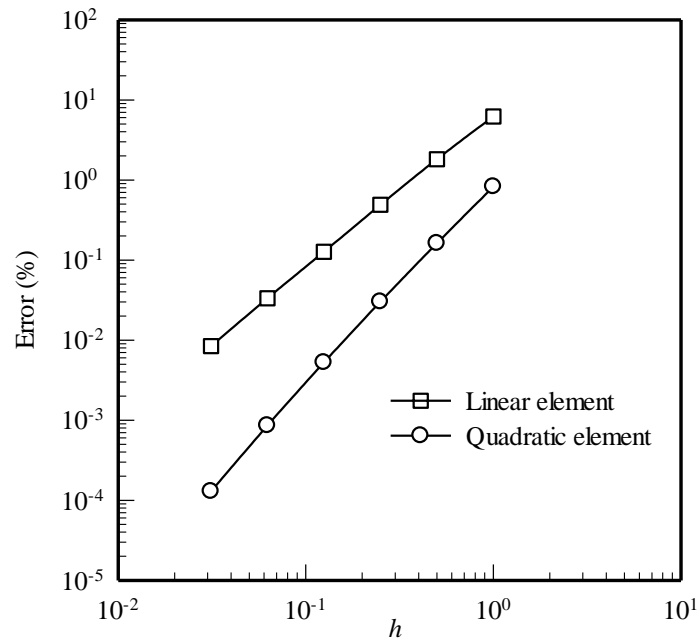


Figure 32: Relative percent error of numerical solutions generated by uniform meshes of linear and quadratic elements (solution generated by a uniform mesh containing 128 quadratic elements is taken as the exact solution)

To emphasize the computational efficiency of the proposed technique in terms of the number of degrees of freedom required to yield the converged solution, the single layer medium under a uniformly distributed normal traction at the top surface without the surface stresses is resolved by using the finite element method. In the analysis, the single layer is truncated with $L/a = 20$ and 8-node rectangular elements are employed in the discretization. The convergence of the finite element solutions is confirmed via numerical experiments over a series of meshes as reported in Figure 33. The converged FE solution is then plotted along with the converged SBFEM solution generated from a mesh containing only 16 uniform quadratic elements in Figure 34. As can be observed from those results, the SBFEM solution (generated by a mesh of 16 elements) has an excellent agreement with the FE solution (generated by 10240 elements with 64 element-layers along the vertical direction). This finding confirms that the implemented SBFEM requires a significantly less number of degrees of freedom in the discretization to obtain the solution of comparable quality than that of the standard finite element technique

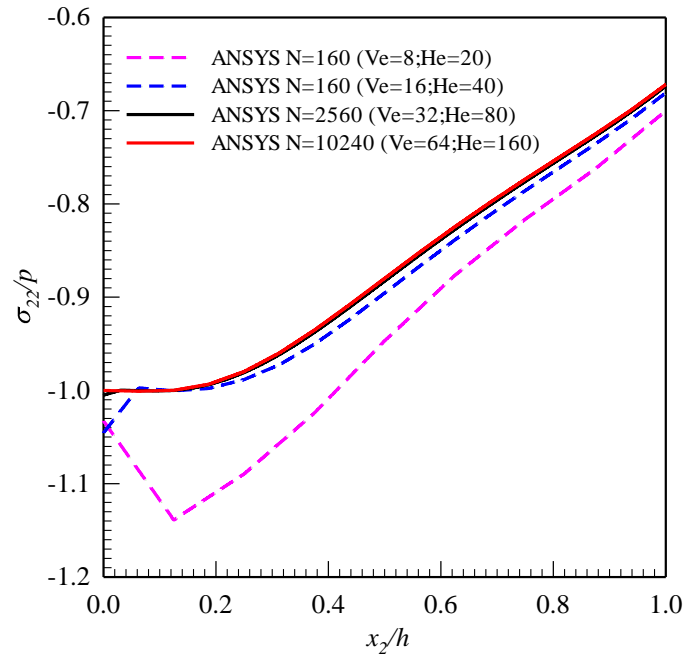


Figure 33: Convergence study of normalized vertical stress obtained from finite element method with meshes containing 8 nodes rectangular elements

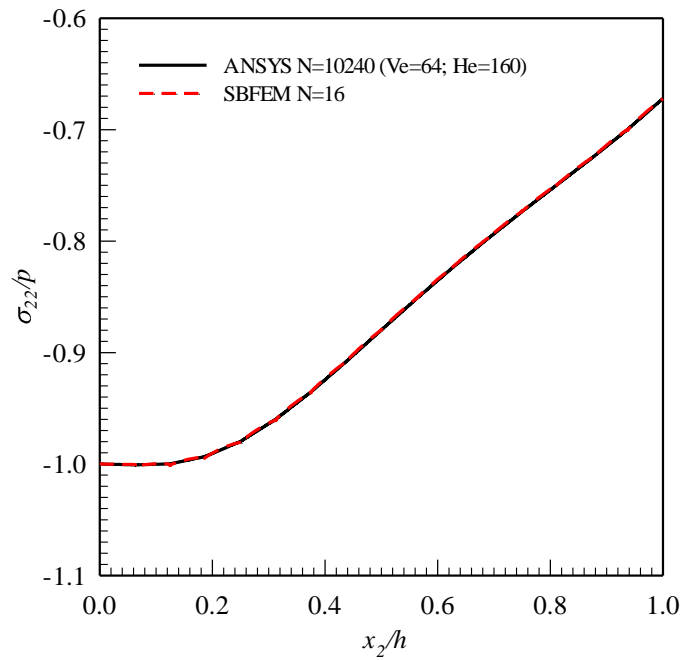


Figure 34: Comparison of converged normalized vertical stress from SBFEM (16 quadratic elements) and FEM (10240 8-node rectangular elements).

4.3.2. Uniformly distributed shear traction

In this section, a semi-infinite, rigid-based, elastic layer loaded by a uniformly distributed shear traction shown in Figure 17(b) is considered. The normalized horizontal displacement and normalized shear stress along the line of anti-symmetry, generated by meshes with linear and quadratic elements, are reported in Figures 35-36 and Figures 37-38, respectively, along with those proposed by [Intarit et al. \(2011\)](#). The convergence of numerical solutions for is clearly achieved for all cases as the mesh is refined and the good agreement between the converged and benchmark results is observed. Similar to the previous loading case, the quality of the approximate displacement field is apparently better than that of the stress field since the displacement is chosen as the primary unknown in the formulation and directly approximated following Eq. (2.12) whereas the stress field is obtained in the post-process and requires the derivatives of the displacement field. In addition, use of quadratic elements in the discretization can significantly improve the accuracy of the numerical solutions with use of relatively coarse meshes, especially when the stresses are of interest.

To additionally verify the proposed technique, results of the displacement and stress at various locations within the elastic layer are generated by a sufficiently fine mesh containing 128 quadratic elements and compared with the reference solutions obtained from the analytical technique proposed by [Intarit et al. \(2011\)](#) as shown in Figures 39-43. Clearly, the two solutions are hardly distinguishable when observed from the plots and this implies the correctness of results obtained from the present method. The contour plots of the normalized displacements and stresses are also reported in Figures 44-48 to not only illustrate the variation of field quantities in the neighborhood of the loading region but also see the significant influence of surface stresses.

The convergence behavior of computed numerical solutions can also be investigated in the same manner as in the previous loading case. The relative errors of SBFEM solutions generated by a series of meshes with linear and quadratic elements are computed by taking results from a fine mesh containing 128 quadratic elements as the exact solution. Results are then reported in, Table 4, and Figure 49. It is seen that

as the mesh is uniformly refined (i.e., the number of elements increases), the relative error reduces and this clearly indicates the convergence of the numerical solution for the entire domain. For this particular loading condition, the rate of convergence is approximately equal to 2 and 3 when linear and quadratic elements are utilized in the solution discretization.

The same problem is then reanalyzed by the finite element method using the same truncated domain (i.e., $L/a = 20$) and type of elements in the discretization. It is seen in the convergence study, as indicated in Figure 50, that to obtain the converged solution, it is required as many elements as 2560 (with 32 element-layers in the vertical direction). Such converged FE solution is found in good agreement with that generated by the implemented SBFEM with a relatively coarse mesh containing only 16 quadratic elements (see Figure 51). Thus, it clearly indicates that use of the SBFEM in the solution procedure can significantly reduce the number of elements (i.e., the number of nodal unknowns) in the discretization in comparison with the FEM. This partially confirms the computational efficiency of the implemented SBFEM.

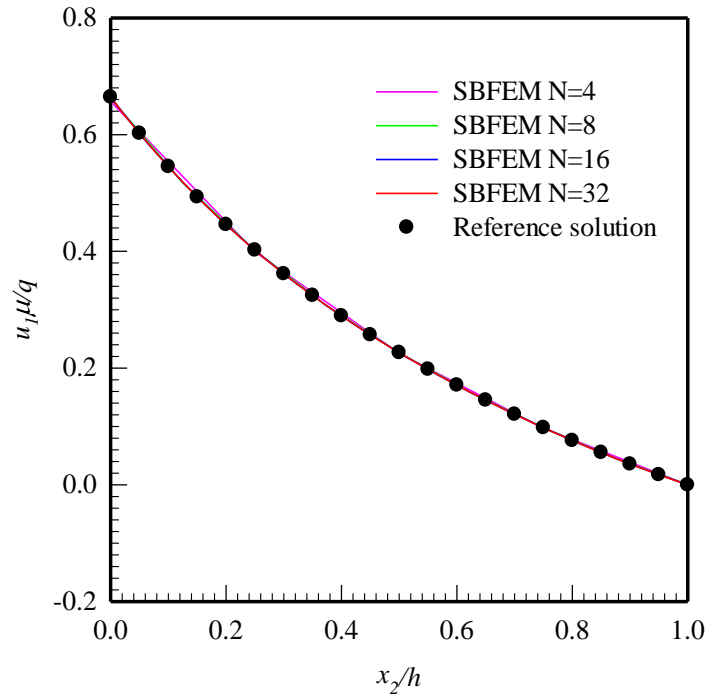


Figure 35: Normalized horizontal displacement along the line of anti-symmetry obtained from uniform meshes of linear elements

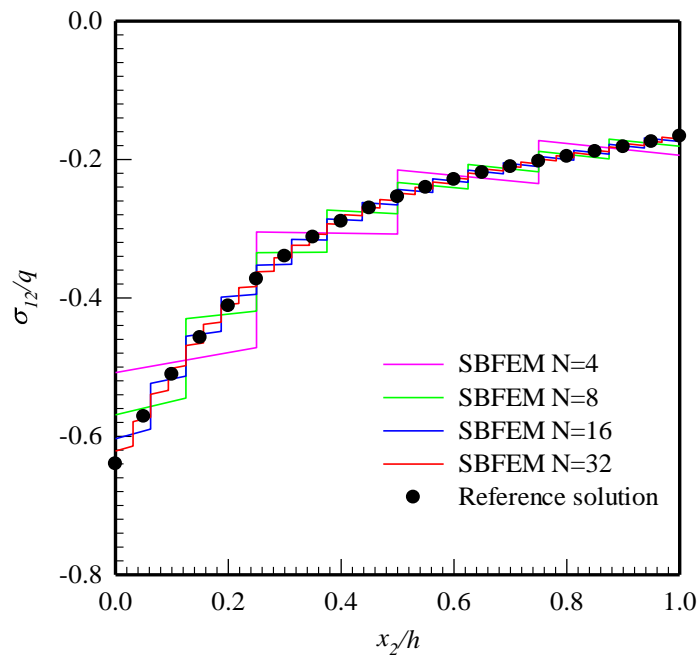


Figure 36: Normalized shear stress along the line of anti-symmetry obtained from uniform meshes of linear elements

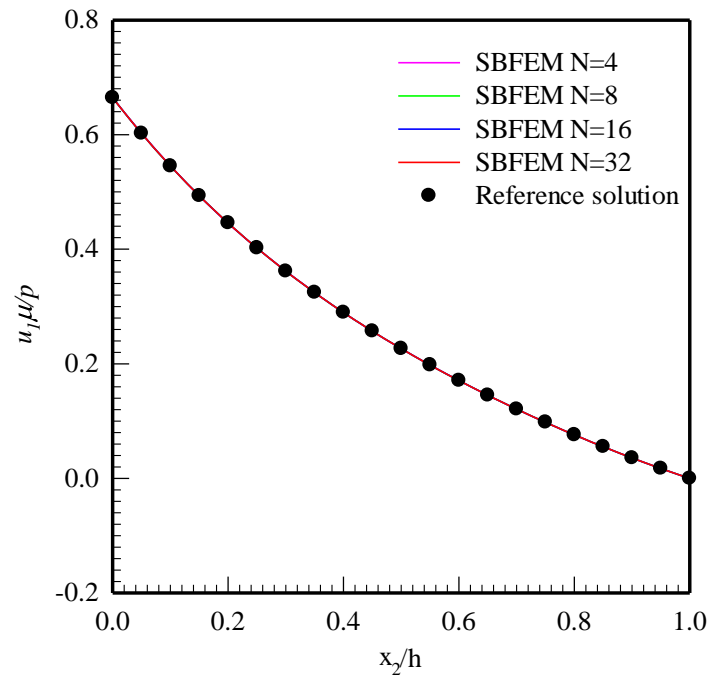


Figure 37: Normalized horizontal displacement along the line of anti-symmetry obtained from uniform meshes of quadratic elements

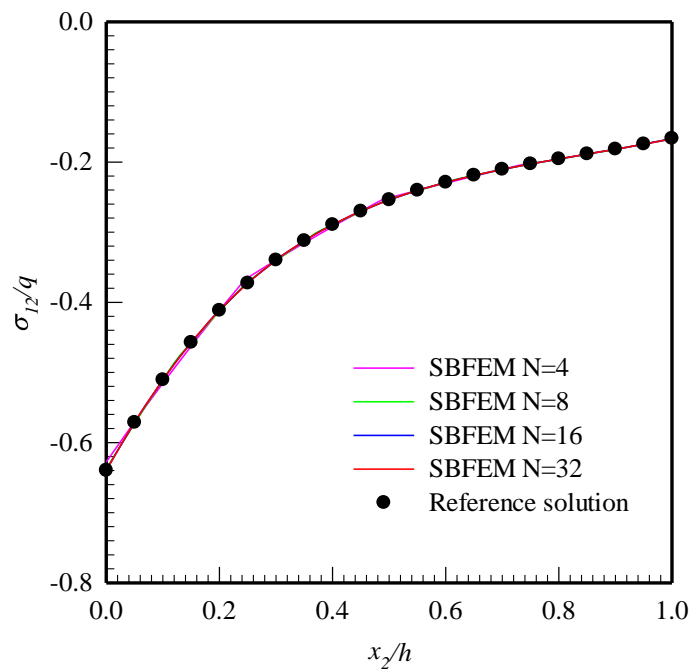


Figure 38: Normalized shear stress along the line of anti-symmetry obtained from uniform meshes of quadratic elements

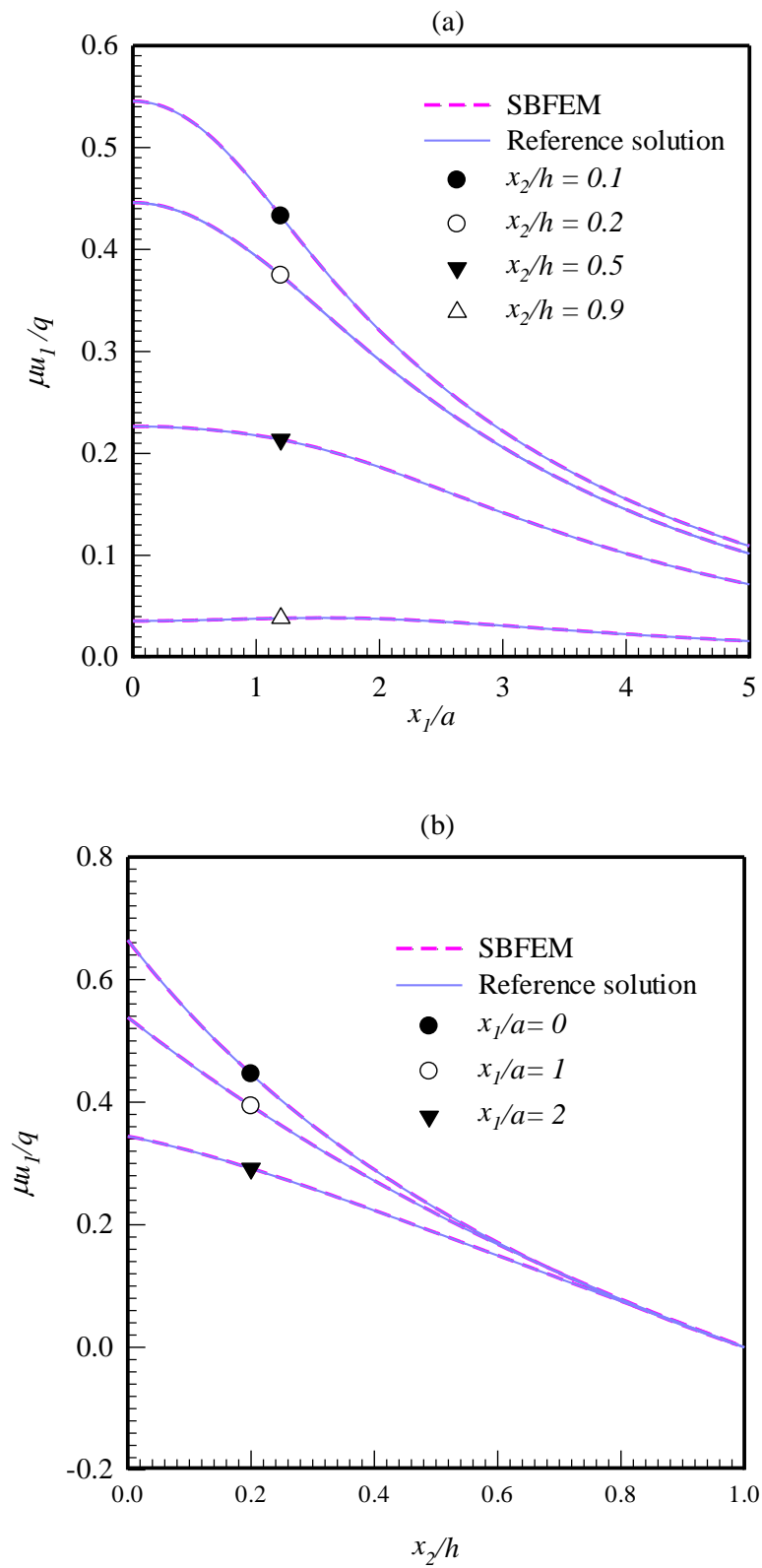


Figure 39: Normalized horizontal displacement along (a) x_1 -direction and (b) x_2 -direction generated by a uniform mesh containing 128 quadratic elements

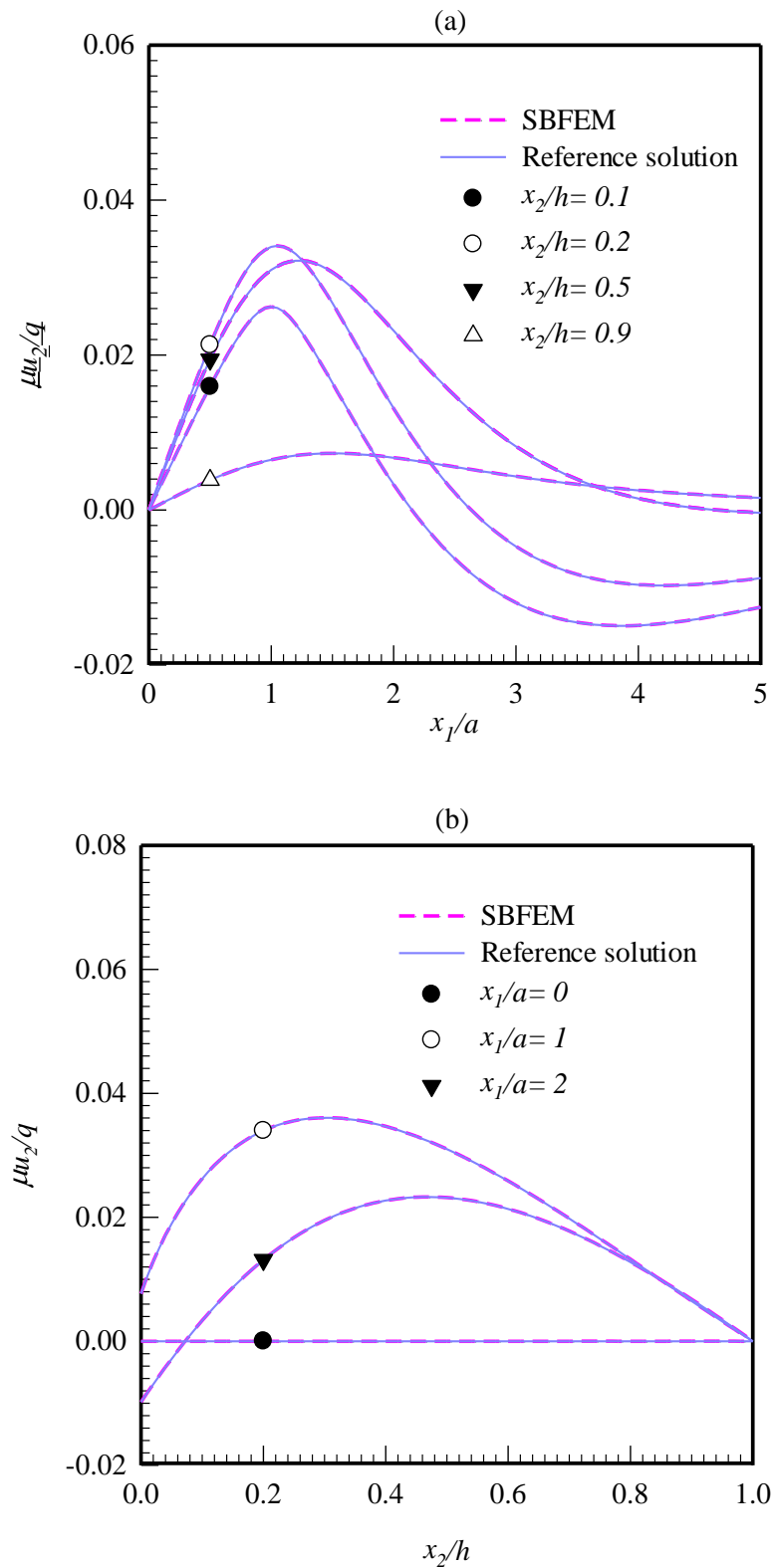


Figure 40: Normalized vertical displacement along (a) x_1 -direction and (b) x_2 -direction generated by a uniform mesh containing 128 quadratic elements

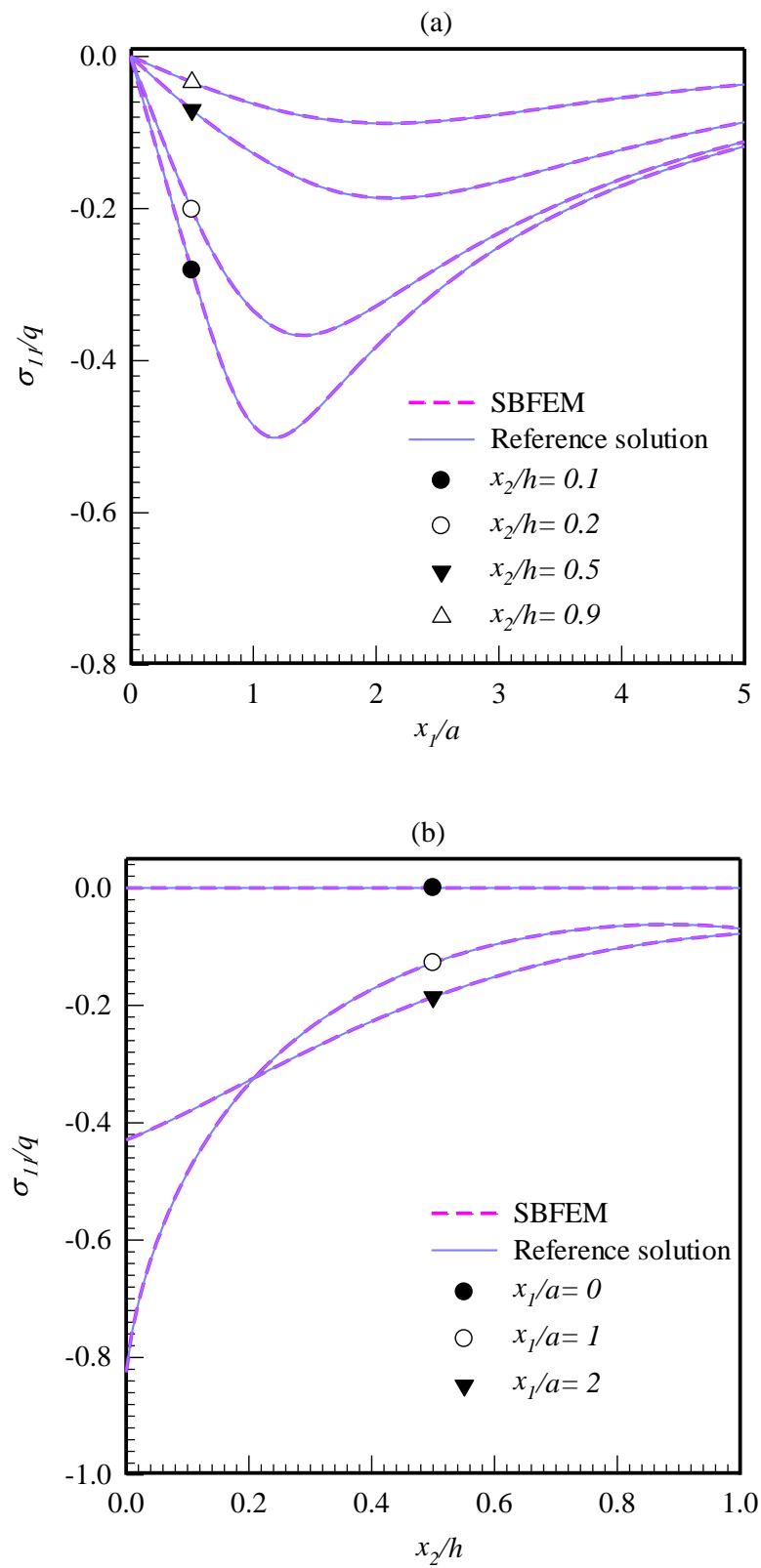


Figure 41: Normalized horizontal stress along (a) x_1 -direction and (b) x_2 -direction generated by a uniform mesh containing 128 quadratic elements

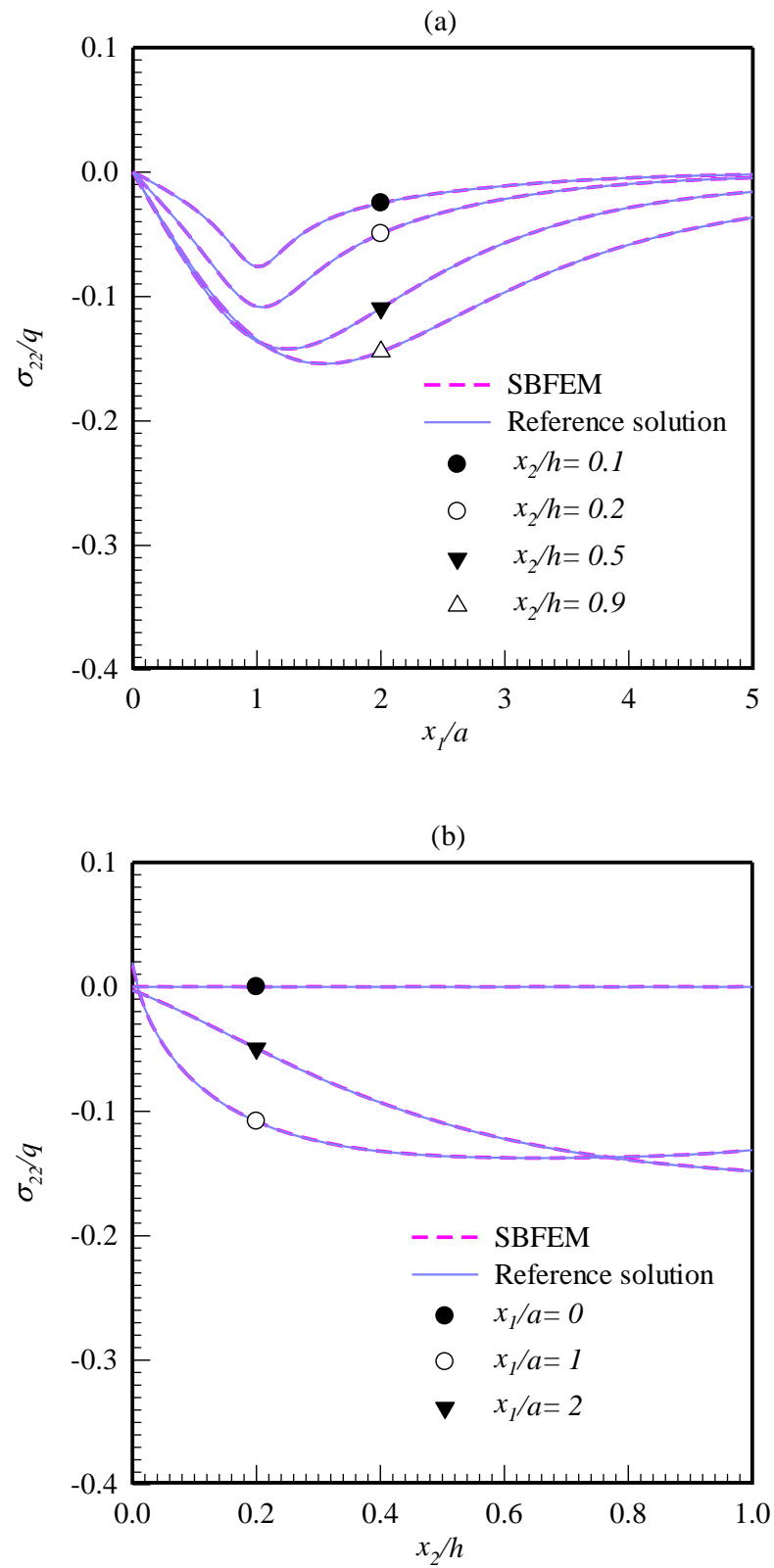


Figure 42: Normalized vertical stress along (a) x_1 -direction and (b) x_2 -direction generated by a uniform mesh containing 128 quadratic elements

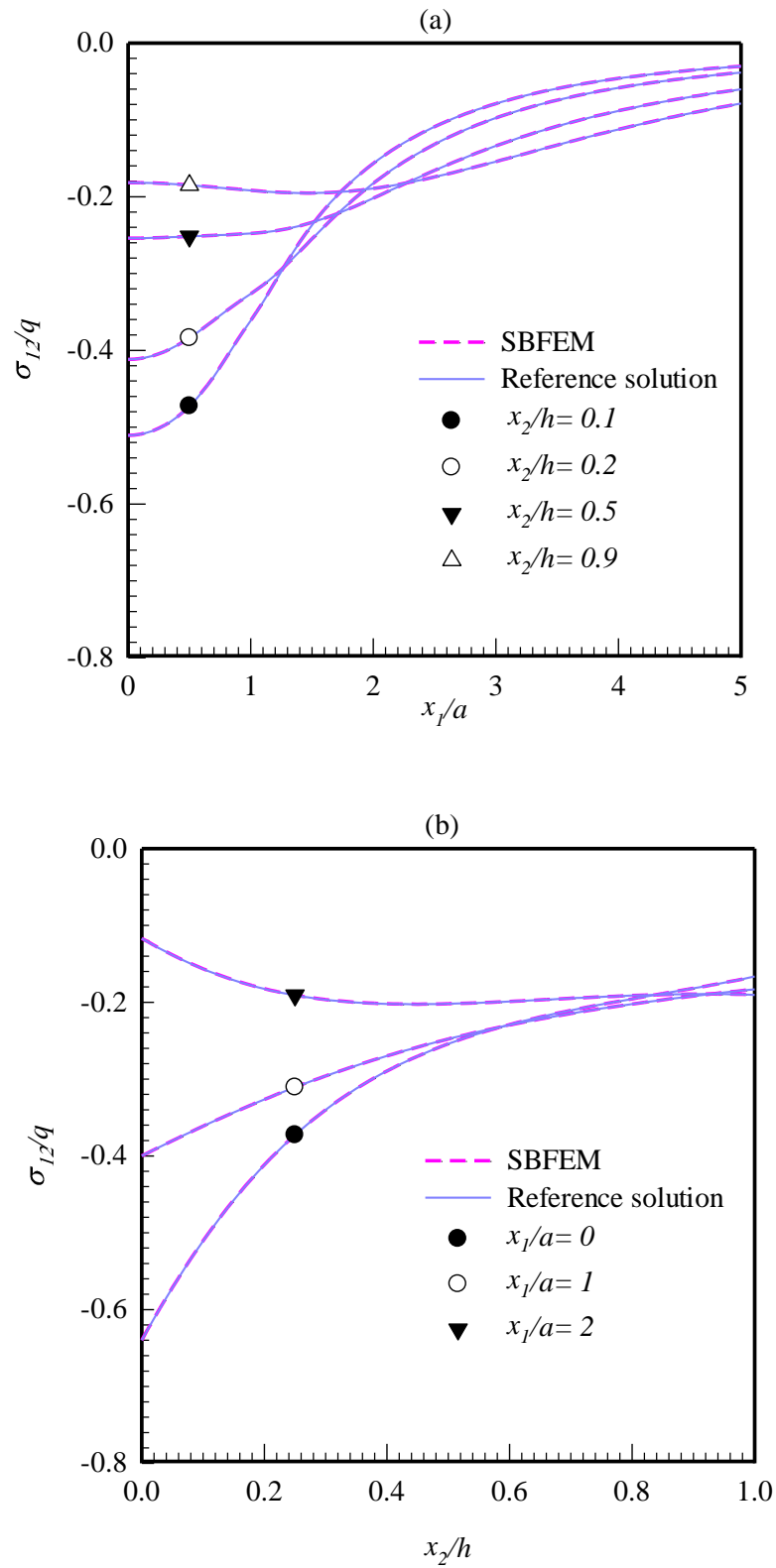


Figure 43: Normalized shear stress along (a) x_1 -direction and (b) x_2 -direction generated by a uniform mesh containing 128 quadratic elements

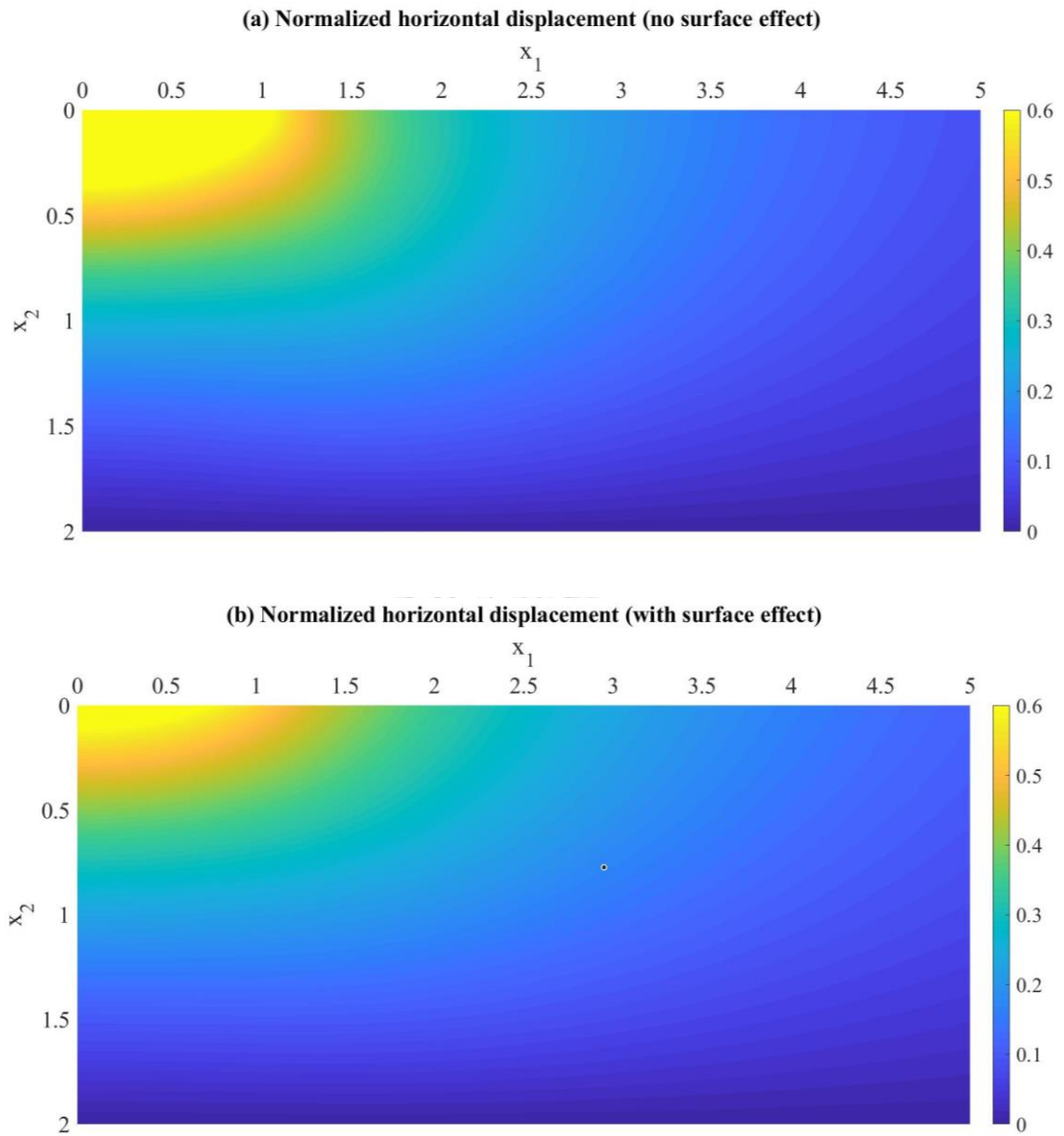


Figure 44: Contour plot of normalized horizontal displacement ($\mu u_1 / q$) of a rigid-based elastic layer under uniformly distributed shear traction: (a) without surface effect and (b) with surface effect

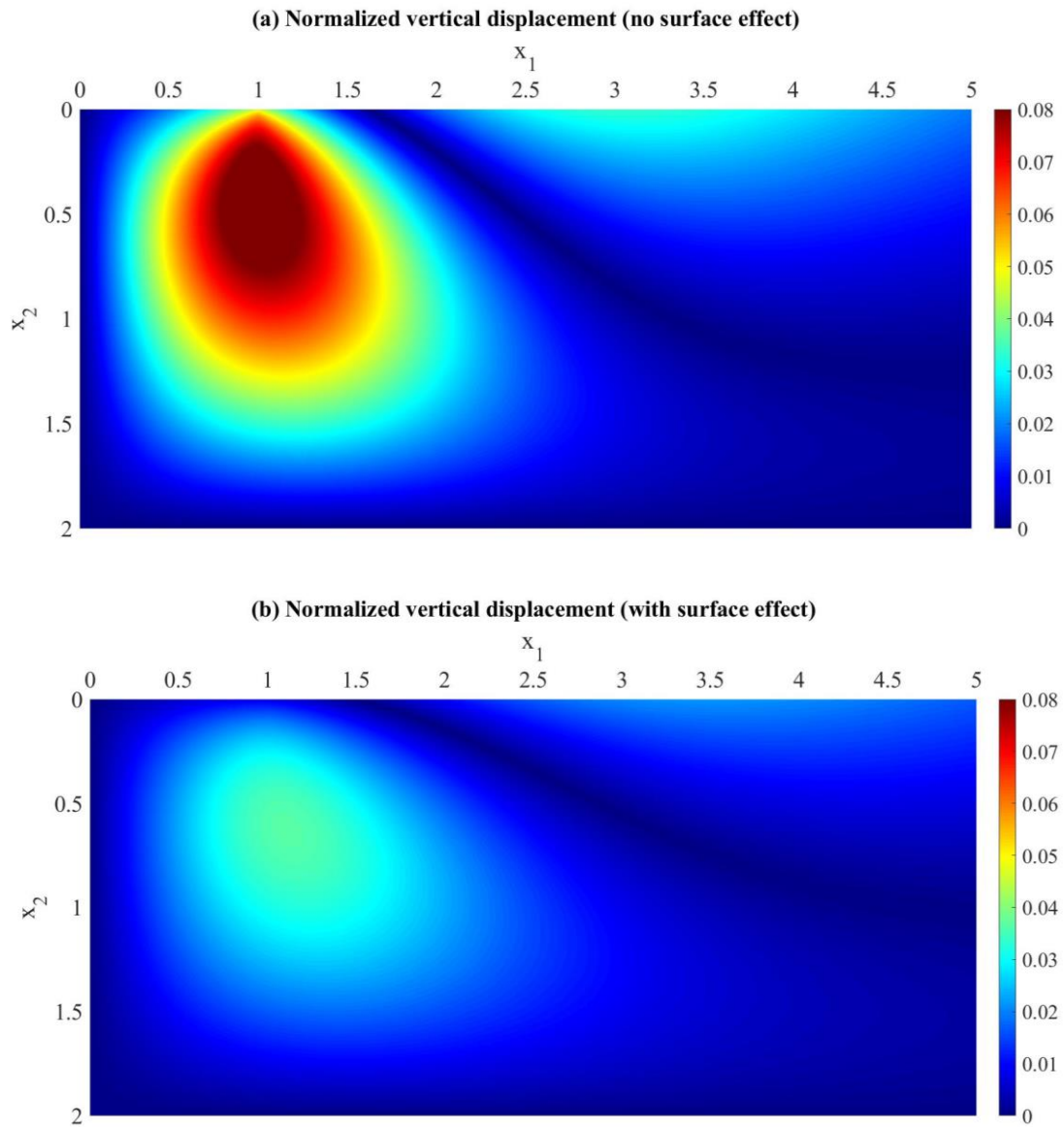


Figure 45: Contour plot of normalized vertical displacement ($\mu u_2 / q$) of a rigid-based elastic layer under uniformly distributed shear traction: (a) without surface effect and (b) with surface effect

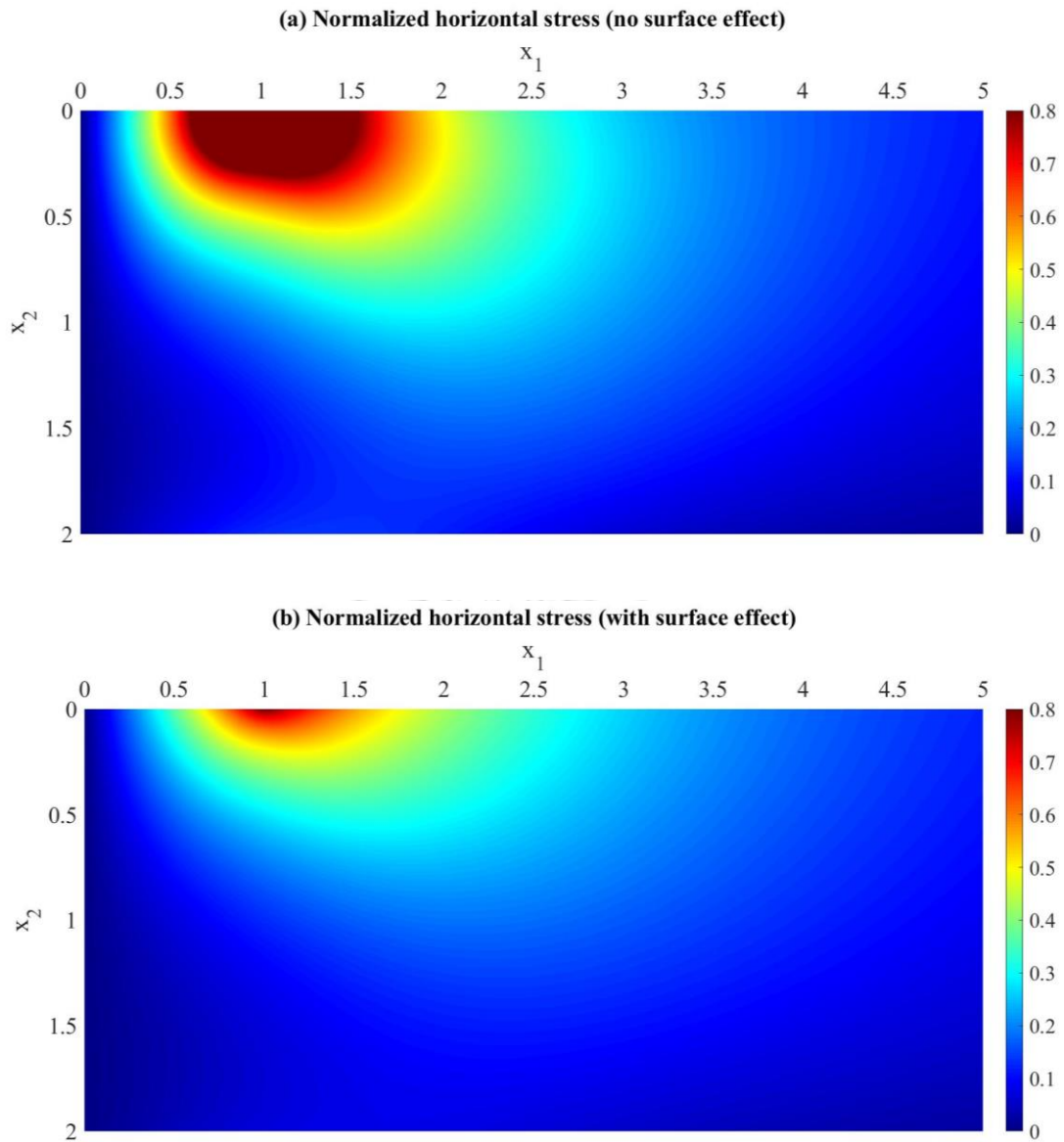


Figure 46: Contour plot of normalized horizontal stress ($-\sigma_{11}/q$) of a rigid-based elastic layer under uniformly distributed shear traction: (a) without surface effect and (b) with surface effect

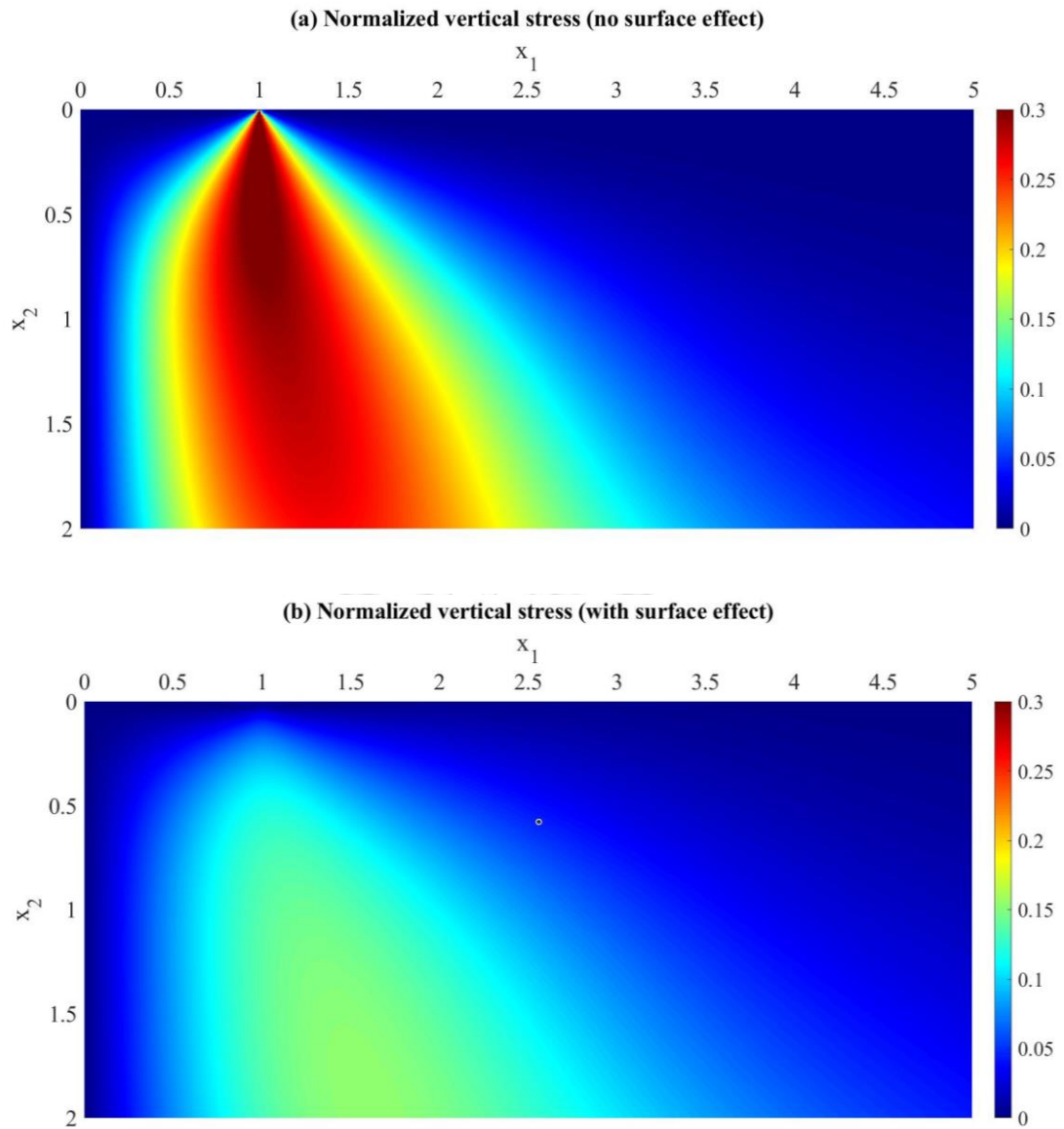


Figure 47: Contour plot of normalized vertical stress ($-\sigma_{22}/q$) of a rigid-based elastic layer under uniformly distributed shear traction: (a) without surface effect and (b) with surface effect

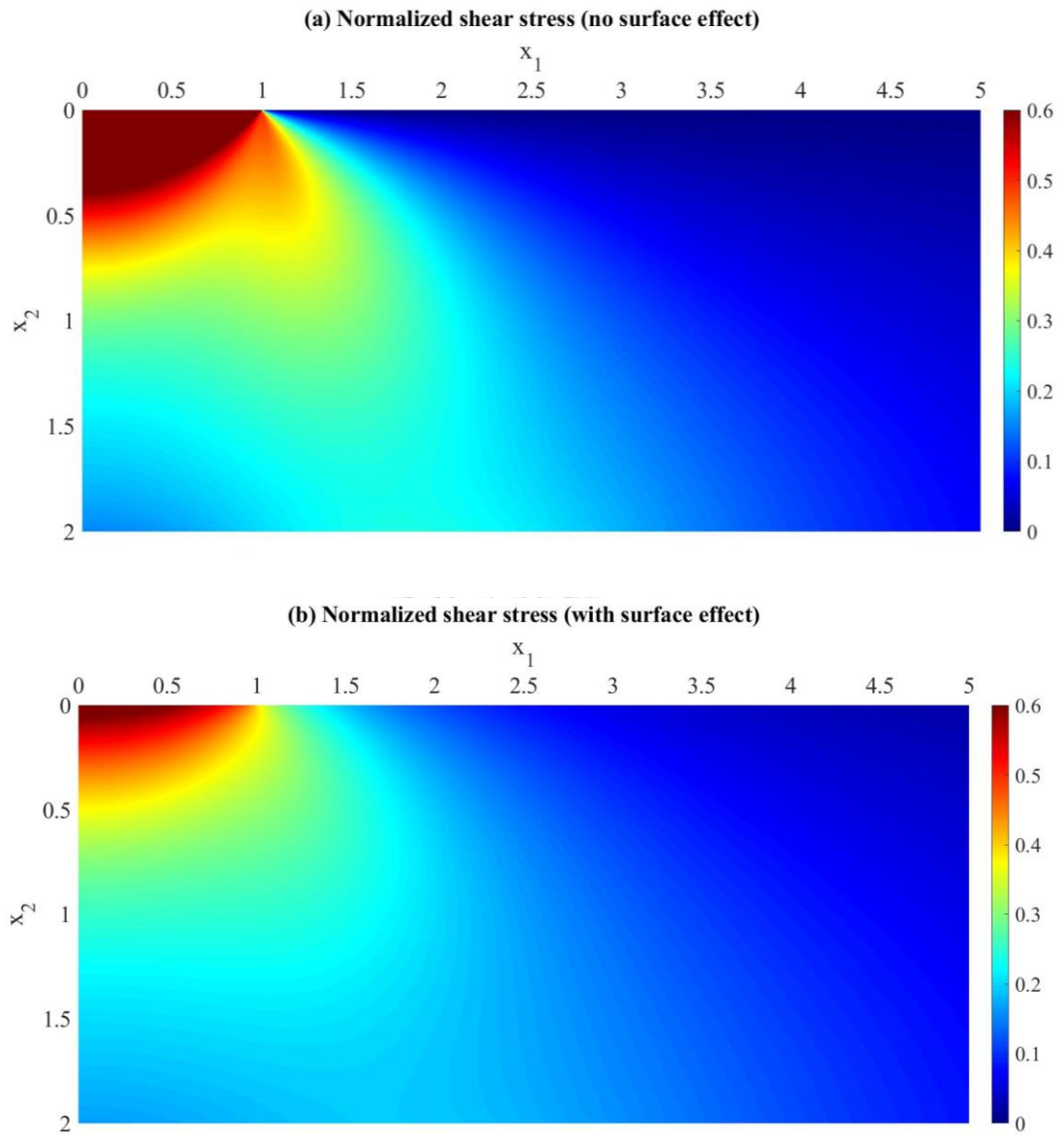


Figure 48: Contour plot of normalized shear stress ($-\sigma_{12} / q$) of a rigid-based elastic layer under uniformly distributed shear traction: (a) without surface effect and (b) with surface effect

Table 3: Relative percent error and rate of convergence of numerical solutions with linear elements (solution generated by a uniform mesh containing 128 quadratic elements is taken as the exact solution)

N	NDOFs	h	Error (%)	p
2	6	1	4.5439981	-
4	10	0.5	1.269541	1.840
8	18	0.25	0.3319228	1.935
16	34	0.125	0.0843503	1.976
32	66	0.0625	0.0213593	1.982
64	130	0.03125	0.0053496	1.997

Table 4: Relative percent error and rate of convergence of numerical solutions with quadratic elements (solution generated by a uniform mesh containing 128 quadratic elements is taken as the exact solution)

N	NDOFs	h	Error (%)	p
2	10	1	0.5381754	-
4	18	0.5	0.0872886	2.624
8	34	0.25	0.0133682	2.707
16	66	0.125	0.0019596	2.770
32	130	0.0625	2.77E-04	2.822
64	258	0.03125	3.57E-05	2.957

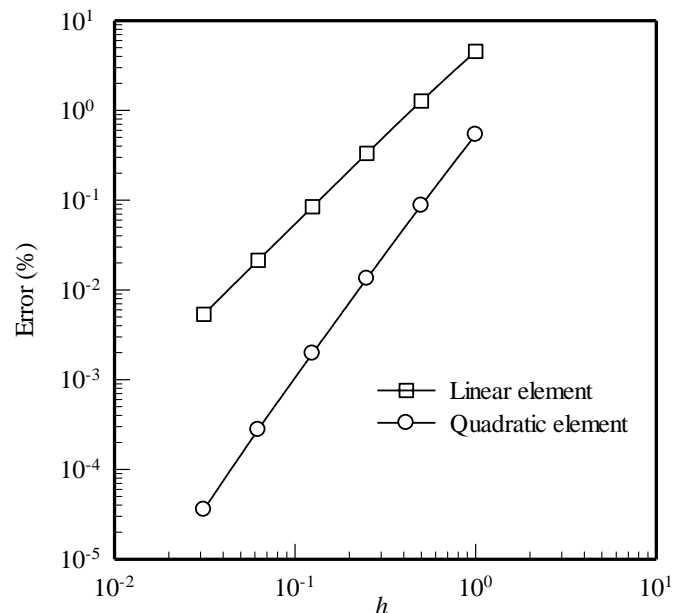


Figure 49: Relative percent error of numerical solutions generated by uniform meshes of linear and quadratic elements (solution generated by a uniform mesh containing 128 quadratic elements is taken as the exact solution)

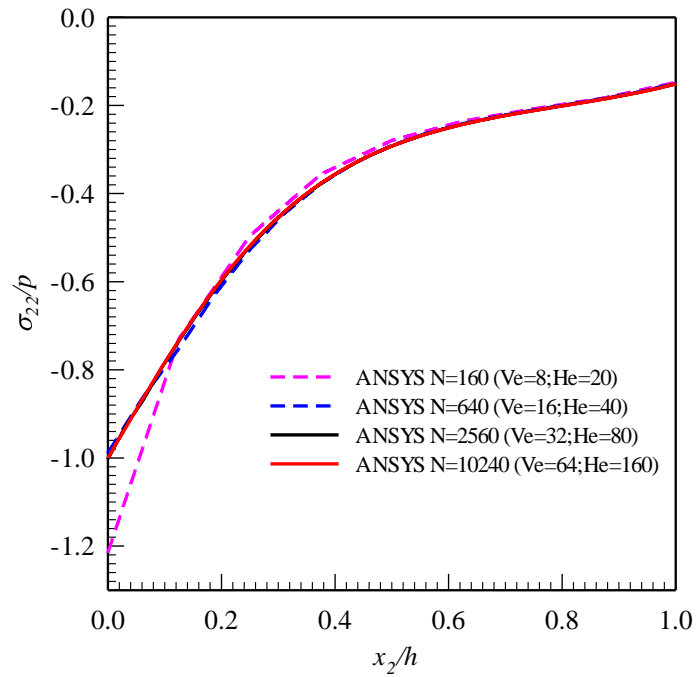


Figure 50: Convergence study of normalized vertical stress obtained from finite element method with meshes containing 8 nodes rectangular elements

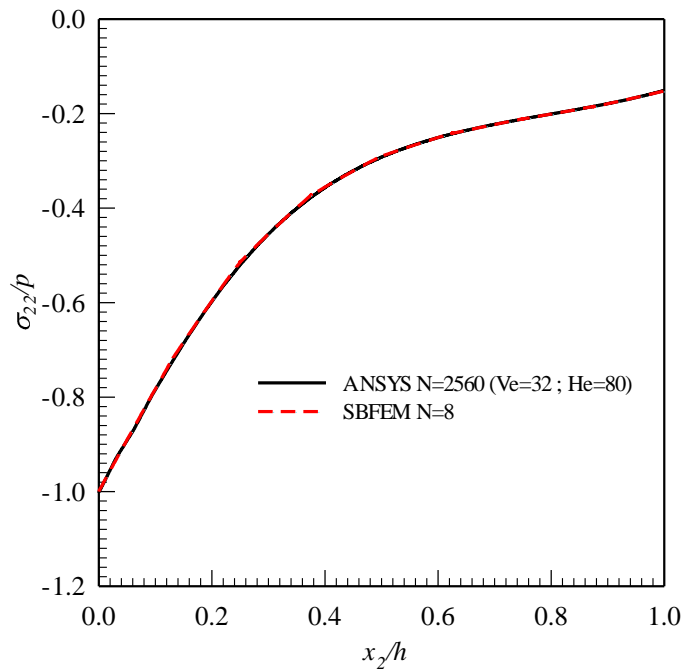


Figure 51: Comparison of converged normalized vertical stress from SBFEM (16 quadratic elements) and FEM (2560 8-node rectangular elements).

4.4. Surface loaded multilayer media

Consider, as a final example, a semi-infinite, rigid-based, layered elastic medium subjected to a uniformly distributed normal traction p over the normalized length $2\bar{a}$ ($\bar{a} = a/\Lambda = 1$) as shown schematically in Figure 52. This representative problem is chosen to demonstrate the capability of the proposed SBFEM in handling multi-layer media. The body is composed of four layers with the same normalized thickness ($\bar{h}_1 = \bar{h}_2 = \bar{h}_3 = \bar{h}_4 = 0.5$). The first and third layers are made of Si[100] whereas the second and fourth layers are made of Al[111] whose material properties are clearly indicated in Table 5. Properties of the top material surface are taken to be the same as those of Si[100] whereas those of the three material interfaces are taken to be the same as the surface properties of Al[111]. It is important to note that all involved length scales are normalized by the intrinsic length scale of the material surface of Al[111], i.e., $\Lambda = \Lambda_1 = 0.1529 \text{ nm}$.

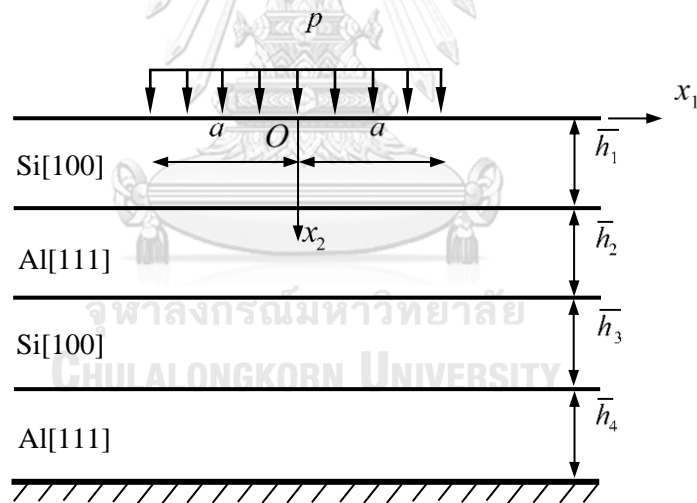


Figure 52: Schematic of a semi-infinite, rigid-based, Si/Al layered elastic medium subjected to uniformly distributed normal traction p over the normalized length $2\bar{a}$

First, the relative errors and the rate of convergence of the SBFEM solutions using the linear elements in the discretization are explored. A sufficiently fine, uniform mesh containing 128 quadratic elements is employed to generate the converged solution and further used in the estimation of the relative error of computed solutions. Resulting relative errors and the rate of convergence are then reported in Table 6 and

Figure 53, when the influence of the surface stresses is fully ignored, and in Table 7 and Figure 54, when the surface stresses are taken into account. It is seen that as the number of elements increases, the proposed numerical scheme yields the converged solution and the rate of convergence is approximately equal to 2 for both cases.

Table 5: Material properties of Al [111] and Si [100]

Material parameters	Al[111]	Si[100]
λ_i [GPa]	58.1700	78.0859
μ_i [GPa]	26.1300	40.2256
λ_i^s [N/m]	6.8511	4.4939
μ_i^s [N/m]	-0.3760	2.7779
τ_i^s [N/m]	1.0000	0.6056
κ_i [N/m]	6.0991	0.03125
Λ_i [nm]	0.1529	0.1674

Table 6: Relative percent error and rate of convergence of numerical solutions generated by linear elements without surface stresses (solution generated by a uniform mesh containing 128 quadratic elements is taken as the converged solution)

N	NDOFs	h	Error (%)	P
4	10	0.5	2.3304749	-
8	18	0.25	0.6685888	1.80
16	34	0.125	0.1825218	1.87
32	66	0.0625	0.0491981	1.89
64	130	0.03125	0.0129747	1.92

Table 7: Relative percent error and rate of convergence of numerical solutions generated by linear elements with surface stresses (solution generated by a uniform mesh containing 128 quadratic elements is taken as the converged solution)

N	NDOFs	h	Error (%)	P
4	10	0.5	2.2709806	-
8	18	0.25	0.6021653	1.92
16	34	0.125	0.1554835	1.95
32	66	0.0625	0.0395592	1.97
64	130	0.03125	0.0099776	1.99

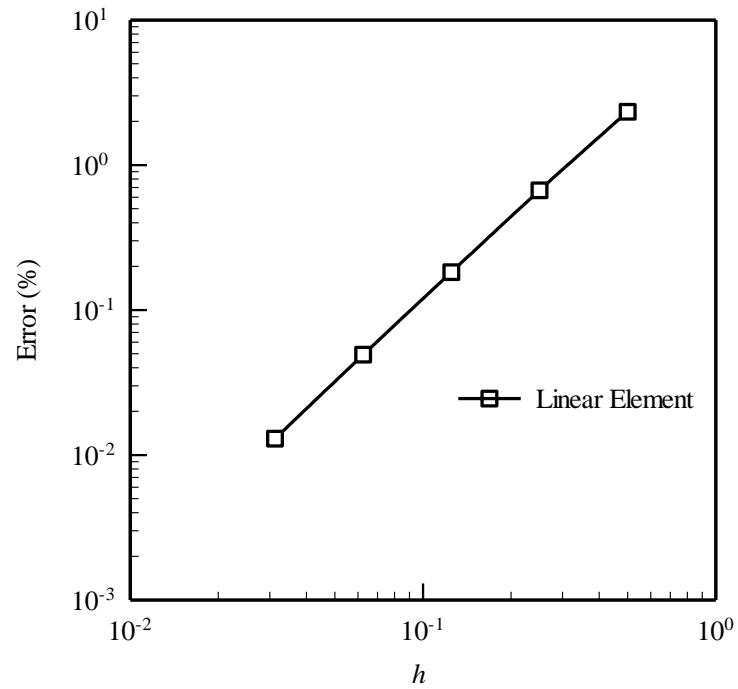


Figure 53: Relative percent error of numerical solutions generated by uniform meshes of linear elements without surface stresses

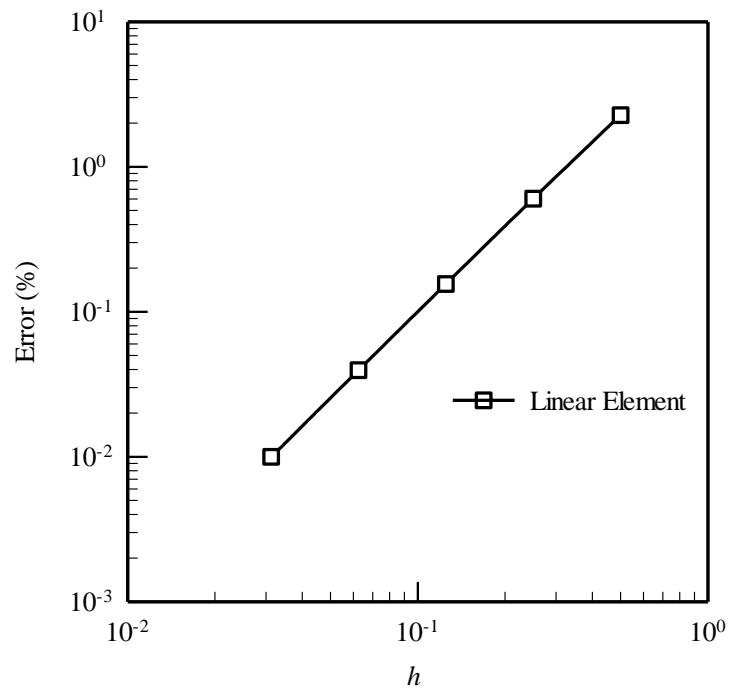


Figure 54: Relative percent error of numerical solutions generated by uniform meshes of linear elements with surface stresses

To further explore the mechanical responses of the layered medium with and without the influence of surface stresses, the normalized vertical displacement and normalized vertical stress across the thickness of the layered medium and along normalized horizontal and vertical direction are reported in Figures 55-58. As can be seen in these figures, the presence of surface stresses significantly influence the elastic response of the bulk material. In particular, the normalized vertical displacement and vertical stress, when the surface stress are taken into account, are relatively lower over the loading region and become higher outside the loading area than those for the classical case. It is also found that the influence of the surface stress on the elastic field becomes more prominent at a region relatively close to the surface and material interfaces and a region close to the loading area. From results shown in Figure 58, the remarkable changes of both the normalized vertical displacement and stress at each layer can be observed when the surface stresses are taken into account. In addition, the vertical stress is always continuous at the material interfaces for the classical case but clearly discontinuous when the surface stresses are present. To clearly depict the variation of the displacement and stress within the layered medium and emphasize the significant influence of the surface stresses on the field quantities as discussed above, the contour plots of the normalized displacement and stress with and without the presence of surface stresses are also reported in Figures 59-63.

Similar to the previous two problems, the computational efficiency of the implemented SBFEM in comparison with the standard finite element method is also investigated. In the finite element analysis, the layered medium without the surface effect is considered and truncated with $L/a = 20$, and 8-node rectangular elements are, again, used in the discretization. Results from the convergence study of the representative FE solutions as shown in Figure 64 and the comparison with the converged SBFE solution shown in Figure 65 indicate that it is required only 16 quadratic elements in the SBFE analysis to generate the solution of comparable accuracy to that from the FEM. The computational efficiency and the effort in the discretization of the proposed technique should be additionally confirmed.

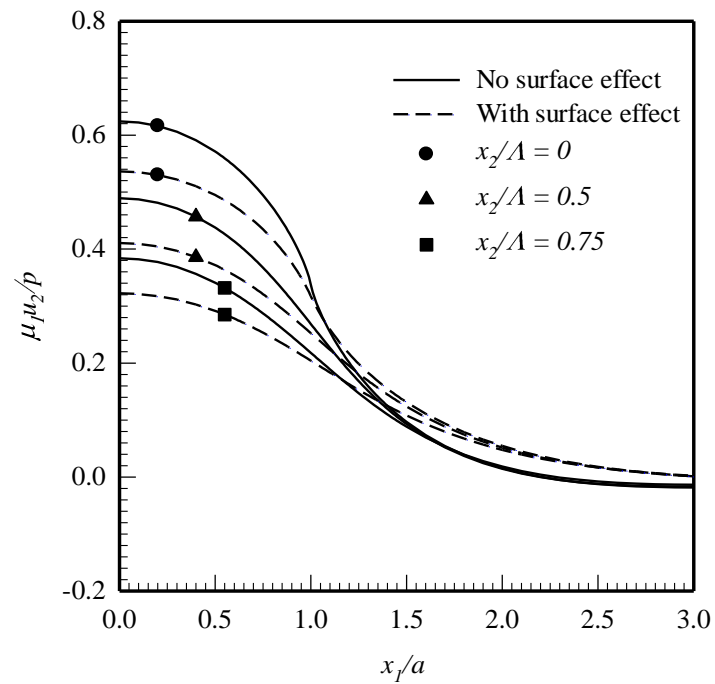


Figure 55: Normalized vertical displacement of Si/Al layered medium along x_1 - direction generated by a uniform mesh containing 128 quadratic elements

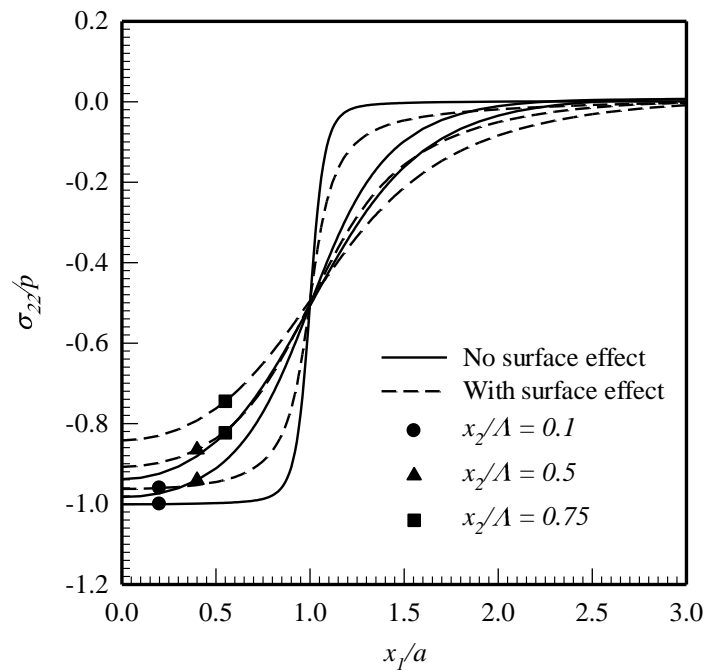


Figure 56: Normalized vertical stress of Si/Al layered medium along x_1 -direction generated by a uniform mesh containing 128 quadratic elements

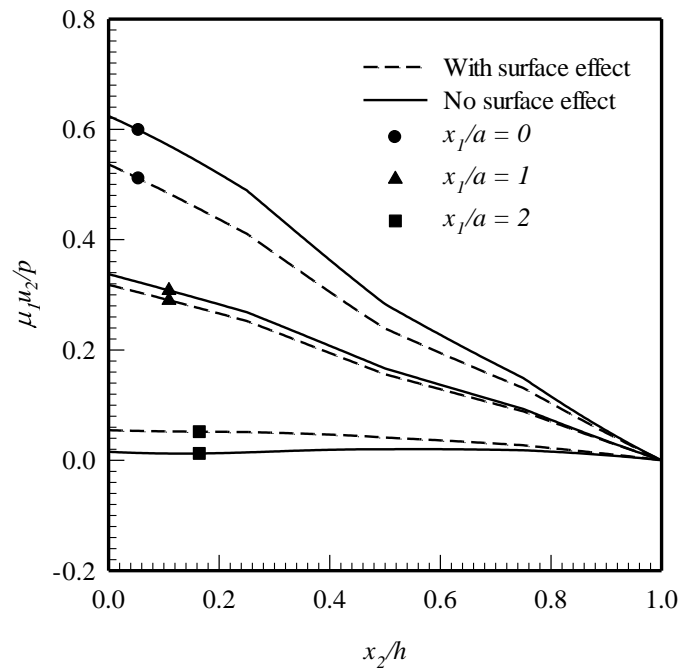


Figure 57: Normalized vertical displacement of Si/Al layered medium along x_2 -direction generated by a uniform mesh containing 128 quadratic elements

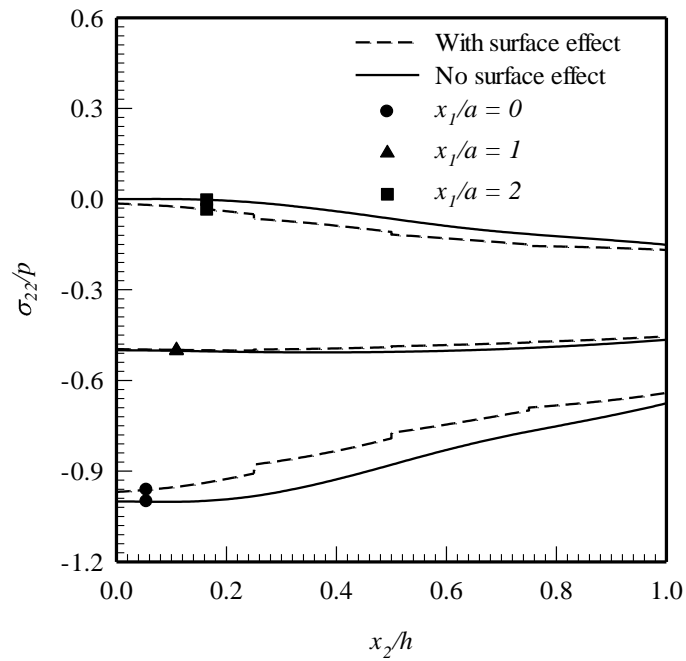


Figure 58: Normalized vertical stress of Si/Al layered medium along x_2 -direction generated by a uniform mesh containing 128 quadratic elements

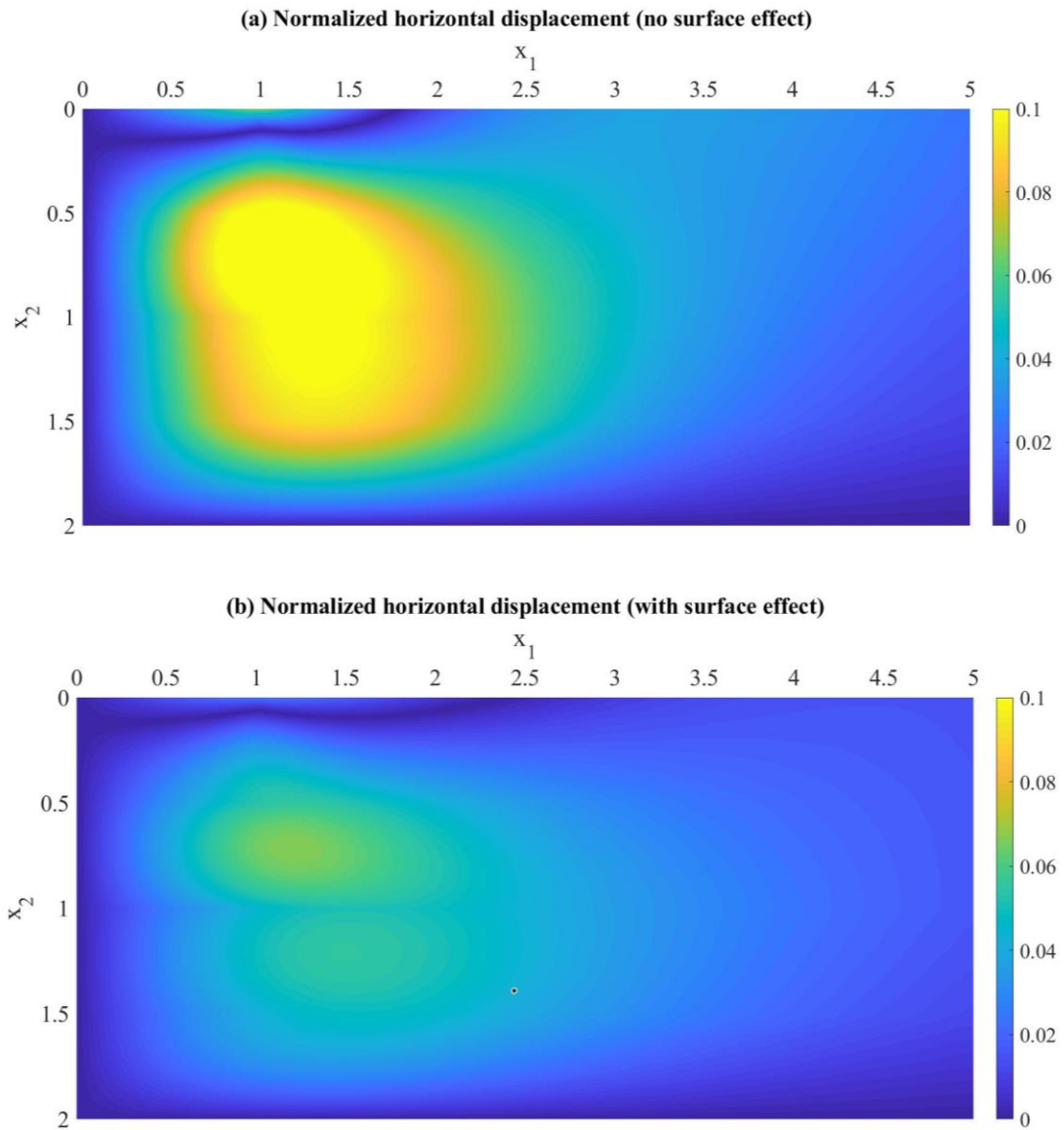


Figure 59: Contour plot of normalized horizontal displacement ($\mu u_1 / q$) of Si/Al layered medium under uniformly distributed normal traction: (a) without surface effect and (b) with surface effect

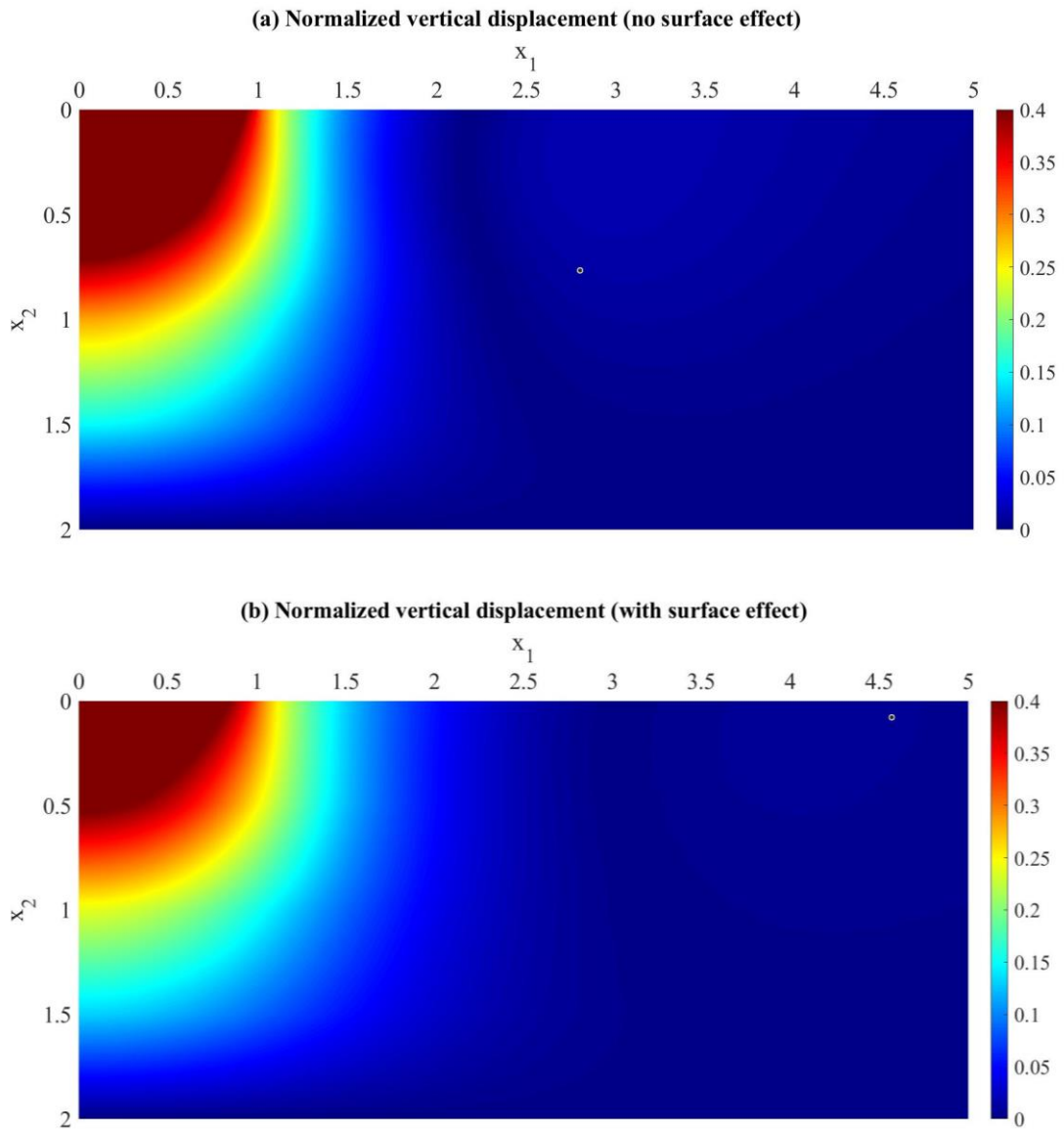


Figure 60: Contour plot of normalized horizontal displacement ($\mu u_2 / q$) of Si/Al layered medium under uniformly distributed normal traction: (a) without surface effect and (b) with surface effect

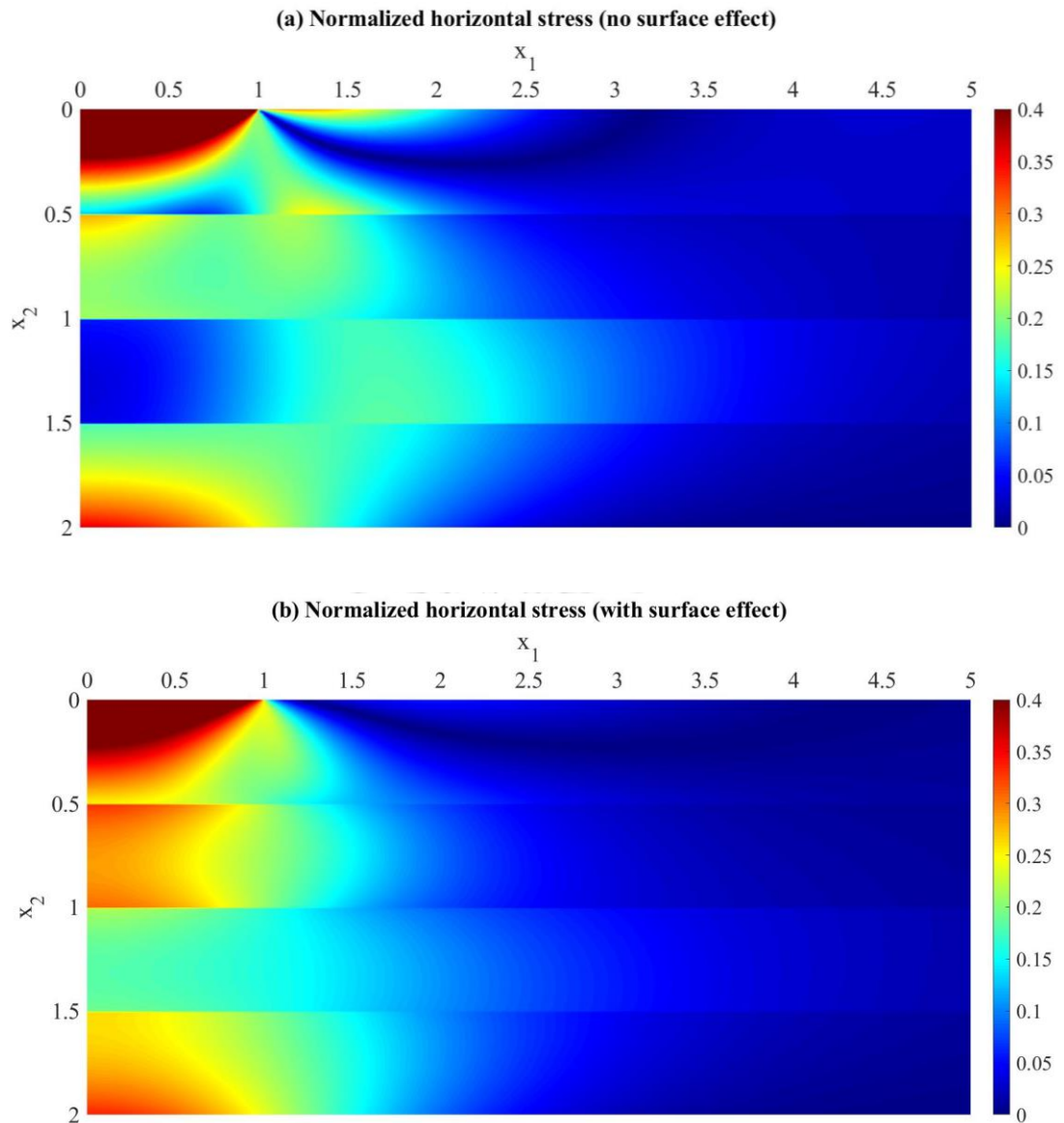


Figure 61: Contour plot of normalized horizontal stress ($-\sigma_{11} / p$) of Si/Al layered medium under uniformly distributed normal traction: (a) without surface effect and (b) with surface effect

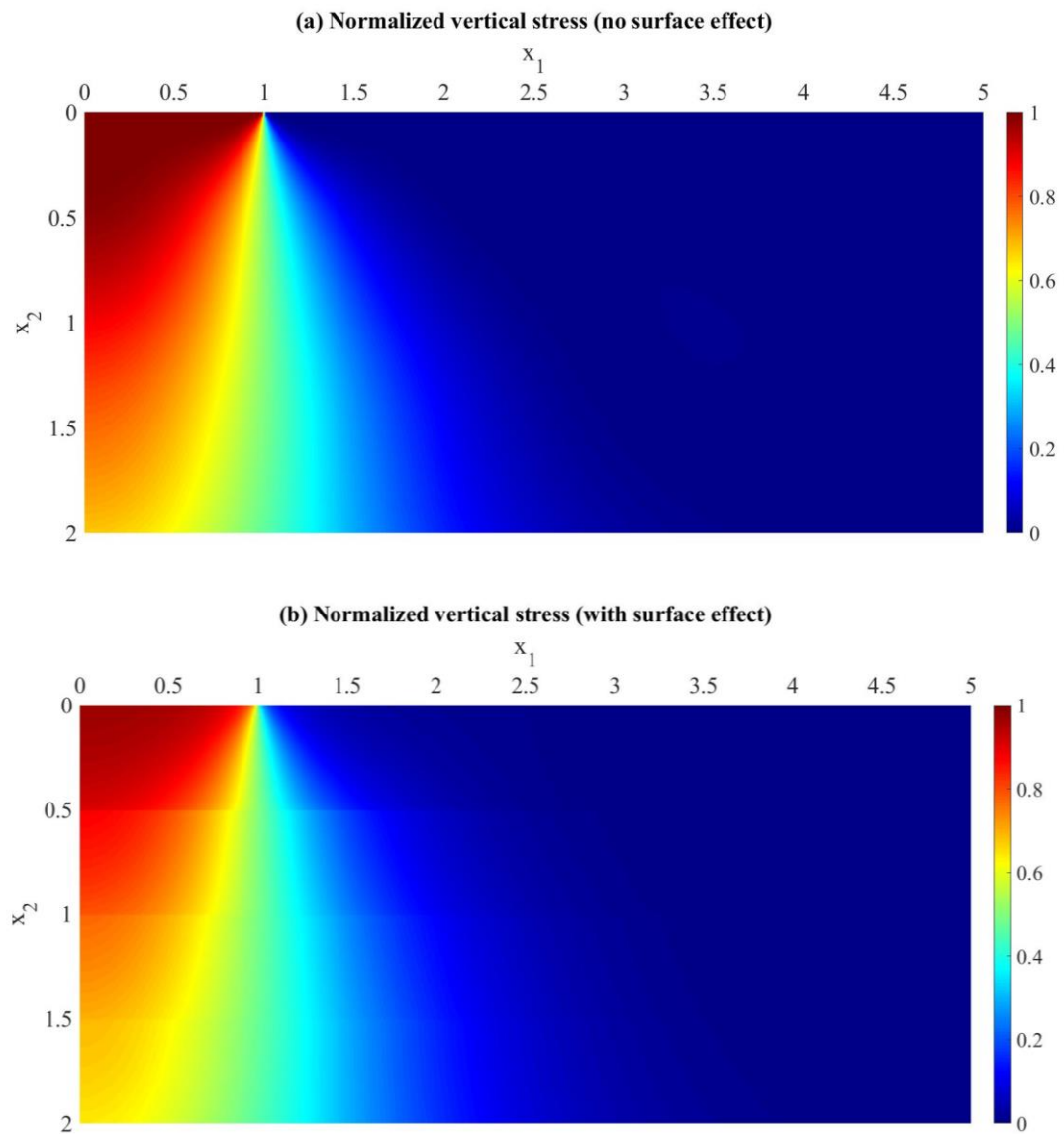


Figure 62: Contour plot of normalized vertical stress ($-\sigma_{22} / p$) of Si/Al layered medium under uniformly distributed normal traction: (a) without surface effect and (b) with surface effect

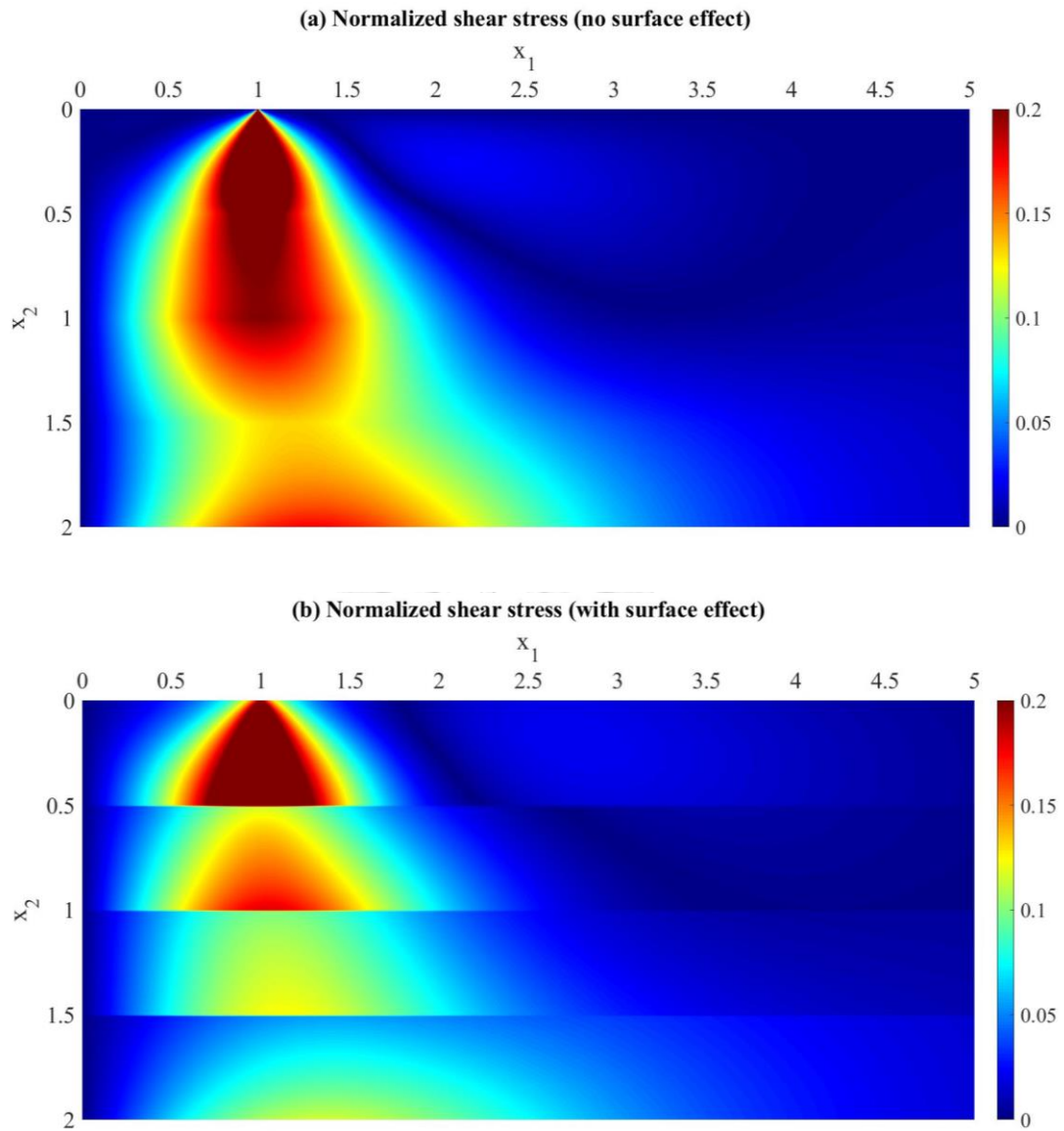


Figure 63: Contour plot of normalized shear stress ($-\sigma_{12} / p$) of Si/Al layered medium under uniformly distributed normal traction: (a) without surface effect and (b) with surface effect

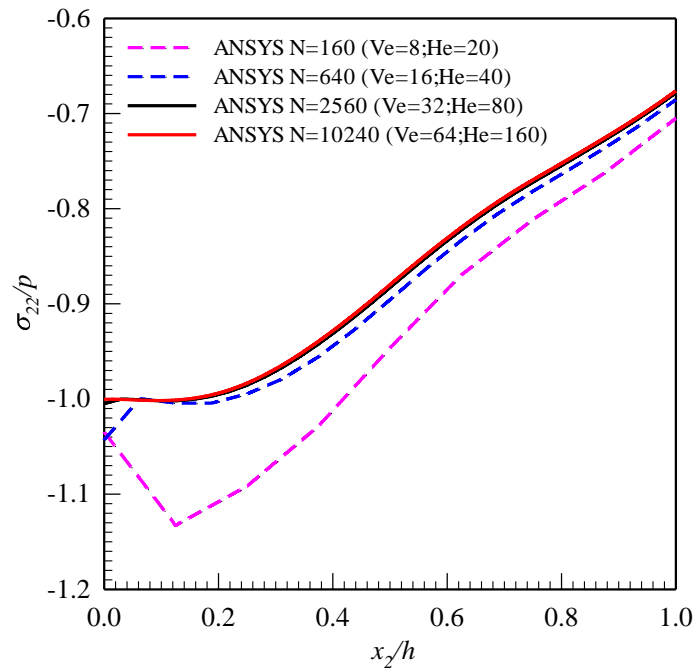


Figure 64: Convergence of normalized vertical stress generated from 8 nodes rectangular element of ANSYS

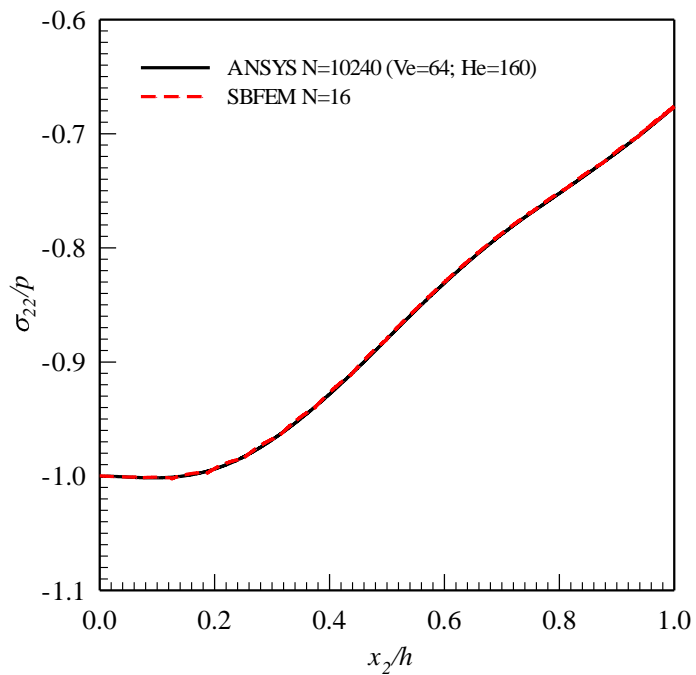


Figure 65: Comparison of normalized vertical stress generated from 16 quadratic element of SBFEM and 10240 element of ANSYS.

CHAPTER 5

CONCLUSIONS

An efficient and accurate numerical approximation based on the scaled boundary finite element method has been developed for determining the mechanical response of surface loaded layered media with the consideration of surface stress effects. In the formulation, the governing equations of the bulk layers have been established from the classical theory of linear elasticity together with the use of SBFEM procedure whereas those of the material surface and the material interfaces have been obtained from a complete version of Gurtin-Murdoch surface elasticity theory. By enforcing the continuity of the displacement and traction at interface of the material surfaces and the bulk layers, it leads to a system of linear non-homogenous ordinary differential equations governing the nodal functions. A general solution of the resulting system of ODEs has been constructed analytically via standard procedures and then used together with the domain decomposition scheme and the boundary conditions to form a system of linear algebraic equations governing nodal degrees of freedom of the whole layered medium.

The convergence, accuracy, and capability of the proposed technique have been fully investigated by considering three different scenarios of surface-loaded media including the half-plane, the single-layer medium, and the multi-layer medium. Results obtained from an extensive numerical study have indicated that the proposed SBFEM essentially yields the converged solutions as the discretization is refined. The rate of convergence of the numerical solutions via the use of linear elements in the approximation has been found approximately equal to 2 for all cases considered whereas that for the quadratic elements seems problem dependent. For instance, the rate of convergence obtained in the analysis of a single layer medium with quadratic elements approaches 3 for the uniformly distributed shear traction but still does not converge (within a series of meshes used in the numerical study) for the uniformly distributed normal traction. In addition, use of the non-uniform discretization can significantly enhance the computational efficiency (associated with the significant reduction of number of elements or degrees of freedom) and accelerate the

convergence of numerical solutions. Via the comparison with reliable benchmark results for various cases, the converged solutions from the proposed technique have found in excellent agreement with those reference solutions.

While the proposed technique has been capable of handling nano-scale multi-layer media under surface excitation, the formulation is still restricted mainly to two-dimensional settings and prescribed surface loadings. The extension of the present work to treat fully three-dimensional scenarios and indentation problems is considered essential and can further enhance the capability of the solution procedure to attack more practical problems.



REFERENCES

- Ansari, R. & Norouzzadeh, A. 2016. "Nonlocal and surface effects on the buckling behavior of functionally graded nanoplates: An isogeometric analysis". *Physica E: Low-dimensional Systems and Nanostructures*, 84, 84-97.
- Attia, M. A. & Mahmoud, F. F. 2015. "Analysis of nanoindentation of functionally graded layered bodies with surface elasticity". *International Journal of Mechanical Sciences*, 94-95, 36-48.
- Cammarata, R. C. 1994. "Surface and interface stress effects in thin films". *Progress in Surface Science*, 46, 1-38.
- Chowdhury, M. S., Song, C. & Gao, W. 2014. "Probabilistic fracture mechanics with uncertainty in crack size and orientation using the scaled boundary finite element method". *Computers & Structures*, 137, 93-103.
- Dai, S., Augarde, C., Du, C. & Chen, D. 2015. "A fully automatic polygon scaled boundary finite element method for modelling crack propagation". *Engineering Fracture Mechanics*, 133, 163-178.
- Deeks, A. J. & Augarde, C. E. 2005. "A meshless local Petrov-Galerkin scaled boundary method". *Computational Mechanics*, 36, 159-170.
- Deeks, A. J. & Wolf, J. P. 2002a. "An h-hierarchical adaptive procedure for the scaled boundary finite-element method". *International Journal for Numerical Methods in Engineering*, 54, 585-605.
- Deeks, A. J. & Wolf, J. P. 2002b. "A virtual work derivation of the scaled boundary finite-element method for elastostatics". *Computational Mechanics*, 28, 489-504.
- Dingreville, R., Qu, J. & Cherkaoui, M. 2005. "Surface free energy and its effect on the elastic behavior of nano-sized particles, wires and films". *Journal of the Mechanics and Physics of Solids*, 53, 1827-1854.
- Gao, Y. F., Xu, H. T., Oliver, W. C. & Pharr, G. M. 2008. "Effective elastic modulus of film-on-substrate systems under normal and tangential contact". *Journal of the Mechanics and Physics of Solids*, 56, 402-416.
- Gibbs, J. W. 1906. *The scientific papers of J. Willard Gibbs*, Vol.1, London, Longmans Green.
- Gibson, R. J. G. 1967. "Some results concerning displacements and stresses in a non-homogeneous elastic half-space". 17, 58-67.
- Gravenkamp, H., Birk, C. & Song, C. 2014. "The computation of dispersion relations for axisymmetric waveguides using the Scaled Boundary Finite Element Method". *Ultrasonics*, 54, 1373-1385.
- Gurtin, M. E. 1973. 'The Linear Theory of Elasticity'. In: Truesdell, C. (ed.) *Linear Theories of Elasticity and Thermoelasticity: Linear and Nonlinear Theories of Rods, Plates, and Shells*. Berlin, Heidelberg: Springer Berlin Heidelberg.
- Gurtin, M. E. & Murdoch, A. I. 1975. "A continuum theory of elastic material surfaces". *Archive for Rational Mechanics and Analysis*, 57, 291-323.

- Gurtin, M. E. & Murdoch, A. I. 1978. "Surface stress in solids". *International Journal of Solids and Structures*, 14, 431-440.
- He, L. H. & Lim, C. W. 2006. "Surface Green function for a soft elastic half-space: Influence of surface stress". *International Journal of Solids and Structures*, 43, 132-143.
- He, L. H., Lim, C. W. & Wu, B. S. 2004. "A continuum model for size-dependent deformation of elastic films of nano-scale thickness". *International Journal of Solids and Structures*, 41, 847-857.
- He, Y., Yang, H. & Deeks, A. J. 2013a. "An Element-Free Galerkin Scaled Boundary Method for Steady-State Heat Transfer Problems". *Numerical Heat Transfer, Part B: Fundamentals*, 64, 199-217.
- He, Y., Yang, H. & Deeks, A. J. 2014. "Use of Fourier shape functions in the scaled boundary method". *Engineering Analysis with Boundary Elements*, 41, 152-159.
- He, Y., Yang, H., Xu, M. & Deeks, A. J. 2013b. "A scaled boundary finite element method for cyclically symmetric two-dimensional elastic analysis". *Computers & Structures*, 120, 1-8.
- Huang, D. W. 2008. "Size-dependent response of ultra-thin films with surface effects". *International Journal of Solids and Structures*, 45, 568-579.
- Huang, G. Y. & Yu, S. W. 2007. "Effect of Surface Elasticity on the Interaction Between Steps". *Journal of Applied Mechanics*, 74, 821-823.
- Intarit, P., Senjuntichai, T. & Rajapakse, R. K. N. D. 2010. "Dislocations and internal loading in a semi-infinite elastic medium with surface stresses". *Engineering Fracture Mechanics*, 77, 3592-3603.
- Intarit, P., Senjuntichai, T. & Rungamornrat, J. 2018. "Elastic layer under axisymmetric indentation and surface energy effects". *Zeitschrift für angewandte Mathematik und Physik*, 69, 29.
- Intarit, P., Senjuntichai, T., Rungamornrat, J. & Rajapakse, R. K. N. D. 2011. "Surface elasticity and residual stress effect on the elastic field of a nanoscale elastic layer". *Interaction and Multiscale Mechanics*, 4, 85-105.
- Intarit, P., Senjuntichai, T., Rungamornrat, J. & Rajapakse, R. K. N. D. 2017. "Penny-shaped crack in elastic medium with surface energy effects". *Acta Mechanica*, 228, 617-630.
- Karasudhi, P. 2012. *Foundations of solid mechanics*, Dordrecht, Netherlands : Springer
- Li, C., Man, H., Song, C. & Gao, W. 2013a. "Fracture analysis of piezoelectric materials using the scaled boundary finite element method". *Engineering Fracture Mechanics*, 97, 52-71.
- Li, C., Song, C., Man, H., Ooi, E. T. & Gao, W. 2014. "2D dynamic analysis of cracks and interface cracks in piezoelectric composites using the SBFEM". *International Journal of Solids and Structures*, 51, 2096-2108.
- Li, M., Guan, H., Zhang, H. & Liu, J. 2013b. "Three-dimensional investigation of

- wave–pile group interaction using the scaled boundary finite element method—Part II: Application results”. *Ocean Engineering*, 64, 185-195.
- Li, M., Zhang, H., Guan, H. & Lin, G. 2013c. “Three-dimensional investigation of wave–pile group interaction using the scaled boundary finite element method. Part I: Theoretical developments”. *Ocean Engineering*, 64, 174-184.
- Liu, J. & Lin, G. 2012. “A scaled boundary finite element method applied to electrostatic problems”. *Engineering Analysis with Boundary Elements*, 36, 1721-1732.
- Meng, X. N. & Zou, Z. J. 2013. “Radiation and diffraction of water waves by an infinite horizontal structure with a sidewall using SBFEM”. *Ocean Engineering*, 60, 193-199.
- Mi, C. 2017. “Surface mechanics induced stress disturbances in an elastic half-space subjected to tangential surface loads”. *European Journal of Mechanics - A/Solids*, 65, 59-69.
- Miller, R. E. & Shenoy, V. B. 2000. “Size-dependent elastic properties of nanosized structural elements”. *Nanotechnology*, 11, 139-147.
- Nguyen, T. B., Rungamornrat, J. & Senjuntichai, T. 2016. “Analysis of planar cracks in 3D elastic media with consideration of surface elasticity”. *International Journal of Fracture*, 202, 51-77.
- Nguyen, T. B., Rungamornrat, J., Senjuntichai, T. & Wijeyewickrema, A. C. 2015. “FEM-SGBEM coupling for modeling of mode-I planar cracks in three-dimensional elastic media with residual surface tension effects”. *Engineering Analysis with Boundary Elements*, 55, 40-51.
- Nguyen Van, C., Rungamornrat, J. & Pheinsusom, P. 2017. “Scaled Boundary Finite Element Method for Two-Dimensional Linear Multi-Field Media”. *Engineering Journal*, 21, 333-360.
- Norouzzadeh, A. & Ansari, R. 2018. “Isogeometric vibration analysis of functionally graded nanoplates with the consideration of nonlocal and surface effects”. *Thin-Walled Structures*, 127, 354-372.
- Ooi, E. T., Shi, M., Song, C., Tin-Loi, F. & Yang, Z. J. 2013. “Dynamic crack propagation simulation with scaled boundary polygon elements and automatic remeshing technique”. *Engineering Fracture Mechanics*, 106, 1-21.
- Ooi, E. T., Song, C., Tin-Loi, F. & J. Yang, Z. 2012. “Automatic modelling of cohesive crack propagation in concrete using polygon scaled boundary finite elements”. *Engineering Fracture Mechanics*, 93, 13–33.
- Park, H. J., Xu, T., Lee, J. Y., Ledbetter, A. & Guo, L. J. 2011. “Photonic Color Filters Integrated with Organic Solar Cells for Energy Harvesting”. *ACS Nano*, 5, 7055-7060.
- Pinyochotiwong, Y., Rungamornrat, J. & Senjuntichai, T. 2013. “Rigid frictionless indentation on elastic half space with influence of surface stresses”. *International Journal of Engineering Science*, 71, 15-35.

- Povstenko, Y. Z. 1993. "Theoretical investigation of phenomena caused by heterogeneous surface tension in solids". *Journal of the Mechanics and Physics of Solids*, 41, 1499-1514.
- Rungamornrat, J., Tuttipongsawat, P. & Senjuntichai, T. 2016. "Elastic layer under axisymmetric surface loads and influence of surface stresses". *Applied Mathematical Modelling*, 40, 1532-1553.
- Shenoy, V. B. 2002. "Size-dependent rigidities of nanosized torsional elements". *International Journal of Solids and Structures*, 39, 4039-4052.
- Shenoy, V. B. 2005. "Atomistic calculations of elastic properties of metallic fcc crystal surfaces". *Physical Review B*, 71, 094104.
- Shuttleworth, R. 1950. "The Surface Tension of Solids". *Proceedings of the Physical Society. Section A*, 63, 444.
- Song, C. & Wolf, J. P. 1997. "The scaled boundary finite-element method—alias consistent infinitesimal finite-element cell method—for elastodynamics". *Computer Methods in Applied Mechanics and Engineering*, 147, 329-355.
- Tarntira, K. 2018. "Multi-layer elastic medium under axisymmetric loading and surface energy effect". Mater thesis, Chulalongkorn University, Bangkok, Thailand.
- Timoshenko, S. & Goodier, J. 1970. *Theory of Elasticity*. McGraw-Hill, New York.
- Tirapat, S. & Senjuntichai, T. 2018. "Analysis of Indentation on Layered Elastic Medium with Surface Energy Effects". *Key Engineering Materials*, 775, 524-530.
- Tirapat, S., Senjuntichai, T. & Rungamornrat, J. 2017. "Influence of Surface Energy Effects on Elastic Fields of a Layered Elastic Medium under Surface Loading". *Advances in Materials Science and Engineering*, 2017, 1-11.
- Vu, T. H. & Deeks, A. J. 2006. "Use of higher-order shape functions in the scaled boundary finite element method". *International Journal for Numerical Methods in Engineering*, 65, 1714-1733.
- Vu, T. H. & Deeks, A. J. 2008. "A p-adaptive scaled boundary finite element method based on maximization of the error decrease rate". *Computational Mechanics*, 41, 441-455.
- Vu, T. H. & Deeks, A. J. 2014. "Using fundamental solutions in the scaled boundary finite element method to solve problems with concentrated loads". *Computational Mechanics*, 53, 641-657.
- Wang, G. F. & Feng, X. Q. 2007. "Effects of surface stresses on contact problems at nanoscale". *Journal of Applied Physics*, 101, 013510.
- Wolf, J. P. & Song, C. 1995a. "Consistent infinitesimal finite-element cell method: in-plane motion". *Computer Methods in Applied Mechanics and Engineering*, 123, 355-370.
- Wolf, J. P. & Song, C. 1995b. "Unit-impulse response matrix of unbounded medium by infinitesimal finite-element cell method". *Computer Methods in Applied*

Mechanics and Engineering, 122, 251-272.

- Wolf, J. P. & Song, C. 1996. *Finite-Element Modelling of Unbounded Media*, Chichester, John Wiley and Sons.
- Wolf, J. P. & Song, C. 2000. "The scaled boundary finite-element method – a primer: derivations". *Computers & Structures*, 78, 191-210.
- Wolf, J. P. & Song, C. 2001. "The scaled boundary finite-element method – a fundamental solution-less boundary-element method". *Computer Methods in Applied Mechanics and Engineering*, 190, 5551-5568.
- Wong, E. W., Sheehan, P. E. & Lieber, C. M. 1997. "Nanobeam Mechanics: Elasticity, Strength, and Toughness of Nanorods and Nanotubes". *Science*, 277, 1971-1975.
- Wu, L. K., Zhang, X. F. & Hu, J.-M. 2014. "Corrosion protection of mild steel by one-step electrodeposition of superhydrophobic silica film". *Corrosion Science*, 85, 482-487.
- Yang, C., Ji, C., Shen, W., Lee, K.-T., Zhang, Y., Liu, X. & Guo, L. J. 2016. "Compact Multilayer Film Structures for Ultrabroadband, Omnidirectional, and Efficient Absorption". *ACS Photonics*, 3, 590-596.
- Yang, F. 1998. "Indentation of an incompressible elastic film". *Mechanics of Materials*, 30, 275-286.
- Yu, H. Y., Sanday, S. C. & Rath, B. B. 1990. "The effect of substrate on the elastic properties of films determined by the indentation test — axisymmetric boussinesq problem". *Journal of the Mechanics and Physics of Solids*, 38, 745-764.
- Zhao, X. J. 2009. "Surface loading and rigid indentation of an elastic layer with surface energy effects". Master thesis, The university of British Columbia, Vancouver, Canada.
- Zhao, X. J. & Rajapakse, R. K. N. D. 2009. "Analytical solutions for a surface-loaded isotropic elastic layer with surface energy effects". *International Journal of Engineering Science*, 47, 1433-1444.
- Zhao, X. J. & Rajapakse, R. K. N. D. 2013. "Elastic field of a nano-film subjected to tangential surface load: Asymmetric problem". *European Journal of Mechanics A/Solids*, 39, 69-75.
- Zhou, L. G. & Huang, H. 2004. "Are surfaces elastically softer or stiffer?". *Applied Physics Letters*, 84, 1940-1942.
- Zhu, X., Zhai, J. H. & Xu, W. 2019. "Analysis of surface-loaded problem of nonhomogeneous elastic half-plane with surface tension". *Mechanics of Materials*, 129, 254-264.

APPENDIX



จุฬาลงกรณ์มหาวิทยาลัย
CHULALONGKORN UNIVERSITY

VITA

NAME CHANTHA CHHUON

DATE OF BIRTH 09 May 1993

PLACE OF BIRTH Tunlorb village, PreyPouch commune, Angsnoul district,
Kandal province, Cambodia

**INSTITUTIONS
ATTENDED** 1. Institute of Technology of Cambodia

HOME ADDRESS 2. Chulalongkorn University
Tunlorb village, PreyPouch commune, Angsnoul district,
Kandal province, Cambodia



จุฬาลงกรณ์มหาวิทยาลัย
CHULALONGKORN UNIVERSITY